

<b>REPORT DOCUMENTATION PAGE</b>			Form Approved OMB NO. 0704-0188		
<p>The public reporting burden for this collection of information is estimated to average 1 hour per response, including the time for reviewing instructions, searching existing data sources, gathering and maintaining the data needed, and completing and reviewing the collection of information. Send comments regarding this burden estimate or any other aspect of this collection of information, including suggestions for reducing this burden, to Washington Headquarters Services, Directorate for Information Operations and Reports, 1215 Jefferson Davis Highway, Suite 1204, Arlington VA, 22202-4302. Respondents should be aware that notwithstanding any other provision of law, no person shall be subject to any penalty for failing to comply with a collection of information if it does not display a currently valid OMB control number.</p> <p>PLEASE DO NOT RETURN YOUR FORM TO THE ABOVE ADDRESS.</p>					
1. REPORT DATE (DD-MM-YYYY) 12-06-2015		2. REPORT TYPE Ph.D. Dissertation		3. DATES COVERED (From - To) -	
4. TITLE AND SUBTITLE Self-catalyzed growth of axial GaAs/GaAsSb nanowires by molecular beam epitaxy for photodetectors			5a. CONTRACT NUMBER W911NF-11-1-0223		
			5b. GRANT NUMBER		
			5c. PROGRAM ELEMENT NUMBER 206022		
6. AUTHORS Sai Krishna Ojha			5d. PROJECT NUMBER		
			5e. TASK NUMBER		
			5f. WORK UNIT NUMBER		
7. PERFORMING ORGANIZATION NAMES AND ADDRESSES North Carolina A&T State University 1601 East Market Street  Greensboro, NC 27411 -0001			8. PERFORMING ORGANIZATION REPORT NUMBER		
9. SPONSORING/MONITORING AGENCY NAME(S) AND ADDRESS (ES) U.S. Army Research Office P.O. Box 12211 Research Triangle Park, NC 27709-2211			10. SPONSOR/MONITOR'S ACRONYM(S) ARO		
			11. SPONSOR/MONITOR'S REPORT NUMBER(S) 59052-EL-REP.7		
12. DISTRIBUTION AVAILABILITY STATEMENT Approved for public release; distribution is unlimited.					
13. SUPPLEMENTARY NOTES The views, opinions and/or findings contained in this report are those of the author(s) and should not be construed as an official Department of the Army position, policy or decision, unless so designated by other documentation.					
14. ABSTRACT Semiconductor nanowires are currently attracting great interest due to their unique optical and electrical properties with great prospects for potential optoelectronic device applications at nanoscale. The GaAsSb materials system, in particular, is promising in the telecommunication wavelength range of 1.3-1.55 $\mu$ m. This dissertation describes the growth of self-catalyzed GaAs/GaAsSb nanowires (NWs) on Si (111) substrates using molecular beam epitaxy (MBE) and growth optimization of GaAs NWs along with the p-type doping incorporation. Substrate					
15. SUBJECT TERMS Nanowire, Self Catalyzed, GaAs/GaAsSb, Molecular Beam Epitaxy, Raman, MicroPL					
16. SECURITY CLASSIFICATION OF:			17. LIMITATION OF ABSTRACT	15. NUMBER OF PAGES	19a. NAME OF RESPONSIBLE PERSON
a. REPORT UU	b. ABSTRACT UU	c. THIS PAGE UU	UU		Shanthi Iyer
					19b. TELEPHONE NUMBER 336-285-3710

## Report Title

Self-catalyzed growth of axial GaAs/GaAsSb nanowires by molecular beam epitaxy for photodetectors

### ABSTRACT

Semiconductor nanowires are currently attracting great interest due to their unique optical and electrical properties with great prospects for potential optoelectronic device applications at nanoscale. The GaAsSb materials system, in particular, is promising in the telecommunication wavelength range of 1.3-1.55  $\mu\text{m}$ . This dissertation describes the growth of self-catalyzed GaAs/GaAsSb nanowires (NWs) on Si (111) substrates using molecular beam epitaxy (MBE) and growth optimization of GaAs NWs along with the p-type doping incorporation. Substrate preparation prior to the growth of NWs was found to be critical for achieving vertical and dense NWs. Both in-situ annealing and chemically etched substrates were examined. A detailed growth study on the effects of growth parameters namely V/III flux ratios, growth temperature, Ga opening duration used for the initiation of NW growth and effect of As species were used to determine the optimized growth condition. Chemically etched substrates provide the best results in terms of achieving >90% vertical NWs with high density >108/cm<sup>2</sup> NWs due to a better control on the thickness of the SiO<sub>2</sub> layer with appropriate micropore opening for the nucleation of Ga droplet initiating the NW growth. A detailed and systematic study of morphological, structural, compositional, vibrational and optical properties of GaAs/GaAsSb segmented NWs were performed on non-etched and etched substrates using variety of characterization techniques namely scanning electron microscope, X-ray diffraction, energy dispersive X-ray spectroscopy, (scanning) transmission electron microscopy,  $\phi$ -photoluminescence and Raman spectroscopy. 4K PL emission energy as low as 1.345eV were obtained on non-etched substrates. A FWHM of  $\sim$ 70 meV was observed in the room temperature photoluminescence (PL) for double segmented NWs. The low temperature PL behavior appears to be dominated by excitons bound to shallow defects. Two non-radiative channels were found, one weakly-bound exciton and the other related to a deep center, which appears to be influenced by the NW configuration. GaAs/GaAsSb axial NWs grown on chemically etched substrates produced 4K PL emission energy which redshifted to 1.2 eV. Intensity dependence of the PL emission indicated a type II band alignment. The GaAsSb segment always exhibited a zinc blende structure with mixture of stacking faults and twins and the presence of these faults were significantly reduced in the NWs grown on chemically etched substrates. For fabrication of an axial p-i-n heterostructured NW photodetector using the above segmented configuration, Be doping of the GaAs NW was also examined. Be incorporation in the NW was found to be strongly influenced by the Be cell temperature and V/III flux ratio for the shell. Preliminary data demonstrates the potential to further redshift the wavelength in heterostructured NWs for the fabrication of NW based photodetectors

**Self-catalyzed growth of axial GaAs/GaAsSb nanowires by  
molecular beam epitaxy for photodetectors**

Sai Krishna Ojha

North Carolina A&T State University

A dissertation submitted to the graduate faculty  
in partial fulfillment of the requirements for the degree of

DOCTOR OF PHILOSOPHY

Department: Electrical and Computer Engineering

Major: Electrical Engineering

Major Professor: Dr. Shanthi Iyer

Greensboro, North Carolina

2015

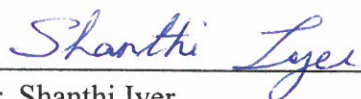
The Graduate School  
North Carolina Agricultural & Technical State University  
This is to certify that the Doctoral Dissertation of

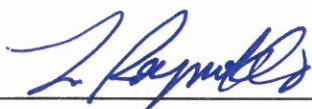
Sai Krishna Ojha

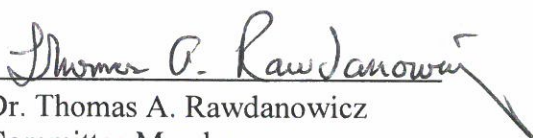
has met the dissertation requirements of  
North Carolina Agricultural & Technical State University

Greensboro, North Carolina  
2015

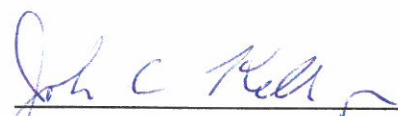
Approved by:

  
Dr. Shanthi Iyer  
Major Professor

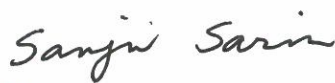
  
Dr. C. Lewis Reynolds, Jr.  
Committee Member

  
Dr. Thomas A. Rawdanowicz  
Committee Member

  
Dr. Ward Collis  
Committee Member

  
Dr. John Kelly  
Department Chair

  
Dr. Zhijian (Cliff) Xie  
Committee Member

  
Dr. Sanjiv Sarin  
Dean, The Graduate School

© Copyright by

Sai Krishna Ojha

2015

### Biographical Sketch

Sai Krishna Ojha was born in Sunabeda, Orissa located in India. He received his Master of Science in Physics with photonics specialization from Sathya Sai Institute of Higher Learning, India, in 2008. He worked with Wipro Technologies, India, from 2008 to 2010. He is passionate and excited in working with the novel area of semiconductor materials and nanotechnology.

## Dedication

This work is dedicated to my mentor and the most compassionate, Bhagwan Sri Sathya Sai Baba.

## Acknowledgments

I would like to express my gratitude to my advisor Dr. Shanthi Iyer who constantly guided me throughout the PhD program. Her knowledge, hard work and commitment were highly inspirational and were a constant catalyst for me to grow in my research. It was definitely a great experience, quantum leap in my life which would be a stepping stone for all the future opportunities in my career.

I would like to thank my committee members, Dr. C. Lewis Reynolds. Jr and Dr. Thomas A. Rawdanowicz from Department of Materials Science and Engineering from North Carolina State University, Dr. Ward Collis and Dr. Zhijian Xie from Department of Electrical and Computer Engineering, North Carolina A &T State University. Their feedback and support were valuable in interpretation of crucial results. I would like to thank Dr. John Kelly, the chairperson of Department of Electrical and Computer Engineering, North Carolina A &T State University for his support throughout my stay at North Carolina A&T State University.

I would like to thank Professor Yuntian Zhu and Dr. Judith Reynolds from North Carolina State University for their support in using the Raman system, Dr. Thomas A. Rawdanowicz and Dr. Yang Liu for their support on scanning transmission electron microscope (STEM) and Dr. Cynthia S Day from Wake Forest University for the use of XRD system and Dr. Ryan White for the XEDS measurements on the FEI Titan G2 at NC State University's Analytical Instrumentation Facility.

Special thanks to former and current researchers from Dr. Iyer's group. Dr. Jia Li, for his instrumentation skills, Pavan Kumar Kasanaboina for being a close friend and a constant support in many research related discussions. Md.Sami, Prithviraj Deshmukh, Estiak Ahmad and Manish Sharma for their constant support. I won't be justifying if I don't acknowledge my seniors,

Shereen Farhana, Dr. Nimai Chand Patra, Dr. Adam Bowen, Dr. Robert Alston, Dr. Tanina Bradley and Dr. Sudhakar Bharatan.

I would not have been here without the love and support of my father, mother, brother and sister. I am highly grateful to them for all they have done for me. I would like to thank all my friends and families in Greensboro who have always loved and helped in time of need without any expectations.

I would like to acknowledge the financial support by the Army Research Office (Grant No. W911NF-11-1-0223,) under the technical monitor-William Clark and also Triad Interuniversity Project (TIPP), (Project Award # A14-0011-001).

## Table of Contents

Table of Contents .....	vii
List of Figures .....	xi
List of Tables .....	xvii
Abbreviations .....	xviii
Abstract .....	1
CHAPTER 1 Introduction.....	3
1.1 Challenges.....	7
1.2 Objectives .....	8
1.3 Dissertation Outline .....	10
CHAPTER 2 Literature Review .....	13
2.1 Introduction.....	13
2.2 Nanowire Growth .....	13
2.2.1 The role of liquid droplet in the NW. ....	14
2.3 Heterostructured NW Systems .....	17
2.3.1 GaAs/AlGaAs NWs.....	18
2.3.2 InAs/InAsSb NWs. ....	19
2.3.3 InGaAs NWs. ....	19
2.3.4 GaAs/GaAsSb NWs. ....	20
2.3.4.1 Photoluminescence study of the GaAs/GaAsSb. ....	22
2.4. P-type Doping in NWs.....	23
2.5 Summary .....	26
CHAPTER 3 Experimental Methodology .....	27
3.1 Introduction.....	27

3.2 Molecular Beam Epitaxy (MBE).....	27
3.2.1 Refraction high energy electron diffraction (RHEED). ....	31
3.3 Growth Process of GaAs/GaAsSb NWs on Si (111) Substrates .....	32
3.4 Characterization Techniques .....	33
3.4.1 Scanning electron microscope.....	33
3.4.2 Photoluminescence (PL).....	34
3.4.3 Raman spectroscopy. ....	36
3.4.4 Atomic Force Microscopy.....	37
3.4.5 X-Ray Diffraction.....	38
3.4.6 Transmission electron microscope. ....	39
3.5 Conclusion .....	41
CHAPTER 4 Study of Be Doping in Ga Assisted GaAs Nanowires .....	42
4.1 Introduction.....	42
4.2 Experimental Details .....	42
4.3 Results.....	44
4.3.1 Scanning Electron Microscopy.....	44
4.3.2 X ray diffraction and STEM.....	46
4.3.3 Optical study of the Be doped NWs. ....	50
4.3.3.1 Photoluminescence study. ....	51
4.3.4 Growth of Be doped on etched substrates. ....	57
4.3.4.1 Photoluminescence measurement. ....	59
4.4 Conclusion .....	60
CHAPTER 5 GaAs/GaAsSb Axial NWs on Non-etched Epiready Si Substrate .....	62
5.1 Introduction.....	62
5.2 MBE Growth .....	62

5.2.1 Ga assisted GaAs/GaAsSb NWs on Si (111). .....	62
5.3 Scanning Electron Microscopy Analysis. ....	64
5.4 XRD Analysis. ....	66
5.5 TEM Analysis. ....	67
5.5.1 Composition analysis by XEDS. ....	70
5.6 Photoluminescence .....	72
5.7 Raman Spectroscopy .....	78
5.8 Conclusions. ....	80
CHAPTER 6 Optimization of GaAs NWs on a Non-etched Si Substrate .....	81
6.1 Introduction. ....	81
6.2 Experimental Details .....	81
6.3 Optimization Process .....	82
6.3.1 Effect of annealing. ....	85
6.3.2 Comparison between As <sub>2</sub> and As <sub>4</sub> . ....	86
6.4 Conclusion .....	87
CHAPTER 7 Optimization Process on Etched Si Substrates .....	88
7.1 Introduction. ....	88
7.2 Experimental Details .....	89
7.3 Optimization Process on Etched Si (111) Substrates .....	91
7.4 Comparison of the GaAs/GaAsSb/GaAs NWs on both Etched and Non-etched substrates .....	95
7.5 Conclusion .....	100
CHAPTER 8 Compositional variation of Sb in Ga Assisted Axial GaAs/GaAsSb/GaAs Heterostructure Nanowires on Chemically Etched Si Substrate.....	101
8.1 Introduction.....	101

8.2 Experimental Details .....	102
8.3 Results.....	102
8.3.1 Morphological analysis. ....	102
8.3.2 Sb composition by EDX.....	104
8.3.3 STEM Study. ....	106
8.3.4 X- Ray Diffraction.....	108
8.3.5 Photoluminescence. ....	109
8.3.6 Raman Analysis.....	112
8.4 Conclusion .....	113
CHAPTER 9 Summary and Scope of Future Work .....	115
9.1 Summary.....	115
9.1.1 GaAs/GaAsSb Segmented NWs.....	115
9.1.2 High density and vertical NWs.....	116
9.1.3 Doping. ....	117
9.2 Future Work.....	117
References .....	119
Appendix A.....	133

## List of Figures

Figure 1.1. Energy gap vs lattice constant of different semiconductor alloys with energy gap in the NIR region.....	6
Figure 2.1. Step wise explanation of vapor liquid solid (VLS) growth mechanism.....	14
Figure 2.2. Energy band gap vs lattice constant [61].....	18
Figure 2.3. Low temperature power dependent PL spectra ( $P= 2.55\text{W}/\text{cm}^2$ ) of a NW together with 30 kV BF STEM image (inset).The scale bar in the inset is 500 nm. (Reprinted with permission from [91], Copyright 2011 IOP Publishing). ....	23
Figure 2.4. Processes that influence the doping and diffusion of Be dopants in NWs.(Adapted after [36], Copyright 2013 American Institute of Physics).....	24
Figure 3.1. EPI 930 molecular beam epitaxy system.....	28
Figure 3.2. Schematic diagram of the different sources in the Veeco EPI 930 MBE system. ....	30
Figure 3.3. Cutaway view of valved oven for high-vapor-pressure elements (e.g., $\text{As}_4$ , $\text{P}_4$ , etc.): (1) internal hot zone for molecular cracking of tetramers to dimers, (2) mounting flange, (3) valve seat for isolating charge, (4) externally heated large volume PBN insert crucible and (5) controlled leak valve stem.(Reprinted with permission from [83]. Copyright 2002 Elsevier).....	30
Figure 3.4. Surface morphologies deduced from the RHEED patterns. (Adapted from [87]). ....	32
Figure 3.5. Carl Zeiss Auriga-BU FIB FESEM Microscope.....	34
Figure 3.6. Photoluminescence setup.....	36
Figure 3.7. Bruker's Discover D8 X-ray diffraction system[92].....	39
Figure 3.8. A schematic of the TEM set-up.....	40
Figure 4.1. Summary of the growth parameters of the Be-doped NWs where the samples are divided based on the core/shell, Be cell temperature ( $^{\circ}\text{C}$ ) and V/III ratio. ....	43

Figure 4.2. Variation of (a) NW density, (b) Diameter and (c) NW 2D layer thickness as a function of V/III ratio during core growth. SEM images of NWs with constant core V/III ratio of 6 and different shell V/III ratio of (d) 20,(e) 35 and (f) 70 at a Be cell temperature of 900°C.....	45
Figure 4.3. Variation of (a) length and diameter and (b) density of the nanowires with Be cell temperature. Be doped GaAs NWs with increasing Be cell temperature from (c) 800°C to (d) 990°C.....	46
Figure 4.4. XRD scans of core and shell structured NWs for Be cell temperatures of 900° C and 990°C.....	47
Figure 4.5 HAADF and STEM images which (a) and (b) displays the zinc blende GaAs with GaAs dumbbells clearly visible as viewed from the [011] zone axis (c) Image showing necking down near the NW tip (d) FFT of WZ region in the NW tip viewed along the [2110] zone axis with WZ growth direction as <0001>.....	48
Figure 4.6. (a) Shows a transition from ZB to WZ with random twinning present (b) The tip end of the GaAs structure is shown transitioning back to ZB. ....	49
Figure 4.7. (a) HAADF STEM image of core NW, viewed along the [011] ZB zone axis indicating a predominantly ZB region.(b) viewed along the [2110]   [011] (WZ  ZB) zone axes indicating a transition region from twinning ZB to polytype WZ congruent with NW diameter reduction (c) HAADF STEM image with selected areas annotated for region identification and correlation of subsequent images viewed from different axes, (d) viewed along the [2110] WZ zone axis indicating predominantly polytype wurtzite crystal structure (e) viewed along [2110]  [011] (WZ  ZB) zone axes at the NW tip terminating in a ZB structure.....	50
Figure 4.8. (a) PL spectra of samples with variation in density and 2D layer thickness for NWs grown at Be cell temperature of 900°C. (b) PL spectra of NWs at different Be cell temperature.	51

Figure 4.9. PL spectra of NWs grown at different V/III ratios of (a) core and (b) core/shell configurations. (c) PL spectra of core/shell (6/35) NWs for different Be cell temperatures and (d) comparison of core/shell structure for NWs grown at Be cell temperatures of 900°C and 990°C and at V/III ratios of 70 and 35. ....	52
Figure 4.10. Raman plots of the (a) NW core and (b) with the core/shell configuration grown at Be cell temperature of 990°C. Variation of (c) FWHM (LO) modes of GaAs and its (d) their intensities (LO) and (e) $I_{TO}/I_{LO}$ for the GaAs peaks as a function of Be cell temperature. ....	56
Figure 4.11. (a) shows the SEM image of Be doped NWs, (b) shows the schematic of I-V measurement for both the samples, (c) I-V curve for the ensemble of NWs at Be cell temperature of 900°C and 990°C. ....	58
Figure 4.12. (a) 4K photoluminescence of samples grown with Be cell temperature of 900°C and 990°C (b) comparing single NW with the ensemble of NWs of sample grown with Be cell temperature of 990°C. ....	60
Figure 5.1. RHEED patterns of a Si substrate in the initial GaAs NWs growth showing the 3D islands formation. ....	63
Figure 5.2. Typical RHEED image during a GaAs/GaAsSb NW growth on an epitaxially grown Si (111). ....	64
Figure 5.3. (a) schematic of the one segment NWs (b) two segmented NWs grown along with their expected dimensions. We also see the opening and closing time of Sb valve. ....	65
Figure 5.4. Hexagonal-shaped GaAs NWs grown on Si substrate and (b) comparison of the percentage of vertical and bent wires in different samples taken over an area of $200 \mu\text{m}^2$ . ....	65
Figure 5.5. (a) Single segmented NW with Ga droplet on the top. (b) NW with tapered top .....	66
Figure 5.6. XRD scan of sample N1 620 and N2 are GaAs/GaAsSb NWs grown .....	67

Figure 5.7. Shows (a) the TEM image of a NW with twin planes and (b) the corresponding SAED pattern of the twin (111) plane. Inverse Fast Fourier filter of HRTEM image (c) applied to the (002) reflections of both ZB twin phases illustrates the mirroring of the (002) and (002t) planes across the twin boundary. ....	68
Figure 5.8. N2 NW without a Ga droplet at the tip and with a 400 nm region with a WZ structure just below the tip. The very tip end and the remaining NW below the WZ region are pure ZB with multiple twinning. ....	69
Figure 5.9. (a) A NW with a single GaAsSb band (Region 2 (e)) imaged with TEM, (b) HAADF-STEM and (c) through (e) XEDS-STEM mapping of Ga, As and Sb, respectively. (f) .....	71
Figure 5.10. (a) 11 K PL spectra of the NWs and (b) temperature dependence of PL peak energy. ....	72
Figure 5.11. Varshni fit for the data of sample N1 620. ....	74
Figure 5.12. Temperature dependence of integrated intensity.....	75
Figure 5.13. Variation of the full width half maximum (FWHM) with temperature for sample N1, N1 620 and N2. ....	76
Figure 5.14. Raman spectra depicting the GaAs and GaSb like modes of NWs N1 and N2 compared to the epitaxial GaAsSb epitaxial film reference. ....	79
Figure 6.1. Cross section SEM images of GaAs NWs on Si (111) substrate with a change in V/III ratio with (a) 6 (b) 15. ....	83
Figure 6.2. Variation in the Ga opening vs V/III ratio (Green and brown color corresponds to..	83
Figure 6.3. Plot of samples with different annealing time vs Ga opening and densities. ....	85

Figure 6.4. Graph depicting the increase in the % of bent NWs with the change in the annealing time, Ga opening and density of the NWs. ....	86
Figure 7.1. Schematic diagram of the etching process performed on the intrinsic Si (111) substrate. ....	90
Figure 7.2. Schematic diagram of the etching process performed on the p- type Si (111) substrate. ....	91
Figure 7.3. (a) SEM image of circular patched GaAs/GaAsSb/GaAs NWs with > 90 % vertical orientation. ....	92
Figure 7.4. AFM image on the optimized substrate showing the formation of SiO <sub>2</sub> and the corresponding top view SEM of the nanowires. ....	93
Figure 7.5. AFM image of Si (111) substrate with different oxidation timings. ....	94
Figure 7.6. SEM images show the top view of the NWs grown on Si (111) with different oxidation timings from (a) 48 hrs (b) 10 hrs and (c) 3.3 hrs. ....	94
Figure 7.7. SEM images of GaAs/GaAsSb/GaAs NWs on (a) non-etched substrate and (b) etched Si substrates. ....	95
Figure 7.8.(a) Low temperature photoluminescence spectra of the single segmented GaAsSb NWs. Here NE1 (non-etched) indicates the NWs with single segment and E1 (etched), the NWs with single segment with high densities. (b) Plot for calculating the activation energies for both single segmented NWs. ....	98
Figure 7.9. Raman spectra depicting the LO and TO modes of GaAs and GaSb. ....	99
Figure 8.1. SEM images of the NWs with different composition of Sb varying from 0 to 4.5 at. % in the GaAsSb insert in GaAs/GaAsSb/GaAs core NW. ....	103
Figure 8.2. Shows the EDX spectrum of a GaAs/GaAsSb NW with 1 at. % Sb. ....	104

Figure 8.3. Shows the EDX spectrum of a GaAs/GaAsSb NW with 4.5 at. % Sb.....	105
Figure 8.4. (a) TEM image of the core NW (b) HR-TEM image displaying the stacking faults and twinning defects. (c)SAED pattern showing the ZB crystal structure. (d)ZB structure and (e) TEM image of NW2 with the ZB structure (inset) and the SAED pattern (inset).....	107
Figure 8.5. The XRD spectra of GaAs/GaAsSb/GaAs for different concentrations of Sb depicting the occurrence of different planes of GaAs, GaSb and Si. (a) Shows the $2\theta^\circ$ region from $50^\circ$ to $60^\circ$ , (b) from $86^\circ$ to $96^\circ$ and (c) the GaAsSb (222) peak for S4 sample. ....	108
Figure 8.6. 4K PL spectra with Sb at. % varying from 0 to 4.5.....	109
Figure 8.7. Temperature dependent PL spectra for both (a) S2 and (b) S4. ....	110
Figure 8.8. Intensity dependent photoluminescence spectra for core sample containing (a) S2 (b) S4. ....	111
Figure 8.9. Proposed schematic energy band diagram for (a) GaAs and .....	112
Figure 8.10 Raman spectra depicting the shift in the peak (encircled) with the variation in the at. % of Sb in the samples from S1 to S4. ....	113

# List of Tables

Table 5.1 Summary of the PL parameter and pertinent PL data.....	73
Table 5.2 Raman mode data for N1, N2 and the reference GaAsSb epilayer grown on GaAs ...	79
Table 6.1 Shows the list of samples grown during the optimization process .....	82
Table 8.1 The dimensions of the NWs and Sb at. % along the length of S2 .....	105
Table 8.2 The dimensions of the NW and Sb at. % along the length of S4.....	106

## Abbreviations

$\alpha$	Absorption coefficient
AFM	Atomic force microscopy
at. %	Atomic percent
E <sub>g</sub>	Band gap energy
BEP	Beam equivalent pressure
Be	Beryllium
CB	Conduction band
cps	Counts per second
Cu	Copper
EDX	Energy dispersive x-ray spectroscopy
et al.	Et al.
FWHM	Full width half maxima
GaAs	Gallium arsenide
GaAsSb	Gallium arsenide antimonide
HRXRD	High resolution x-ray diffraction
HAADF	High angle annular dark field
I <sub>LO</sub>	Intensity of LO phonon mode
I <sub>TO</sub>	Intensity of TO phonon mode
IR	Infrared
LED	Light emitting diode
LO	Longitudinal optical
MBE	Molecular beam epitaxy

MOCVD	Metalorganic chemical vapor deposition
MOVPE	Metal organic vapor phase epitaxy
NCA	Nano Channel Aluminum
NW	Nanowire
PL	Photoluminescence
PMMA	Poly methyl methacrylate
RHEED	Reflection high energy electron diffraction
RGA	Residual gas analyzer
SAED	Selected area electron diffraction
SEM	Scanning electron microscope
STEM	Scanning transmission electron microscope
$R_{\text{rms}}$	Surface roughness RMS
VLS	Vapor liquid solid
VSS	Vapor solid solid
$T_s$	Substrate temperature
2D	Two dimensional
3D	Three dimensional
UHV	Ultra high vacuum
$E_v$	Valence band energy
$\lambda$	Wavelength
WZ	Wurtzite
XRD	X-ray diffraction
ZB	Zinc blende

## Elements with the atomic mass and atomic number

<b>4-</b> atomic number <b>Be</b> <b>Beryllium</b> <b>9.0121831-</b> atomic weight		
	<b>31</b> <b>Ga</b> <b>Gallium</b> <b>69.723</b>	<b>33</b> <b>As</b> <b>Arsenic</b> <b>74.921</b>
		<b>51</b> <b>Sb</b> <b>Antimony</b> <b>121.760</b>

## Abstract

Semiconductor nanowires are currently attracting great interest due to their unique optical and electrical properties with great prospects for potential optoelectronic device applications at nanoscale. The GaAsSb materials system, in particular, is promising in the telecommunication wavelength range of 1.3-1.55  $\mu\text{m}$ . This dissertation describes the growth of self-catalyzed GaAs/GaAsSb nanowires (NWs) on Si (111) substrates using molecular beam epitaxy (MBE) and growth optimization of GaAs NWs along with the p-type doping incorporation. Substrate preparation prior to the growth of NWs was found to be critical for achieving vertical and dense NWs. Both in-situ annealing and chemically etched substrates were examined. A detailed growth study on the effects of growth parameters namely V/III flux ratios, growth temperature, Ga opening duration used for the initiation of NW growth and effect of As species were used to determine the optimized growth condition. Chemically etched substrates provide the best results in terms of achieving >90% vertical NWs with high density  $>10^8/\text{cm}^2$  NWs due to a better control on the thickness of the  $\text{SiO}_2$  layer with appropriate micropore opening for the nucleation of Ga droplet initiating the NW growth. A detailed and systematic study of morphological, structural, compositional, vibrational and optical properties of GaAs/GaAsSb segmented NWs were performed on non-etched and etched substrates using variety of characterization techniques namely scanning electron microscope, X-ray diffraction, energy dispersive X-ray spectroscopy, (scanning) transmission electron microscopy,  $\mu$ -photoluminescence and Raman spectroscopy. 4K PL emission energy as low as 1.345eV were obtained on non-etched substrates. A FWHM of  $\sim 70$  meV was observed in the room temperature photoluminescence (PL) for double segmented NWs. The low temperature PL behavior appears to be dominated by excitons bound to shallow defects. Two non-radiative channels were found, one weakly-bound exciton and the other related

to a deep center, which appears to be influenced by the NW configuration. GaAs/GaAsSb axial NWs grown on chemically etched substrates produced 4K PL emission energy which redshifted to 1.2 eV. Intensity dependence of the PL emission indicated a type II band alignment. The GaAsSb segment always exhibited a zinc blende structure with mixture of stacking faults and twins and the presence of these faults were significantly reduced in the NWs grown on chemically etched substrates. For fabrication of an axial p-i-n heterostructured NW photodetector using the above segmented configuration, Be doping of the GaAs NW was also examined. Be incorporation in the NW was found to be strongly influenced by the Be cell temperature and V/III flux ratio for the shell. Preliminary data demonstrates the potential to further redshift the wavelength in heterostructured NWs for the fabrication of NW based photodetectors

## **CHAPTER 1**

### **Introduction**

Semiconductor nanowires (NWs) have received much attention due to their potential as building blocks for miniaturized optoelectronic devices [1]. NWs are one dimensional nanostructure materials whose diameter ranges from 10's of nm to 100's of nm with an aspect ratio of more than 10. These nanostructures display superior optical, electrical and magnetic properties due to their unique singular aspect of 1-D electronic density of states. Their properties can be controlled nonlinearly along their small diameter giving an edge over their bulk counterparts [2]. Simulation results performed by Zhang et al.[3] have shown that incident light can be waveguided into the vertical wires due to the refractive index difference between NWs and their surroundings. In addition, high surface to volume ratio and vertical configuration of NW ensemble lead to high optical absorption and efficient photon trapping[3].

NWs also enable different architectures including axial inserts [4, 5] and the core-shell configuration [1]. Axial insert in a NW refers to a tertiary heterostructure (10's nm in length) which are embedded along the axis of the NW that gives compatibility with 2D and bulk fabrication procedure. The core shell configuration shows a tremendous improvement in the light absorption feature where the core act as absorber and with a transparent shell, the anti-reflection property gets enhanced [6]. These structures have paved the way for applications such as transistors[1], photodetectors [7] and single photon sources [8] with reduced reflection, efficient light trapping and improved band tuning with strain relaxation. These features make NWs very attractive for variety of applications which are not possible in their bulk counterpart. Other advantages are bandgap engineering [9], material design freedom[10] and crystal phase.

Focusing on GaAs material system, predominant phases in GaAs NWs are wurtzite (WZ) and zinc blende (ZB) crystal phases, while in bulk, GaAs exhibits only zinc blende (ZB) structure. Reports have shown a variation in these crystal phases in a NW system can result in either a type I or II band alignment of the materials[9].

With the advancement of technology there is a continual demand on the optoelectronic devices for further improvement. For example, the requirements for the next generation detectors are: long spectral range, short dead time, negligible dark count rate and high detection efficiencies[11]. This past decade has seen considerable advancement in development of single photon detectors for optical quantum information applications [12]. Superconducting NWs single photon detectors (SNSPDs) is one such device that offers single photon sensitivity from visible to mid-IR wavelength improving its detection efficiency up to 57% in small area devices [13]. But the operation of SNSPDs occurs at 1.5-4K due to which there is a need for single photon detectors operating at higher temperature. Further work in semiconductor NWs can potentially overcome this limitation.

Current state of the art for optoelectronic devices such as detectors and lasers are based on either III-V or II-IV semiconductor materials. Silicon has been the most used material in the semiconductor industry for integrated circuits devices and CMOS devices. The small footprint of NWs enables accommodation of large lattice mismatch [14] and thus would facilitate integration of III-V material based photonic devices in the form of NWs to the electronic devices on Si.

The common growth mechanism of the NW is through the vapor liquid solid (VLS) mechanism where a catalyst droplet is used as a seed, which gets supersaturated with atoms from the liquid and vapor phases leading to NWs formation. In the last decade, majority of the work on the nucleation of NWs has suggested the use of Au as a catalyst [15, 16]. Yet due to the

formation of deep traps and contamination in the NWs, Au is not recommended. Early 2010 have seen several reports [17-20] on the vapor liquid solid (VLS) growth mechanism of self-assisted GaAs NWs through molecular beam epitaxy. The role of  $\text{SiO}_2$  in the initial nucleation of the Ga droplets during the NW growths has also been found to be important [21, 22]. The nanopores in the  $\text{SiO}_2$  layer provide the nucleation sites and help in immobilizing the Ga droplets which act as seed for the subsequent NW growth.

For achieving the desired emission, band tuning of the material is needed as electrical and optical properties are strongly dependent on the material composition. This implies that these properties can be tailored for specific applications by adjusting the composition. GaAs in particular has a direct band gap [23] that makes it an efficient photon absorber. In addition, this band gap of 1.4eV can be red shifted by alloying [9] it with Sb and In for application in the near infrared region. In case of NIR photodetectors, the two important wavelengths that are of great interest for optical telecommunications are 1.3  $\mu\text{m}$  and 1.55  $\mu\text{m}$ . However, the two alloys GaInAs and GaAsSb that can be tuned for achieving the above wavelength are highly lattice mismatched on Si substrate. In order to decrease the mismatch, an Sb ternary like GaAsSb can be grown as an insert in the GaAs NWs. Similar work on axial heterostructure such as GaAs/InGaAs/GaAs [4, 5] have also been demonstrated.

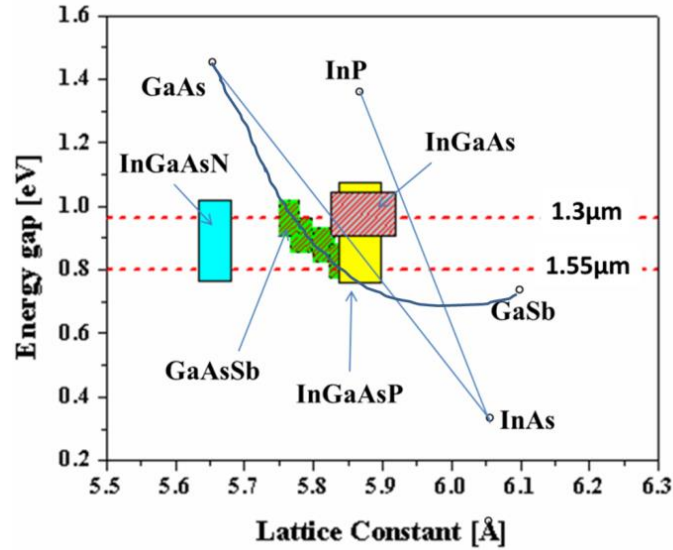


Figure 1.1. Energy gap vs lattice constant of different semiconductor alloys with energy gap in the NIR region.

As shown in Figure 1.1, there are several ternary and quaternary semiconductor materials that are active in the 1.3 and 1.55  $\mu\text{m}$  optical window. Two material systems that are extensively studied for applications in the NIR region are InGaAs[24, 25] and GaAsSb[26-31]. Extensive research has been performed on their structural [32] and optical properties[9, 33].

Comparing the two, GaAsSb has several advantages over InGaAs. Due to the presence of a single group III element in GaAsSb, its electronic structure is less dependent on its alloy configuration. The electron lifetime in GaAsSb is found to be twice as large. Auger recombination in GaAsSb is suppressed as compared to InGaAs. In addition, the surfactant nature of Sb in GaAsSb can be used to improve its structural properties where as large difference in the In and Ga diffusion generally leads to inhomogeneity in the InGaAs NWs. Due to the above reasons GaAsSb nanowires have great potential for optoelectronic applications in the NIR region, in particular, in the telecommunication wavelength window.

For fabricating a good photodetector, doping of the NWs is as important as having an active material like GaAsSb. Between the p and n type doping, p type doping is more challenging as the p-type impurity atoms have limited solubility in the host material and due to deep transition energy of the defects, a sufficient number of carriers do not get generated [34, 35]. There are reports [36-38] on the Be doping of GaAs NWs, but detailed effect of growth parameters on the Be incorporation is not clearly understood.

In the subsequent part of this chapter, the challenges, objective and the outline of the dissertation are discussed.

## **1.1 Challenges**

In the growth of GaAs/GaAsSb NWs there are numerous challenges that need to be overcome to obtain high- quality and defect free NWs. A few important ones are discussed below.

The first problem is the surfactant nature of Sb. Being a surfactant in nature, Sb would remain on the Si substrate making the growth of the NWs challenging. As the mismatch of GaAsSb on Si is large that may also pose a minor problem. As much work on GaAs NW on Si has already been researched [16, 30, 39], it is easier to grow initial GaAs NW followed by GaAsSb.

The second problem is the growth of the NWs with a catalyst. The role of a catalyst is crucial in the NW growth in the VLS mechanism. Among the several metals that have been used as the catalyst, Au has been the most common [40, 41]. However, the deep trap formation along with the high diffusivity of Au in most of the semiconductors leads to contamination of the NW. In addition, the trend toward the elimination of Au in most of the device processes in the electronics industry makes it unattractive. Hence, recently, there has been an increasing interest

on the self-catalyzed growth of NWs using the low melting point of the source element as the catalyst such as Ga melt for GaAs NWs [41]. It is noted that when this research began there were not many reports on the self-catalyzed growth. The size of the opening in the SiO<sub>2</sub> layer and size of the Ga droplet are critical for the growth of Ga catalyzed growth.

The third challenge is obtaining highly vertical and dense NWs. The NWs tend to orient in the direction that is more energetically favorable. Si (111) substrate was proposed [42] to produce NWs vertical with respect to the substrate in the growth direction. Commonly present two dimensional defects in NWs are twin planes and stacking faults. These defects should be minimized. The SiO<sub>2</sub> layer plays an important role in the initial nucleation of the Ga droplets. The thickness of SiO<sub>2</sub> and the nanopore openings of the appropriate size has been reported to be critical to achieve high NW density [17].

The fourth challenge is doping of NWs. For an effective device, the study of the doping needs to be addressed. Doping in NWs is challenging due to the small foot print and in particular, p-doping is found to be more challenging compared to n-type due to the surface Fermi level pinning and limited solubility of p-type dopant.

Finally, the fifth challenge is the narrow optimal growth condition for MBE grown GaAsSb NWs due to the presence of two competing group V species. The growth conditions have to be very stringently controlled to achieve the emission wavelength reaching 1.3 $\mu$ m.

## 1.2 Objectives

The objectives of this research are listed below:

- Effect of substrate preparation and growth parameters on the GaAs and GaAsSb NW density grown on Si (111) substrate by self-catalyzed MBE growth.
- Effect of Sb concentration on GaAs/GaAsSb NWs properties in the axial NW configuration.

- Study of Be doping in self-catalyzed GaAs NWs.

The above objectives were approached as follows:

*Optimization of the growth parameters of GaAs NWs:* The effects of growth parameters, namely growth temperature, role of As<sub>2</sub> and As<sub>4</sub>, annealing of Si (111) substrate and V/III ratios were studied independently for higher density and better quality of GaAs NWs. These NWs were then characterized structurally and optically for an optimized growth process. In addition, the role of naturally occurring SiO<sub>2</sub> on Si substrate was also studied. Both intrinsic and p –type Si substrate were chemically etched for achieving the optimum SiO<sub>2</sub> layer. The surface roughness of these substrates was also studied.

*Study of Be doping in self-catalyzed GaAs NWs:* For an effective device, the doping aspect in GaAs NWs was also studied. Different configurations of the NWs were examined for efficient incorporation of Be. A systematic study was also carried out to determine the effect of growth variants namely Be cell temperature and V/III ratio. It was examined in both the core and shell for an effective incorporation of Be and optimized parameters were established for enhanced Be incorporation. Growths were performed independently on epitaxially grown Si and chemically etched Si substrates for analyzing pre and post optimized parameters.

*Incorporation of GaAsSb in GaAs NWs:* The objective was to develop good quality, vertical GaAs/GaAsSb of high density NWs on Si (111) substrate for photo detection in the NIR (near infrared) region approaching 1.3  $\mu\text{m}$ . In order to achieve this, a systematic study of the GaAs/GaAsSb NW system was performed which was executed by growing self-catalyzed growth of GaAs/GaAsSb NWs on both intrinsic and p-type Si (111) substrates through molecular beam epitaxial method. This was accomplished by two processes.

- The first process was the growth of self-catalyzed GaAs/GaAsSb NWs on non-etched Si (111) substrates. This was achieved by using Ga as a self-catalyst and developing a simple growth scheme by growing the GaAs NWs on Si (111) substrates in which GaAsSb segments were inserted and capped with GaAs. This structure was designed based on the literature survey of other systems of NWs[4].
- The second process was to grow the same structure as in the first process on an etched Si substrate and later vary the composition of Sb in the GaAs/GaAsSb NWs for further band tuning towards 1.3  $\mu\text{m}$ . In order to achieve this, the Si substrates were chemically etched and the self- catalyzed growth of GaAs/GaAsSb NW was performed. For band tuning of the GaAsSb segment, Sb flux was varied to achieve at. % in solid from 0 to 4.5. The post growth characterization of these NWs were performed for its structural study and confirming the Sb incorporation.

The structure and morphology of these NWs were examined through scanning electron microscope (SEM), x-ray diffraction (XRD), scanning transmission electron microscope (STEM) and conventional and high resolution TEM. The optical characterizations were performed using 4 K photoluminescence and Raman spectroscopy.

### **1.3 Dissertation Outline**

This dissertation is organized into nine chapters and brief content of each chapter is listed below.

Chapter 1 discusses the motivation and challenges behind this work and the objective of this research. Brief historical evolution of photodetector is presented. The importance of the III/V heterostructure semiconductor materials for band gap tuning is discussed. Material system combinations that have been reported in literature for device applications in the optical window

of 1.3 and 1.55  $\mu\text{m}$  have been identified. The advantage of NWs over thin films is discussed and the advantages of GaAsSb over its competitor InGaAs are presented. Finally the statement of problem, objective of the dissertation and the approaches taken are listed.

Chapter 2 gives a brief literature review on the growth of GaAs NWs on GaAs and Si (111) substrates, the role of catalyst and different crystal phases formed during the growth. A brief review on different III/V heterostructured systems belonging to IR region is presented. Advantage of GaAsSb is highlighted showing its optical and structural properties. Importance of Be in doping of NWs is also discussed.

Chapter 3 provides experimental details on the MBE growth of NWs and also the other characterization techniques used in this research work are presented.

Chapter 4 describes the p-type doping of GaAs NWs using Be dopant. A comparison of the doping efficiency in the two NW architectures core and core-shell has been made. A comprehensive study of the doping effects on the morphological, structural and optical characteristics has been carried out using variety of characterization techniques, namely morphological, structural and optical characteristic were performed by x-ray diffraction (XRD), scanning electron microscopy (SEM), low temperature photoluminescence (PL), Raman spectroscopy and scanning transmission electron microscopy (STEM). These studies have been used to arrive at an optimized growth condition for enhanced Be doping.

Chapter 5 describes the study of the self-catalyzed Ga assisted growth of GaAs NWs with GaAsSb inserts on Si (111) substrate. The effects of the growth parameters namely, V/III ratios, growth temperature and Ga opening during the initial nucleation on the NW were studied. Different characterization techniques were performed for finding the morphological, structural and optical study in the NWs which were performed by scanning electron microscope (SEM), x-

ray diffraction (XRD), HR-TEM, low temperature photoluminescence of NWs and Raman spectroscopy.

Chapter 6 discusses the growth optimization of the GaAs NWs on non-etched Si substrates. Influence of V/III flux ratio, initial Ga opening duration prior to the growth, fluxes of adatoms, growth temperature on the NW density have been determined and the growth conditions for the optimized NW density and almost "0 % bent wires" that can be achieved, are demonstrated.

Chapter 7 describes the etching process to achieve highly dense and vertical NWs on etched Si (111) substrate. The substrates were chemically etched followed by oxidation for the desired SiO<sub>2</sub> layer. Atomic force microscopy (AFM) and scanning electron microscopy (SEM) were performed for measuring the surface roughness of the substrates and the morphological characteristics of the NWs, respectively.

In Chapter 8, the Sb composition was varied in the GaAsSb segment along the Ga assisted GaAs/GaAsSb axial NW heterostructures. These growths were performed on optimized etched Si substrate for better results. The effects of Sb composition on the structural, morphological and optical properties have been the subject of study in this Chapter.

Chapter 9 summarizes the research results and all the major achievements. It concludes with the scope for future work.

## CHAPTER 2

### Literature Review

#### 2.1 Introduction

In this chapter a brief history of the GaAs NW growth through MBE, the role of catalyst and the crystal phases formed in a NW are described. Different IR heterostructured NW systems are discussed showing the advantages of using GaAsSb for achieving the emission in the NIR region. The effects of Be doping in a core-shell GaAs NW are reviewed.

#### 2.2 Nanowire Growth

Many groups in the last decade have investigated [16, 40, 43-46] the growth mechanisms of NWs through metal organic chemical vapor deposition (MOCVD), molecular beam epitaxy (MBE), and chemical beam epitaxy (CBE) techniques. Based on the different phases of the material involved, the growth mechanisms are classified as vapor-liquid-solid (VLS) growth or vapor-solid-solid (VSS). Since most NW growths are mainly governed by VLS mechanism, a brief discussion of this technique is presented. In VLS [47], a liquid catalyst droplet is deposited on the substrate at certain growth temperature which becomes the nucleation center for the growth of the desired NW. During the growth, various species of material deposit on this droplet and produce a concentration gradient in the liquid. As the concentration of these solute species increases on the liquid droplet, the supersaturation of the droplet increases thereby leading to the growth of NWs. Depending on the adatoms incorporation on the NWs, there is either a vertical growth or a radial growth. By changing the reactant species, heterostructures can be grown by preferential incorporation on the catalyst or by deposition on the sidewalls of the NWs [48]. Thus the thermodynamic driving force for the nanowire formation is the vapor supersaturation with

respect to the solid phase, whereas the kinetic growth processes involved are surface diffusion and nucleation[16].The VLS process is summarized in the Figure 2.1 below.

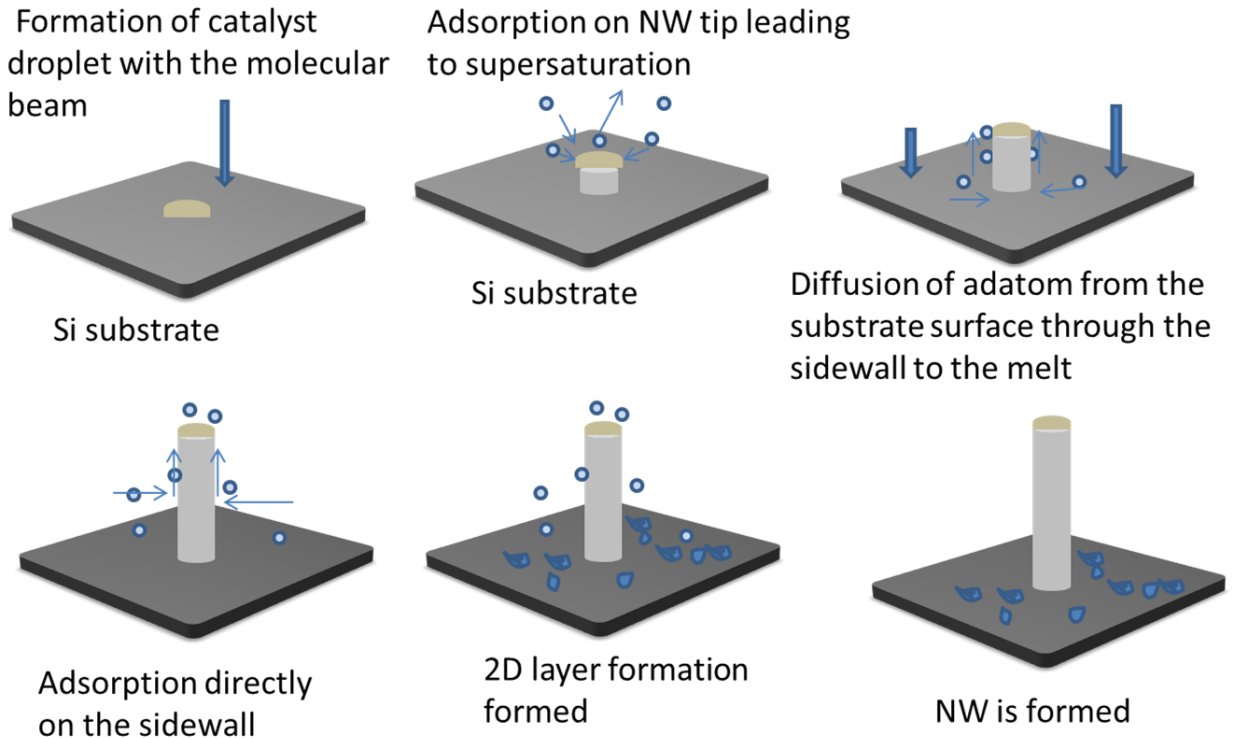


Figure 2.1. Step wise explanation of vapor liquid solid (VLS) growth mechanism.

**2.2.1 The role of liquid droplet in the NW.** The desirable attributes of the liquid-phase droplet to be used in the VLS process are: (1) it should exhibit a high accommodation coefficient (i.e., high probability that an impinging atom or molecule will be incorporated into the droplet) compared with the nanowire solid phase and (2) it should reduce the activation energy of nucleation at the liquid solid (nanowire) interface.

In the early stages of the GaAs NWs growth research, Au was preferred as a catalyst. Wu et al.[49] first demonstrated the growth of GaAs NWs using Au as a catalyst through MBE on a GaAs (111) B substrate. The NWs were grown using a nanochannel alumina (NCA) template. It was later shown by Dubrovskii et al. [16], that the NWs could be grown by itself by using Au as

catalyst without a template. They explained the length to diameter relation using the diffusion model. They also discussed in length the role of catalyst in the NW growth. Subsequent report by Plante et al. [50] demonstrated the growth of the GaAs NWs with Au catalyst on GaAs (111) B with a V/III ratio of 1.5 and 2.3 with the growth temperature ranging between 500°C and 600°C. They suggested that growth by surface diffusion becomes negligible for a large size catalyst and the direct impingement of atoms through the catalyst becomes dominant.

In 2007, Ihn et al. [51] reported the GaAs NWs growth on Si substrates with the growth along the [111] direction and the occurrence of zinc blende(ZB)- wurtzite(WZ) polytypism which was well known for GaAs substrates. Samsonenko et al. [52] further analyzed the structural and morphological properties by studying annealing effect, the role of oxide layer and surface orientation of the GaAs NWs on porous Si substrates. Paek et al.[19] demonstrated the effect of both Ga and As on the radial and axial growth of the NWs. With the increase in the Ga flux, there is increase in the diameter of the NW. At a constant Ga flux and corresponding increase in the As results in a higher axial growth rate. GaAs NWs growths on Si substrate with photoluminescence study were also reported [51]. A PL spectrum of 1.43 eV with FWHM of 50 meV was demonstrated suggesting pure GaAs/Si (111) NW crystals. [52, 53].  $\mu$ -PL study on WZ GaAs NWs showed the existence of free exciton peak ~29 meV higher than that of ZB GaAs [53]. Temperature dependent PL study was carried out due to ascertain the presence of non-radiative defects.

It is well known that Au leads to deep trap formation which reduces the carrier mobility in the substrate. A trace amount of Au catalyst incorporation in the GaAs NWs was also found to create defects[22, 54]. It was also found that all Au assisted NWs introduce centers which could

be related to strong non-radiative recombination centers in GaAs[55]. This excluded Au from many device applications and research was extended to use of other material as catalysts.

Although Ga assisted whiskers in the  $\mu\text{m}$  range were grown through VLS techniques in 1960s [47], it was in the early 2008, Morral et al. [17] demonstrated the growth of self-assisted GaAs NWs on GaAs substrates. They further showed that presence of  $\text{SiO}_2$  played an important role in the Ga droplet nucleation and the formation of nanocraters. Jabeen et al. [20] obtained self-assisted GaAs NWs on Si substrates. Later in 2010, self-catalyzed GaAs NWs were grown on Si (111) substrates exhibiting ZB structures without any twin planes[56]. Krogstrup et al. determined the correlation of structural phase distribution with the different V/III ratio and growth temperature at the interface.

**2.2.2 Crystal phases in GaAs NWs.** Although the formation of WZ or ZB structure depends on the initial nuclei in the NW growth, GaAs exist in cubic ZB crystal phase in bulk and thin film form but often adopt the WZ structure when it is grown as NWs.[57]. By definition, ZB is stacked as ABCABCABC whereas; WZ is stacked as ABABAB, where each of the letters stands for a bilayer of III-V pairs. When one of this bilayer is displaced in a WZ structure, we get stacking fault defect, whereas twin planes occurs when an additional layer is stacked in a sequence for ZB structure[58]. Joyce et al. [59] showed that the V/III ratio determine the structure formation. A high V/III ratio gives a ZB and a low V/III provides a WZ structure. They also showed that the formation of ZB NWs is more favorable at a lower growth temperature due to low energy surface reconstructions for ZB surfaces. Using a nucleation model they established that the formation of the twins is governed by orientation and surface energy of external vapor-nucleus facets. Krogstrup et al. [56] also demonstrated well-controlled pure ZB GaAs NWs and the role of growth temperature on the structural change.

**2.2.3 Effect of alloying GaAs with Sb on NWs.** When Sb is introduced in GaAs NWs, it tends to form ZB GaAsSb NWs. Dheeraj et al.[29] showed that Sb decreases the chemical potential difference of the system and helps in increasing the material critical supersaturation. Since Sb is a heavier atom ( $z=51$ ) with longer covalent bonds than Ga and As, it tends to remain on the growth surface and act as a surfactant [60]. Sb has the potential to reduce the migration time at which the adatom diffuse, since the diffusion and migration of adatom play a major role in NW growth [10]. GaAs/GaAs<sub>0.89</sub>Sb<sub>0.11</sub>/GaAs structure was studied by Plissard et al. [30] where they found an abrupt shift from WZ GaAs to ZB GaAsSb. It showed that presence of Sb (11 at. %) could affect the crystal structure of the GaAsSb segment thereby changing the band alignment transitions of the NW system. As the at. % of Sb was increased to 15, its incorporation in the segment was found to reduce with increase in the growth temperature. They also found stacking faults on the other end of the segment towards WZ GaAs. This could be due to small traces of Sb after the switching sequence to GaAs. All the above reports suggested that alloying with incorporation of Sb leads to formation of ZB structure in GaAs NW system which could be due to the effect of Sb on the internal energies leading to lower supersaturation which favor ZB structure formation.

## 2.3 Heterostructured NW Systems

There are two architectures that can be used in the growth of heterostructured NWs: a) axial structure and b) core-shell structure. In an axial structure, the composition of the material can be varied in the growth direction. In the core-shell structure, the core growth takes place in the conventional way and for the growth of the shell, the growth parameters are varied for favoring radial growth. As shown earlier, Paek et al. [19] demonstrated that at constant Ga flux, there is an increase in the axial growth rate with an increase in the As flux.

A brief review of the heterostructured NW system grown through different methods, with absorption in the NIR region of interest is identified. Figure 2.2 shows the plot of energy gap versus lattice constant depicting different semiconductor materials.

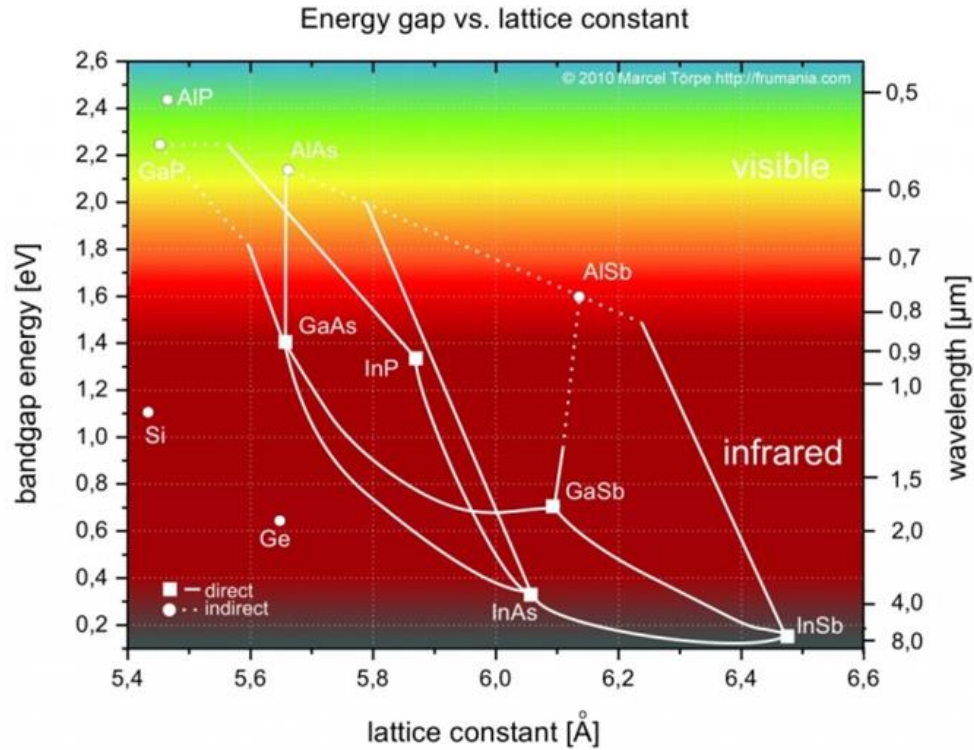


Figure 2.2. Energy band gap vs lattice constant [61].

**2.3.1 GaAs/AlGaAs NWs.** AlGaAs can be incorporated in the core-shell geometry of the NWs as p-AlGaAs or n-AlGaAs shell [62]. Research has been carried out for achieving uniform defect free epitaxial core shell NWs structures [63]. In this type of structure, the AlGaAs shell provides confinement around the GaAs core region and the non-radiative recombination at the GaAs-air interface is minimized. Photoluminescence analysis shows that for a low excitation power density, there is a broad emission band from ~1.46 to 1.51 eV at 10K [64]. Based on the amount of Al, the energy band can be shifted. However, the energy band gap ranges from 1.45 eV to 2.0 eV which doesn't cover the desired telecommunication optical window of 1.3 or 1.55  $\mu\text{m}$ .

**2.3.2 InAs/InAsSb NWs.** The InAsSb alloy, with one of the highest electron mobilities and saturation velocities is a promising material in optoelectronic and sensor applications. The bandgap of this material vary very slowly with its composition allowing a broad spectral response. In comparison to mercury cadmium telluride (MCT), InAsSb is more stable, high mobility with good acceptor and donor impurities. With its large band gap tunability from (2-8  $\mu\text{m}$ ) and the above properties, it is considered as an alternative for the commercially available MCT detectors. Work has been performed on Au assisted [65, 66] as well as self-seeded InAsSb NWs [67]. It was found that the axial and radial growth rate of these structures show opposite trend with increasing group V/III flow rate ratio [19, 68]. The Sb composition determines the growth rate of the NWs. In devices, made from structures like InAs/InAsSb, the strain is relaxed by the radial growth of InAsSb segment after the InAs stem [69]. A cutoff wavelength of 5.7  $\mu\text{m}$  has been reported which is claimed to be the longest cutoff wavelength for any nanowire device so far[69]. Hence these heterostructured NWs are suited in the MWIR device applications.

**2.3.3 InGaAs NWs.** InGaAs NWs have been fabricated by many growth techniques [4, 70]. GaAs/InGaAs/GaAs axial heterostructured NWs have been studied. With the increase in the In incorporation, there was a linear increase in the NW length during the growth. Optical study of this nanostructure through temperature dependent photoluminescence shows emission in the range of 0.93 $\mu\text{m}$  to 1.02  $\mu\text{m}$ [4]. For further shift in the emission wavelength, increased amount of In is needed in the III-V composition which adversely affects the NW density[71]. It was also observed that due to a large difference in the diffusion length of In and Ga the shape and height of the NWs are also deleteriously impacted. Nevertheless, for device fabrication, precise control on the growth is essential. Taking the expensive nature of Indium and its effect on shape and structure of NWs, an alternative system is more desirable.

**2.3.4 GaAs/GaAsSb NWs.** GaAsSb NWs have been grown as inserts in GaAs NWs by molecular beam epitaxy (MBE); both with Au assisted [15] and self-catalyzed method [30]. As in the case of InAsSb NWs, an immediate transition from the WZ GaAs to crystalline ZB GaAsSb is generally observed. At the transition from GaAsSb to GaAs, the occurrence of defects like twinning planes and 4H polytype GaAs has been found [15]. For self-catalyzed GaAsSb NWs as studied by Plissard et al. [30], even a very low Sb (approximately 11 at. %) results in abrupt changes in the structures of WZ GaAs to defect-free ZB GaAsSb.

An optical study was also performed on GaAs/GaAsSb NWs. Photoluminescence spectra exhibit peaks from 1.273 to 1.249 eV for 13.7 at. % Sb. Along the length of the NW with a GaAsSb insert, type I and type II transitions are observed. Type I transition are found to be dominant in the central Sb rich region of the ZB GaAsSb insert (insert refers to one which is embedded along the axis of the NW) whereas type II transition is observed near the interface where there is variation in the Sb concentration [9]. Maximum Sb incorporation is found in the bare core NW having a longer GaAsSb insert. There is an increase in the axial growth rate of the GaAsSb inserts with the increase in the Sb incorporation along the length of the NWs [39]. As per Heiss et al. [72], WZ GaAs/ZB GaAs heterojunction have type II band alignment in a NW structure where the electrons are confined to the ZB GaAs and the holes to the WZ GaAs. In case of ZB GaAs/ZB GaAsSb, for Sb composition < 40% as shown theoretically, a type II alignment results due to the electron confinement in ZB GaAs and the holes to the ZB GaAsSb [9, 73].

The GaAsSb NW by itself [15] grown on a GaAs (111)B substrate, exhibits rotational twins around its (111)B growth axis, with an equal amount of twinned and untwinned orientations. More recently, Plissard et al. [30] demonstrated the growth of a GaAs/GaAsSb core with AlGaAs shell using the Ga self-catalyzed technique. The Sb composition used in the

GaAsSb core was 30 at. %. Unlike other III–V alloys such as AlGaAs, GaAsSb requires more accurate control in the composition due to the presence of the two competing group V species with differing sticking coefficients. For instance, Ga growth rate was reported [41] to affect the Sb incorporation in the NW due to both the differences in the sticking coefficients and the bonding, although its effect on the PL results was not reported. Thus, the composition of GaAsSb alloy not only seems to depend on the flux ratios but also on the individual fluxes.

In the core structure, there is a competition between As and Sb in the incorporation into the GaAsSb insert [50, 74]. The Sb concentration is found to be high in the center of the wire as compared to the edges in a core configuration. Such variation in Sb concentration was not observed for the core-shell structure.

A detailed quantitative analysis of Sb distribution in GaAsSb NWs was performed by Kauko et al.[75]. All the GaAsSb segments under this study ranged from 109- 156 nm in length. Both high annular angle dark field scanning transmission electron microscope (HAADF STEM) and electron dispersive x-ray spectroscopy (EDX) point analysis showed a suggested change in the concentration gradient [75] in the Sb which was due to the out diffusion of Sb during the NW growth. EDX point scans showed a strong Sb concentration in the first two-thirds of the NW and it flattened out towards the top of the NW. This also explained the cross sectional Sb concentration profile using a model for diffusion of Sb in the hexagonal NWs employed in combination with quantitative analysis of HAADF STEM. The Sb concentration peaks and remains high at the center of the NW with a reduction at and near the surface. For small variation along the radial Sb concentration, quantitative analysis of HAADF STEM in combination with a model for diffusion of Sb is considered to be superior to EDX.

**2.3.4.1 Photoluminescence study of the GaAs/GaAsSb.** Figure 2.3 shows the power dependent PL spectra for a WZ GaAs/AlGaAs core-shell NW with a ZB GaAsSb core insert. Todorovic et al.[76], found three different set of PL emission, from band A (1.35-1.45 eV), band B (1.50-1.55 eV) and band C (1.58-1.65 eV). A power dependent PL spectrum showed that the peak at 1.39 eV did not exhibit any blue shift in the peak with the increase of excitation of power. This is considered as a signature of type I band alignment and was assigned to transition of the carriers within the GaAsSb due to confinement of both the electron and holes in the GaAsSb insert. Dark field TEM on these NWs shows the presence of WZ NW with a ZB insert and stacking fault (SF) between the ZB and WZ transition. The presence of the type I emission was considered to be indicative of stacking faults (SFs) quite far from the ZB inserts, thereby having no effect on the carrier recombination taking place in the insert. An unidentified peak at 1.42eV was also observed at higher excitation intensities. For the PL emission occurring at about 1.52 eV in band B, which has been attributed to type II band alignment originating from the transition between the energy states of SFs and the WZ GaAs core part of the NWs.

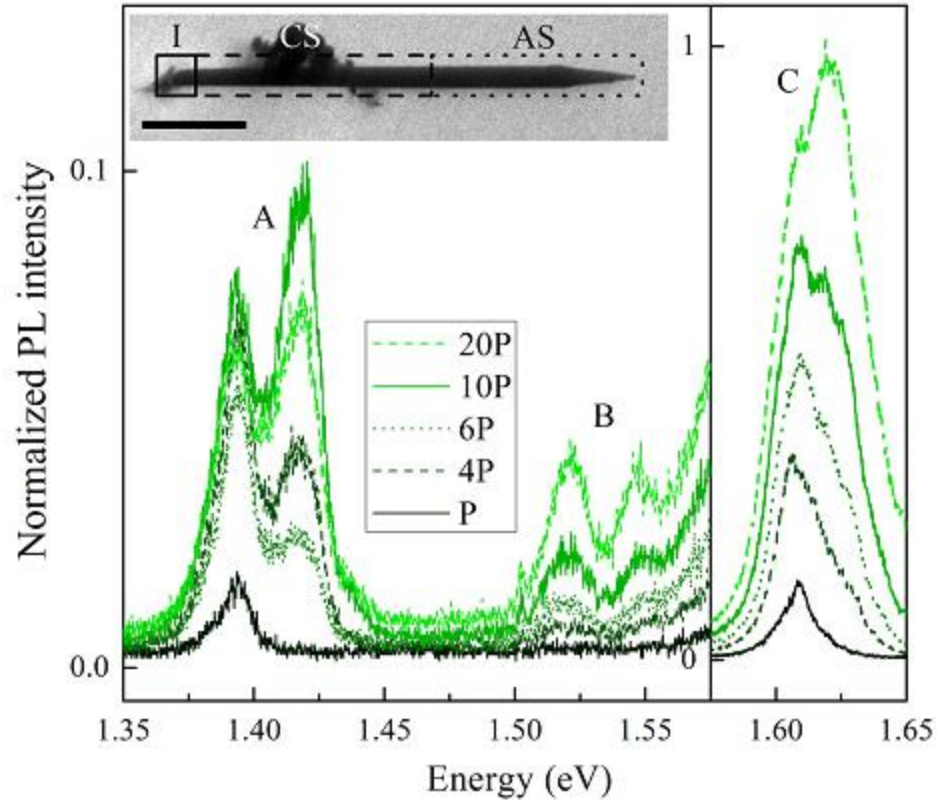


*Figure 2.3.* Low temperature power dependent PL spectra ( $P = 2.55 \text{ W/cm}^2$ ) of a NW together with 30 kV BF STEM image (inset). The scale bar in the inset is 500 nm. (Reprinted with permission from [91], Copyright 2011 IOP Publishing).

#### 2.4. P-type Doping in NWs

Controlled doping plays a major role in making nanowires a technology reality. In order to effectively incorporate dopants in the nanowires, it is important to understand its role in the growth mechanism. Generally for nanowires growing from the catalysts droplet, growths take place via the vapor liquid solid (VLS) technique. The path of incorporation of the dopants in this technique would generally be from the liquid droplet and also from the sidewall that results in the radial growth of NWs. Dopants with a high diffusion coefficient are sought for improved incorporation. The typical dopants for the III-V materials are the Be and Te [77, 78] with high diffusion coefficients. Casadei et al. [36] correlated the electrical conductivity with the dopant

incorporation. They have explained it in core-shell structures (Figure 2.4); where the incorporation can take place through 3 different paths:

- (i) Axial incorporation through VLS mechanism.
- (ii) Radial incorporation through the VS mechanism.
- (iii) Diffusion of the dopant through the shell to the core in the volume of the NW.

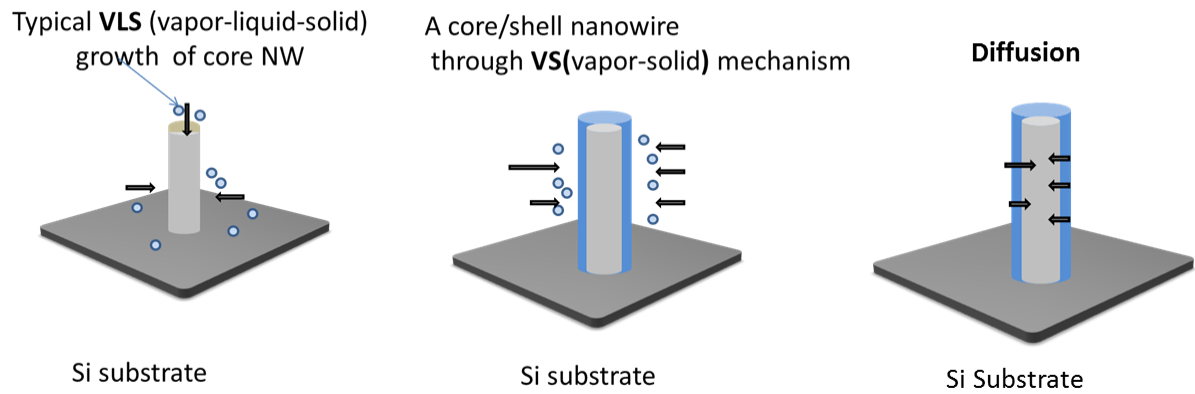


*Figure 2.4.* Processes that influence the doping and diffusion of Be dopants in NWs.(Adapted after [36], Copyright 2013 American Institute of Physics).

Based on the diffusion process during the growth, the diffusion profile has been determined in the case of Be [79, 80]. It was found that during the axial growth, there would be a steady concentration of the Be adatoms on the NW sidewalls. Diffusion of the Be adatoms from the surface to the NW core was driven by the gradient of the Be concentration.

Yu et al. [80] had explained the Be diffusion in GaAs using the kick-out mechanism in thin films, where it is assumed that a doubly positively charged group III element self-interstitials governs the Ga self-diffusion. A much lower diffusivity of Be was observed under out diffusion conditions than under in-diffusion condition. In 1977, Ilegems [79] from Bell laboratories found that Be doping up to  $5 \times 10^{19} \text{ cm}^{-3}$  in GaAs using molecular beam epitaxy. Mobilities of these Be doped GaAs layers were found comparable to those of liquid phase

epitaxy (LPE) material. Room temperature photoluminescence efficiencies under As stabilized conditions were comparatively lower than those from LPE grown material. The lower efficiency might be due to the contamination of the specific dopant material which was not observed in similar doping condition for Sn doped GaAs. Be doping incorporation in the GaAs NWs has also been investigated [36] by the electrical measurements of nanowires for different doping profiles. Improved Be incorporation through the side facets were achieved for core-shell configurations of the NWs which can be tuned between  $6 \times 10^{17}$  and  $5 \times 10^{19} \text{ cm}^{-3}$ .

Dheeraj et al.[37] reported on the comparison between Au assisted and Ga assisted Be doped GaAs NWs grown by molecular beam epitaxy. They performed a systematic analysis on the growth, structural and electrical characterization of the doped NWs. The growth rate was reduced for the case of Au assisted GaAs NWs than as compared to that for Ga assisted NWs with the same Be flux. The selected area electron diffraction (SAED) patterns of these NWs showed that the Au assisted NWs consisted of mainly WZ structure with few stacking faults whose density differed from one NW to other whereas the Ga assisted NW predominantly had ZB with few twin defects. Electrical characterization showed a symmetric I-V characteristic with higher current for the Ga assisted one. 2-probe measurements were performed and the NW resistivity varied between  $1.7 \times 10^{-2}$  and  $5.9 \times 10^{-2} \Omega \cdot \text{cm}$ .

Be doping also affects the NW growth dynamics. It is speculated that Be at high dopant concentrations may increase the steady-state chemical potential of catalyst droplet [81], leading to the corresponding decrease of liquid and adatom supersaturation during growth. This causes a transition from the typical inverse growth rate dependence of length (L) over diameter (D) where for small nanowire diameters the axial growth rate is suppressed. Taking this L versus D dependence, different models have been proposed. The diameter dependence L versus D

relationship for low Be concentration fits well by  $L \propto 1/D^2$ . This equation is more relevant in case of diffusion related growths and is derived between the relation between adatom diffusion length and the adatom surface area[82]. This effect in the doping behavior excludes the change in the adatom diffusion length as a cause of L (D) behavior. Previous studies based on different dopants like Be and Si[38] have shown a reduction in the length of NW and an increase in the tapering with the doping. These results suggests that the dopant present on the NW surfaces will influence the growth as it may affect the diffusion length through the surfactant effect or surface passivation resulting in a more radial growth rather than axial one and also effecting the morphology of the NW. Furthermore such suppression of adatom diffusion length would result in the production of core-shell structure in the nanowires.

## 2.5 Summary

A literature review is presented on different As-Sb materials system leading to GaAs/GaAsSb NWs as prospective NWs for application in the NIR region for photodetection. Depending on Sb composition in GaAsSb, the ZB type of structure is more favorable which can be advantageously used for different optoelectronic applications. A brief literature report on the p-type doping of the NWs with Be dopant has also been presented. For higher Be incorporation, its surface diffusion in the NW during growth becomes important.

## CHAPTER 3

### Experimental Methodology

#### 3.1 Introduction

Precise control over the NW chemical composition, structure, size, morphology, position and growth direction is required for device integration, as these parameters dictate the physical properties of the NWs [16] and the feasibility and the final performance of the device. Self-catalyzed NW growths were performed by molecular beam epitaxy. After the growth, the NWs were ex-situ characterized by scanning electron microscope (SEM), X-ray diffraction (XRD), photoluminescence (PL), Raman analysis, transmission electron microscope (TEM) and ellipsometer. Some of the characterization techniques were performed at different facilities, for example, some of the Raman measurements were carried out at the Shared Materials Instrumentation Facility at Duke University after a certified training, energy dispersive x-ray spectroscopy and Conventional and scanning transmission electron microscopy were performed at North Carolina State University (NCSU) and X-ray diffraction at Wake Forest University.

In this Chapter, a brief description of the MBE system and its various components are discussed. A detailed growth procedure has been provided with a brief description of the above mentioned characterization techniques that have been used in this dissertation for ascertaining the NW properties.

#### 3.2 Molecular Beam Epitaxy (MBE)

MBE is considered to be one of the important deposition techniques for growth of highly crystalline non-equilibrium semiconductor materials. It is a research and production tool as well for epitaxial film growth, which allows in-situ surface analysis tools to obtain a real time analysis

of the surface and its environment. The basic principle behind MBE is atoms or clusters of atoms which are formed by heating an element source are allowed to travel in an ultra-high vacuum (UHV) condition such that they deposit on a heated substrate for producing thin films. The MBE growth takes places in an UHV environment in order to avoid contamination of the material which affects the electrical, structural and film morphological properties. The purity level is one of the important factors in MBE system. For the growth of a sufficiently epilayer of high purity, a background vacuum pressure of  $10^{-11}$  Torr is required. Though it has low growth rates, it provides precise control on each monolayer growth on substrates samples. .

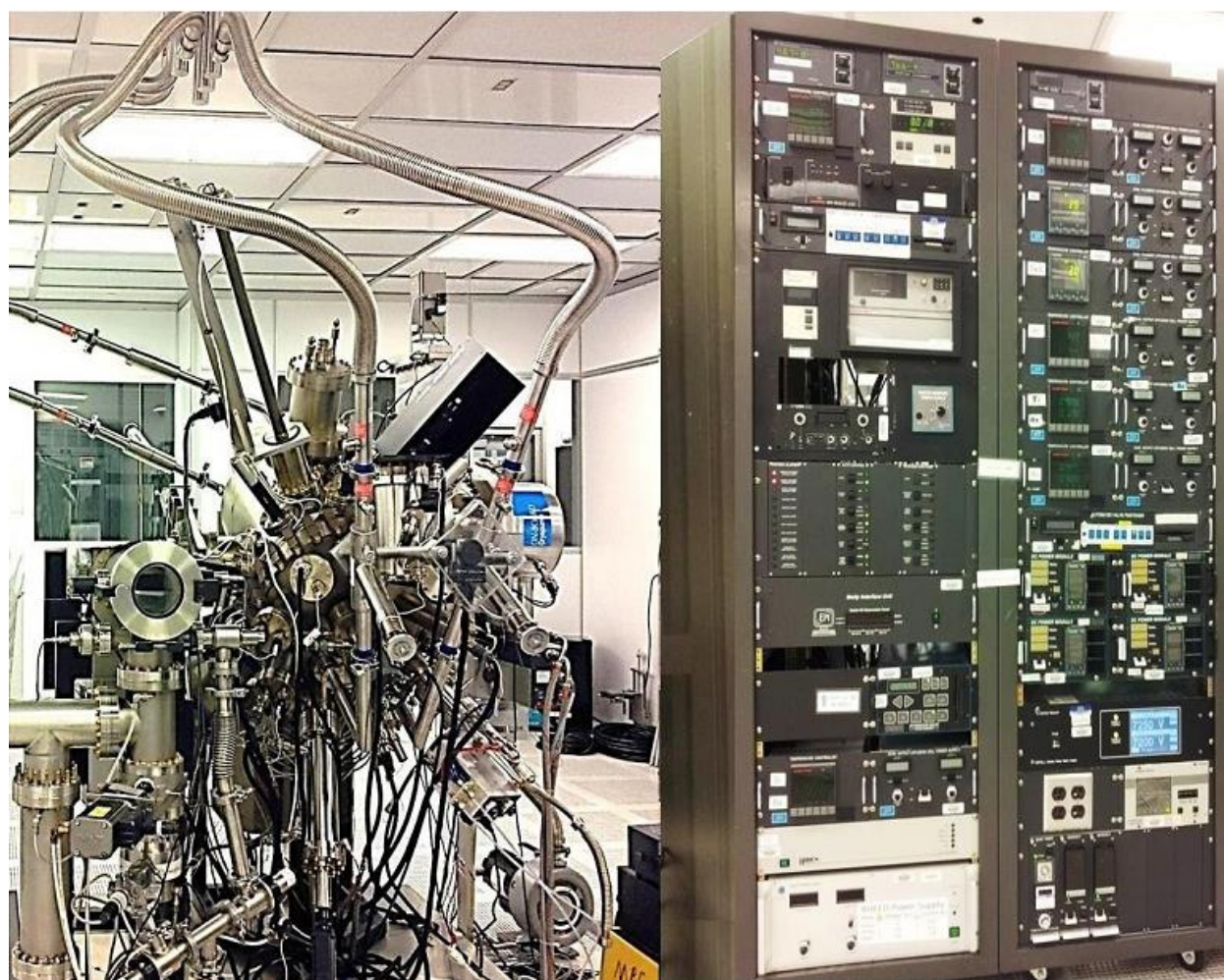


*Figure 3.1.* EPI 930 molecular beam epitaxy system.

For this study a Veeco EPI 930 solid source MBE was used in the growth of the nanowires (Figure 3.1). The EPI 930 MBE had 5 Knudsen effusion cells, one Sumo cell, two valved crackers and a UNI-Bulb plasma nitrogen source. The MBE system predominantly had sources from group III and V periodic table and a schematic of its arrangement in the system is highlighted in Figure 3.2 below. The group III elements include Ga, In and Al and group V comprised of N, As and Sb. For dopants the elements used were Be and Si. The group III elemental source Ga source was placed in a 7N purity SUMO cell, incorporating a specially designed 200gm crucible. The dual filament Ga SUMO cell was used in a hot lip configuration where the majority of the power goes to the tip filament. This results in the tip operating at higher temperature than the primary filament. In this type of arrangement, the oval defects are reduced by the hot lipped operation which reduces the Ga droplet formation in the crucible. These defects are generally caused due to the evaporation and re-evaporation of the Ga cluster near the lip of the crucible. The other advantages of the SUMO cell are the ability to sustain large capacity of Ga which increases the replenishment time and avoids a prolonged long term depletion effect, a shutter flux transient. It also reduces the defect densities when the SUMO cell is operated with 100% power to the tip filament.

The group V elements consist of Sb and As along with the cracking filament as shown in Figure 3.3. The flux from these sources can be controlled by heating the bulk source or the cracker. Each of the valved crackers are associated with automated needle valve positioner that provide precise control of the flux.

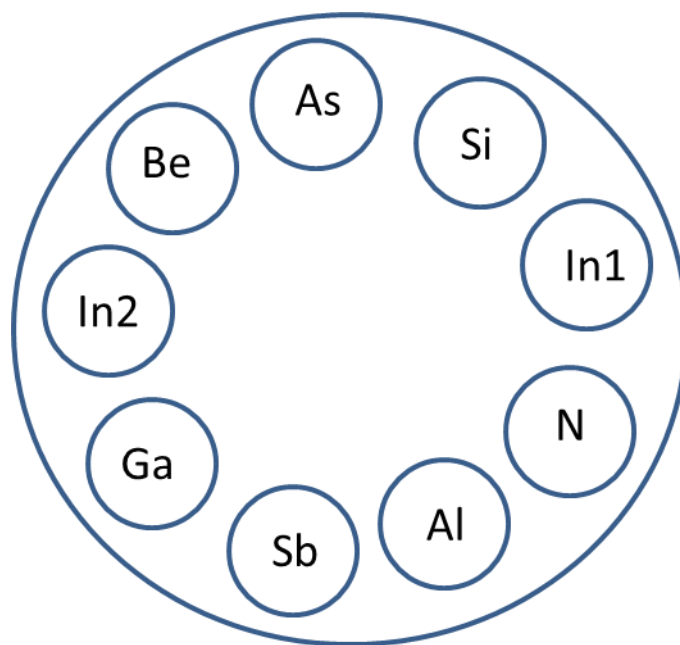


Figure 3.2. Schematic diagram of the different sources in the Veeco EPI 930 MBE system.

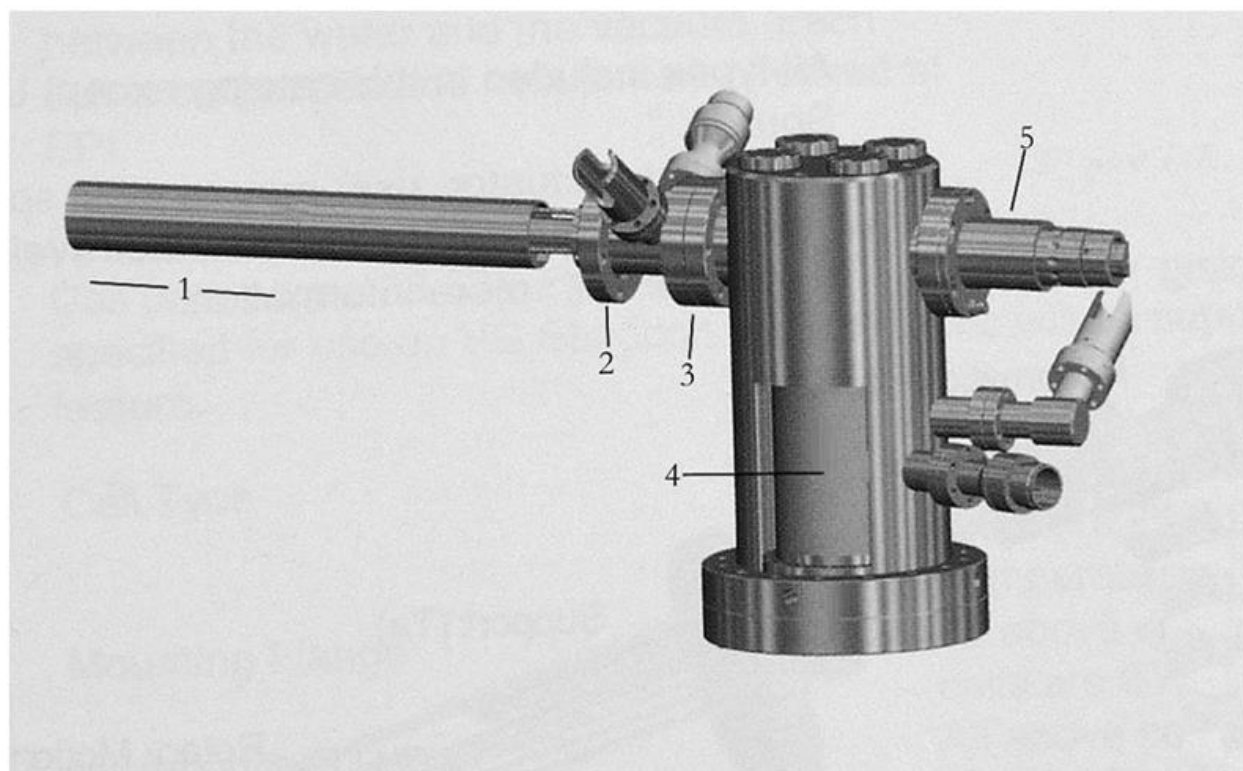


Figure 3.3. Cutaway view of valved oven for high-vapor-pressure elements (e.g.,  $\text{As}_4$ ,  $\text{P}_4$ , etc.):

(1) internal hot zone for molecular cracking of tetramers to dimers, (2) mounting flange, (3)

valve seat for isolating charge, (4) externally heated large volume PBN insert crucible and (5) controlled leak valve stem. (Reprinted with permission from [83]. Copyright 2002 Elsevier).

Epiready Si wafers were purchased from Virginia semiconductor, Inc. These were  $\langle 111 \rangle \pm 0.9^\circ$  in orientation,  $100 \text{ mm} \pm 0.3 \text{ mm}$  in diameter, resistivity  $< 0.005 \Omega \cdot \text{cm}$ , a thickness of  $500 \mu\text{m} \pm 25 \mu\text{m}$  and boron as the dopant. These wafers were cut in to  $1 \times 1 \text{ cm}$  square pieces that were loaded into a Veeco uni-block sample. For some of the growths, the wafer samples prepared were of  $1 \times 1 \text{ inch}$  which was later cut to smaller pieces that could be used for other characterization techniques.

Despite many studies on GaAs NWs [16, 82], the nucleation and growth mechanisms have not been fully clarified yet. Therefore, a deeper understanding of the mechanisms and processes involved in NW growth is essential.

**3.2.1 Refraction high energy electron diffraction (RHEED).** RHEED is an in-situ technique which provides possibility of monitoring the evolution of morphology and crystal structure during the growth. It consists of an electron gun to produce a high electron beam, in our case it was 12kV which is directed to the sample surface at a grazing incidence of  $1-3^\circ$  for a low penetration depth and to get the sensitivity for few outermost atomic layers. This diffracted beam is then allowed to fall on a fluorescent screen on which different patterns are formed based on the sample surface. So, based on the RHEED pattern, the crystal lattice or the roughness can be obtained during a 2D or 3D surface growth. A much detailed study of RHEED can be found elsewhere [84-86]. In our study of the samples during the growths, we used RHEED for inferring the 3D/island growths by observing the spotty pattern as illustrated in Figure 3.5 below. The system used was a kSA 400 analytical RHEED system manufactured by k-Space Associates, Inc.

This system included a 12-bit firewire camera, PCI-based digital frame grabber and the latest acquisition software (v5.13).

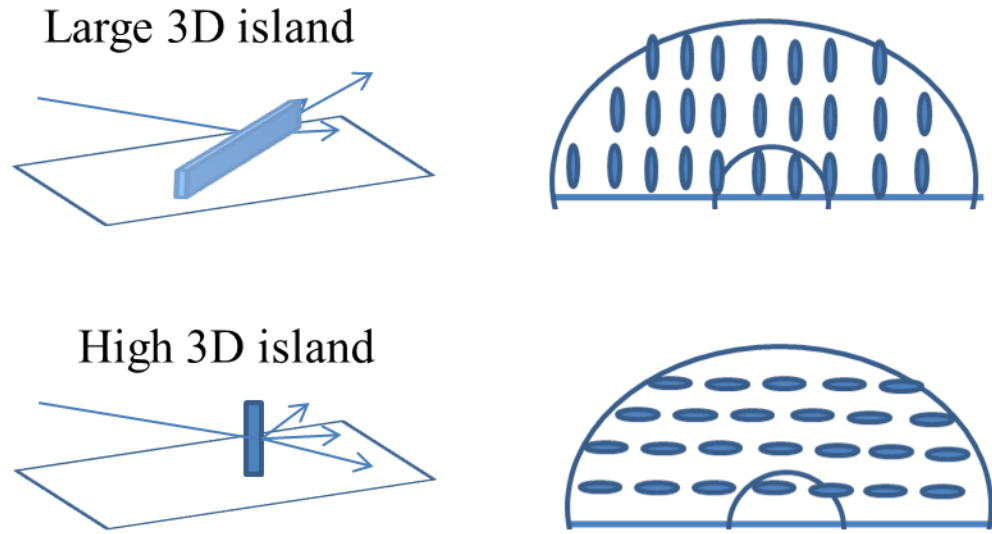


Figure 3.4. Surface morphologies deduced from the RHEED patterns. (Adapted from [87]).

### 3.3 Growth Process of GaAs/GaAsSb NWs on Si (111) Substrates

1. Initially the wafers used were epi-ready which were not chemically etched before loading into the MBE system. This was later changed and the wafers were chemically etched before loading into the MBE system. The growth steps after loading the wafers are listed below for a core NW configuration. The wafers are heated such that the growth temperature of 600°C or 620°C was achieved.
2. After annealing for 5 minutes, the Ga shutter is opened for few seconds (15 sec) for the Ga droplet formation. Then the As flux is initiated for the growth of a GaAs stem of the NW for few minutes based on the V/III ratio. In the case of doping NWs, the dopant is allowed along with the As.
3. Once the GaAs stem is formed, the Sb flux is begun at the same growth temperature to form a GaAsSb segment in the GaAs NW.

4. Once the desired length of the GaAsSb segment is formed, only the Sb flux is terminated thus forming a GaAs cap for the NWs.
5. In order to remove the Ga droplet, the substrate is cooled under As overpressure until the substrate temperature reaches 500°C.

For the growth of a shell, after the step 4 above, the growth temperature is reduced to 465°C after which both Ga and As shutters are opened for the desired duration to allow growing a GaAs shell.

After the successful growth of the NWs, the morphological features of the NWs were examined using a scanning electron microscope (SEM). The structural and optical studies were investigated using x-ray diffraction (XRD), HR-TEM, 4K photoluminescence and Raman spectroscopy. The physical principles of these techniques are described briefly below.

### 3.4 Characterization Techniques

Following is a brief description of the different tools used for characterizing the NWs.

**3.4.1 Scanning electron microscope.** In a typical SEM, an electron beam is thermionically emitted from an electron gun fitted with a tungsten filament cathode gun. The type of signals produced are secondary electron (SE), back scattered electron (BSE), characteristic X-rays, specimen current and transmitted electron. The signals result from the interaction of the electron beam with the atoms at or near the surface of the sample. The common detection mode is the secondary electron imaging mode, which can result in images having resolution <2.5 nm [88].

All the samples were scanned using a Carl Zeiss Auriga-BU FIB FESEM Microscope as shown in Figure 3.5 with the electron beam at 10kV. The samples were generally cut to a size of 1x1 cm<sup>2</sup> for the SEM imaging. Both top view and side view imaging was done. The sample stage

was also tilted to  $45^\circ$  to get a  $45^\circ$  side view of the NWs. For conventional SEM, the samples should be electrically conductive at the surface and electrically grounded to avoid charge accumulation. Non-conducting samples are coated with electrically conductive material like gold, platinum etc. But due to the semiconductor nature of our samples, they are scanned without coating.



*Figure 3.5. Carl Zeiss Auriga-BU FIB FESEM Microscope.*

**3.4.2 Photoluminescence (PL).** This type of spectroscopy is a non-contact, nondestructive method of probing the electronic structure of the materials. In a heterojunction material, the smooth and atomically abrupt interfaces are necessary for good optical and electronic reflections. In this process, when the light of sufficient energy is incident on the material, the photons are

absorbed and are excited to higher electronic states. When these electrons relax, the radiative relaxation process results in photoluminescence. The PL spectrum provides the transition energies which contains wealth of information on the electronic states of the material. The variation of the PL intensities can be used to determine the nature of the type of the transitions. Below are some brief points about the various application of this process.

- **Band gap determination:** Based on the spectral response of the PL, the electronic band gap of a semiconductor material can be analyzed. This also provides a means to quantify the elemental composition.
- **Impurity level and defect detection:** Low temperature PL spectra are a unique way of determining the spectral peaks associated with impurities contained in the semiconductor material. Its high sensitivity to the peaks maximizes the possibility of identification of the intentional or unintentional impurities that can strongly influence the device performance and the material quality.
- **Recombination mechanisms:** The intensity of the PL emission is determined from the amount of radiative and non-radiative recombination rates. Radiative recombination contributes in the intensity where as in non-radiative recombination; it reduces the number of photon generation, thereby reducing the overall intensity. Again based on the non-radiative recombination rates, the impurities can be determined in the material. So, it can act as a good monitoring technique in the production of high quality material.

In our lab, we used a He Ne laser lasing at 632 nm as an excitation source with a 0.32 m double grating monochromator for wavelength dispersion along with an APD cryogenic system for the PL measurement with varying temperature of 4°K-300°K. With a Si detector, the

detection range extending from  $\sim 400$  nm to 1200 nm could be obtained. Figure 3.6 shows the experimental setup of the facility used.



*Figure 3.6.* Photoluminescence setup.

**3.4.3 Raman spectroscopy.** Raman spectroscopy is a spectroscopic technique used to observe the vibrational, rotational and other lattice vibration frequency modes. It is a versatile and relative standard tool for the characterization of materials giving detailed information on crystal structure, phonon dispersion, electronic states, composition, strain in bulk materials, thin film and nanostructures [89, 90]. When light is incident on a molecule, it can either be absorbed or scattered. This incident light can induce many processes. It can interact with the molecule such that there is polarization of the electron cloud around the nuclei of the molecule. If only the electron polarization is involved in the scattering, then it is elastic scattering. Apart from the polarization, if the scattering involves nuclear motion, then either the molecule receives energy from the incident photon or provides energy to the scattered photon. This inelastic scattering

process where there is a difference of one vibrational unit of energy between incident photon and scattered photon, known as the Raman Effect, is the energy of a vibration of the scattering molecule. Raman scattering involves two energy packets where either the photon loses energy, known as Stokes shift, or where the photon gains energy, known as anti-Stokes shift. A monochromatic light source with high power density is necessary in Raman spectroscopy to excite a sufficient number of Raman events in a sample. The mass of the atom and strength of the bonds between them influences the lattice vibration frequency. Raman shift is small for heavy atoms and weak bonds where as it is large for lighter atom and strong bonds. This explains shift towards lower frequency for GaAsSb as compared to GaAs NWs [91]. Prior to the interaction with the laser, most of the molecules would be in the ground vibrational state. This makes most of the scattering to be Stokes Raman scattering.

The Raman measurements were performed using a Horiba Jobin Yvon LabRam ARAMIS with a spectral resolution of  $0.6 \text{ cm}^{-1}$  for spectral dispersion. A HeNe laser of 632 nm wavelength was used for excitation of the molecules. It had a spectral range of 200 nm to NIR with a spectral resolution of  $0.6 \text{ cm}^{-1}$  at 680 nm with 1800 gr/mm grating. The instrument was calibrated using a standard Si sample to observe a peak at  $520 \text{ cm}^{-1}$ . The Raman signals were collected by using a multichannel air cooled charge coupled device and Lorentzian curve fitting was carried out for obtaining the peak frequency value.

**3.4.4 Atomic Force Microscopy.** The surface morphology was studied using Agilent Technologies 5600 LS Atomic Force Microscope. An automated tip mode was used to scan the test area with a minimum damage to the sample surface. A sampling area of  $5 \times 5 \text{ }\mu\text{m}$  square was used to observe the surface roughness. After the data acquisition AFM analysis freeware tools

such as SPIP was used to correct for any tilt/offset in the data. The surface roughness was estimated from the root mean square (rms) value of the intensities in the scanned data.

**3.4.5 X-Ray Diffraction.** X-Ray diffraction is one of the common techniques for the study of crystal structure and lattice parameters of materials. In this diffraction experiment, the incident x-ray having the wavelength which is comparable to the spacing between the atoms in the material follows the Bragg's law. Based on Bragg's law, this relation between angle of incident, wavelength of X-rays and the distance between the crystal planes can be shown as  $2d\sin\theta = n\lambda$ , where  $d$  is the interplanar spacing,  $\theta$  is the angle of incidence of X-ray,  $\lambda$  is the wavelength of the X-ray and  $n$  is the number of planes. For a cubic crystal with lattice constant,  $a_0$ , interplanar distance is given by,  $d_{hkl} = \frac{a_0}{\sqrt{h^2+k^2+l^2}}$  with the diffraction peak at angle  $2\theta$ , where  $2\theta_{hkl} = 2\arcsin(\frac{\lambda\sqrt{h^2+k^2+l^2}}{2a_0})$ . Depending on the crystal structure, certain possible diffracted angles are obtained by scanning it through a range of  $2\theta$  angles. Using the X-ray diffraction spectra, information such as the crystallographic structure, strain, relaxation, tilt, lattice parameter and dislocation densities can be determined.

All the X-ray diffraction scans were performed using Bruker's D8 Discover instrument as shown in Figure 3.7 with a Da Vinci diffractometer in the standard Bragg Brentano para-focusing configuration. This system was configured with a 2.2 kW Cu x-ray tube as the source. X-rays from the Cu  $K\alpha$  source has computer controlled incidence containing both  $K\alpha_1$  and  $K\alpha_2$  components.



*Figure 3.7. Bruker's Discover D8 X-ray diffraction system[92].*

**3.4.6 Transmission electron microscope.** A basic setup of a transmission electron microscope (TEM) can be seen in Figure 3.7. The electron gun accelerates the electron that originate from either a thermionic or a field emission source. This electron beam is controlled by electromagnetic lens and deflector coils[93]. The condenser lens condenses the beam's spread and controls the illumination on the specimen. This lens aperture limits the angular range of the electron that are allowed on the specimen. Hence it makes the beam parallel and remove high angle electron that suffer most from the lens aberration.

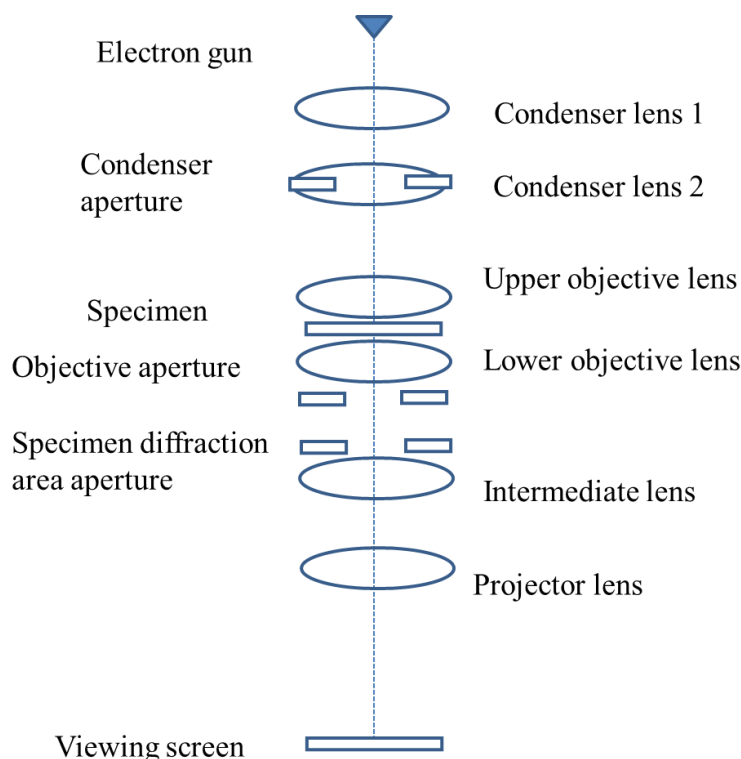


*Figure 3.8.* A schematic of the TEM set-up.

In most TEMs, the samples are placed between the upper and the lower objective lenses. The upper pole piece is used to make the highly focused electron probe in the STEM mode and the lower pole piece is responsible for the imaging in the conventional TEM (CTEM). In diffraction mode, an aperture is inserted in the image plane to restrict the area of the sample contributing to the diffraction pattern. This is called selected area electron diffraction (SAED). In STEM, the image is formed by scanning a probe (convergent beam) in a raster over the sample and collecting the transmitted beam from the probe position. The magnification of the image is determined from the area of the scanned surface rather than by lenses. Here the image intensity depends on the total signal collected during the time the probe was kept on the sample. In this work, the NWs images were acquired using CTEM and HRTEM, on a JEOL2010F and FEI Titan G260-300. The latter was equipped with aberration corrected STEM.

### **3.5 Conclusion**

Molecular beam epitaxial technique was used for the growth of the GaAs/GaAsSb NWs on Si (111) substrate due to its precise control of the adatoms that allows obtaining NWs with superior optical properties. It was also used in Be doping study of GaAs NWs. The growth steps are outlined. The basic principles of operation of different instruments used in the characterization of the NWs have been briefly reviewed and relevant experimental details have been provided.

## CHAPTER 4

### Study of Be Doping in Ga Assisted GaAs Nanowires

#### 4.1 Introduction

For effective implementation of NWs in miniaturized devices, the doping of the NWs needs to be researched extensively. Among various p type dopants, Be doping in NWs has been studied extensively [38, 62, 94]. As evident from the literature review, the studies are focused on single NWs and the results are scattered.

In this chapter a systematic and comprehensive approach is adopted in order to get a deeper insight into the effect of growth parameters with a detailed study on the NW core and shell configuration was performed. For morphological, structural and optical characteristic of the Be doped GaAs NW, characterization techniques, such as XRD, SEM, low temperature PL, Raman spectroscopy and STEM, were performed. This has enabled us to identify the relevant growth parameters that strongly influence Be incorporation in the NWs.

#### 4.2 Experimental Details

The GaAs NWs were grown using the EPI 930 solid source MBE system equipped with a Ga SUMO cell, Be effusion cell and an As valved cracker as described in details elsewhere [95, 96]. The Ga assisted NW growth was carried out on epitaxially grown Si (111) substrates with boron as dopant. For the core NW growth, the As<sub>2</sub> flux was maintained at a beam equivalent pressure (BEP) of  $2.4 \times 10^{-6}$  Torr and all growths were performed at 600°C. Growth was initiated by opening the Ga cell's shutter for 8 seconds prior to simultaneous opening of As and Be shutters. The core GaAs NW growth was carried out at 600°C and was grown for 4 minutes. Growth was terminated by closing the Ga and Be shutters simultaneously while the As shutter was closed after the growth temperature was below 500 °C. However, for the shell growth, the growth was

again initiated with the opening of the Ga and Be shutters along with As at the substrate temperature of 465°C for 4 minutes. Keeping the same Be cell temperature, both the core and shell were doped with Be. Figure 4.1 summarizes the growth parameters of the samples reported in this work along with the nomenclature adopted for easy identification of the samples.

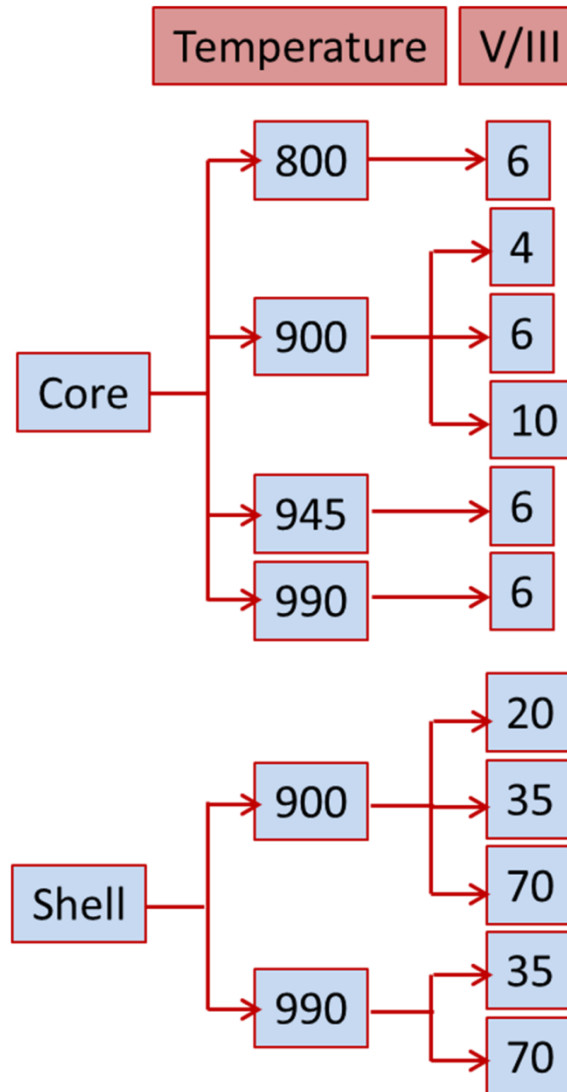


*Figure 4.1.* Summary of the growth parameters of the Be-doped NWs where the samples are divided based on the core/shell, Be cell temperature (°C) and V/III ratio.

### 4.3 Results

**4.3.1 Scanning Electron Microscopy.** Figure 4.2 displays the variation of NW density, diameter and 2D parasitic layer (defined as layer that grows at the base of the nanowires on the substrate) thickness with V/III ratio during core growth where the Ga flux was varied with the As pressure being maintained constant for the NWs grown at a Be cell temperature of 900°C. With increasing V/III ratio, the density of NWs increases (Figure 4.2 (a)), diameter decreases (Figure 4.2 (b)) and the 2D parasitic layer thickness decreases (Figure 4.2(c)) with the continuous 2D film transforming to more localized islands for V/III ratio of 10. Typical diameters and lengths of the NWs studied were in the range of 60-90 nm and 1-1.5  $\mu\text{m}$ , respectively. In addition to enhanced NW density and decrease in the diameter of NWs, there is also increase in the axial growth rate with increasing V/III ratio. The latter confirms the inverse length –diameter (L-D) relationship commonly observed in NWs grown by the VLS mechanism [97] and has generally been attributed to the rapid nucleation of the solid nanowires below the droplet driven by its supersaturation. This also prevents contiguous formation of a 2D parasitic layer. Although thin NWs of high density are grown at a V/III ratio of 10, the PL signals were weak; hence, most of the NW cores were grown at a V/III ratio of 6.

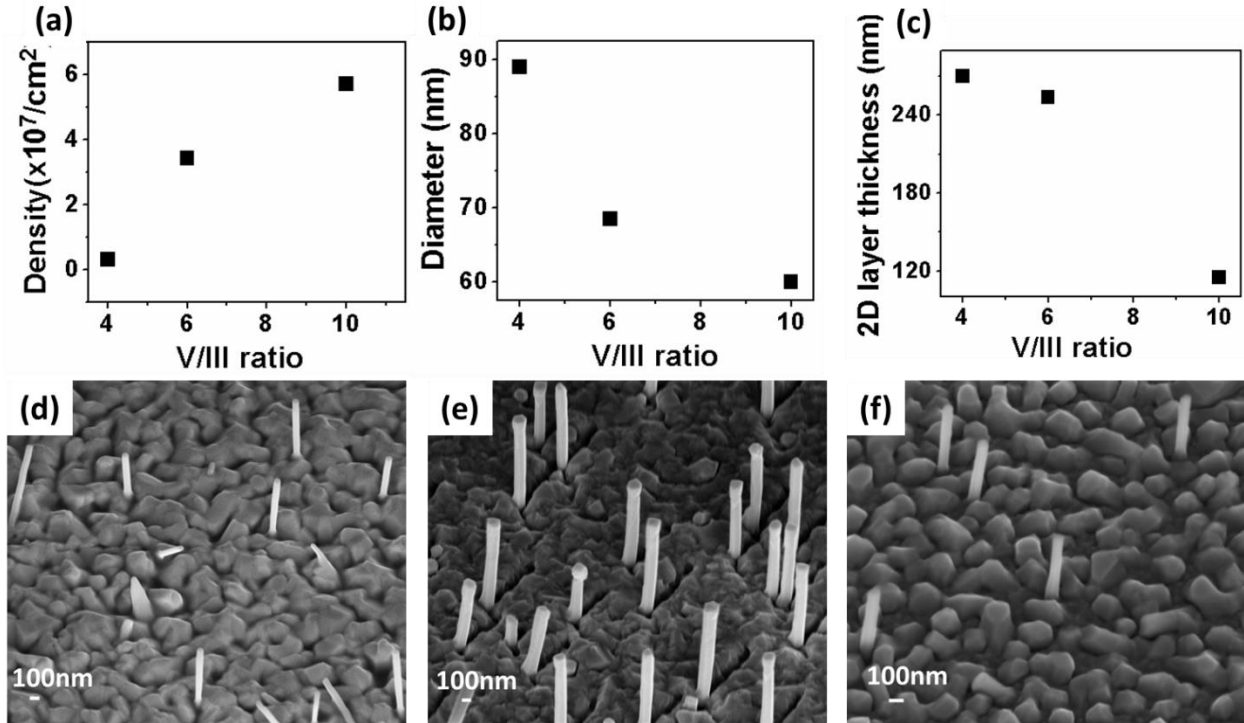


*Figure 4.2.* Variation of (a) NW density, (b) Diameter and (c) NW 2D layer thickness as a function of V/III ratio during core growth. SEM images of NWs with constant core V/III ratio of 6 and different shell V/III ratio of (d) 20, (e) 35 and (f) 70 at a Be cell temperature of 900°C.

The axial growth rate was also influenced by Be cell temperature as demonstrated in Figure 4.3. With an increase in the Be cell temperature from 800°C to 990°C, the axial growth rate and density of the NWs are reduced with simultaneous enhancement in the NW diameter and the two-dimensional islands were found to be more localized (Figure 4.3). Be act as a substitutional (reactive) impurity and form strong bond with GaAs NWs[98]. During the segregation process, an exchange reaction between the adatoms of the growing layer (GaAs) and the Be (acting as a surfactant) takes place which results in subsurface incorporation[99]. In order to migrate, the atoms have to break the existing bonds (including those with Be) and this leads to higher barrier for hopping. This reduces the surface diffusion length of the adatoms which results

in its accumulation around the radius and promoting the radial growth. This also explains the reduction in the axial growth as shown in Figure 4.3(a).

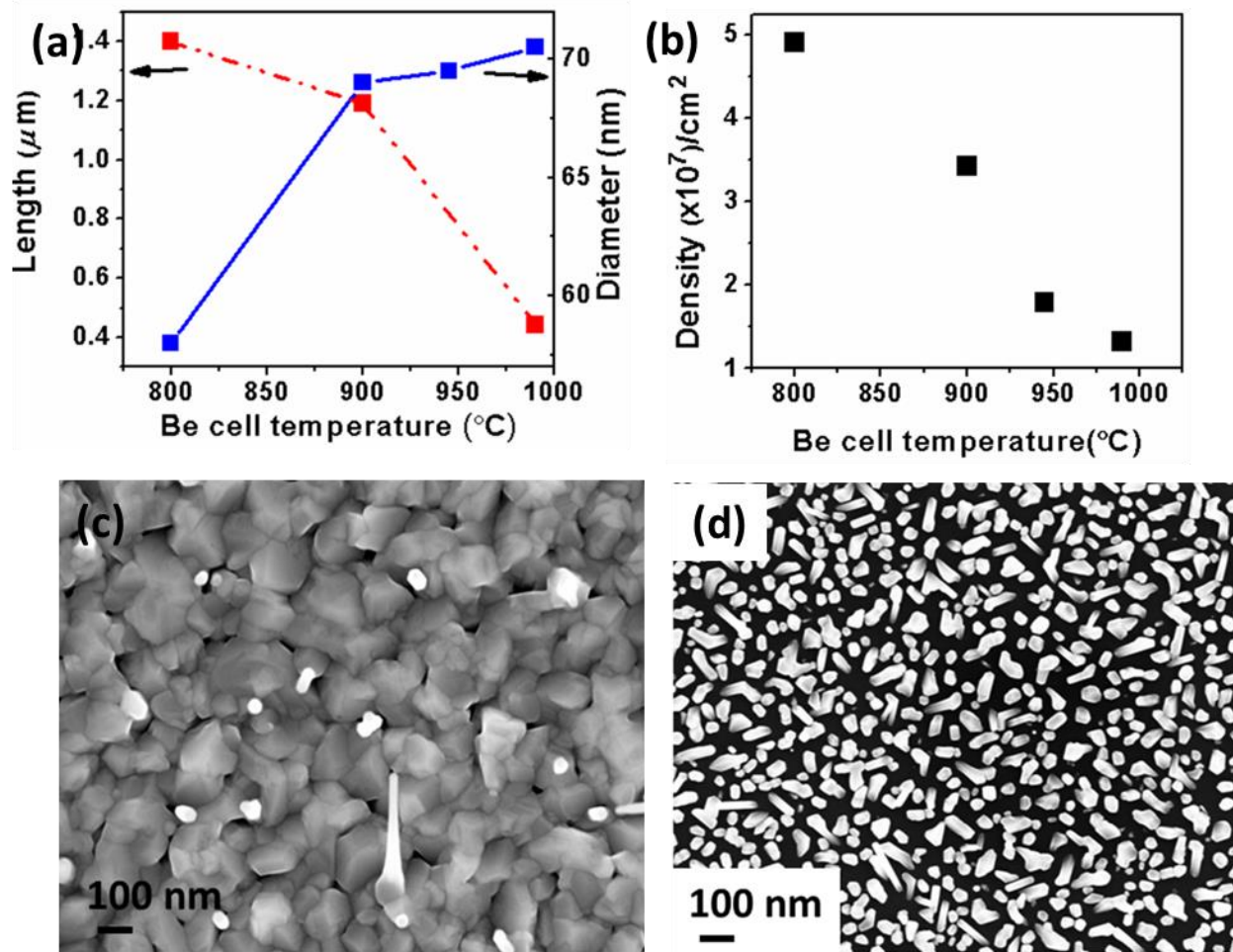
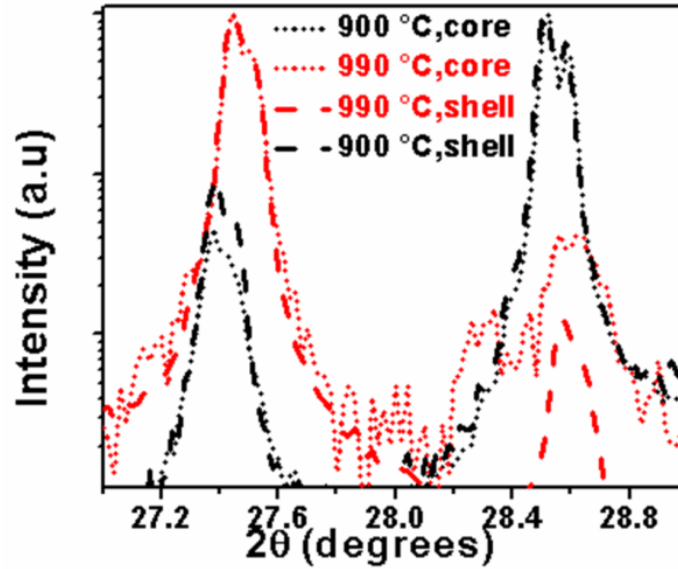


Figure 4.3. Variation of (a) length and diameter and (b) density of the nanowires with Be cell temperature. Be doped GaAs NWs with increasing Be cell temperature from (c) 800°C to (d) 990°C.

**4.3.2 X ray diffraction and STEM.** The  $2\theta/\theta$  XRD scans on all samples exhibited two dominant peaks corresponding to (111) reflections of GaAs and Si at  $27.4^\circ$  and  $28.5^\circ$ , respectively. The shoulder observed on the higher Bragg angle side near all peaks reflects the presence of both components,  $K\alpha_1$  and  $K\alpha_2$ , in the unfiltered X-ray source. This was later

confirmed by calculation. As XRD has only been used to assess the relative quality of the NWs and no quantitative data is derived, the unfiltered X-ray source does not impact any conclusion drawn.



*Figure 4.4.* XRD scans of core and shell structured NWs for Be cell temperatures of 900° C and 990°C.

Figure 4.4 illustrates XRD scans of the core and shell structures for Be cell temperatures of 900° C and 990°C. There was broadening of the peak with a shift towards higher angle as the Be temperature was increased whether we use a core or a shell. This broadening could be either due to the Be incorporation in the NWs or due to the poor crystalline quality of the sample surface. The peak intensity of GaAs (111) and Si (111) XRD peaks in the samples follow an inverse relation, i.e., high GaAs (111) peak is accompanied by small Si (111) XRD peak. It is very likely that Si (111) peak originates from the Si substrate itself. This is also confirmed with a significant reduction in the Si peak for both core and shell structure when more islanding of the 2D layer was present.

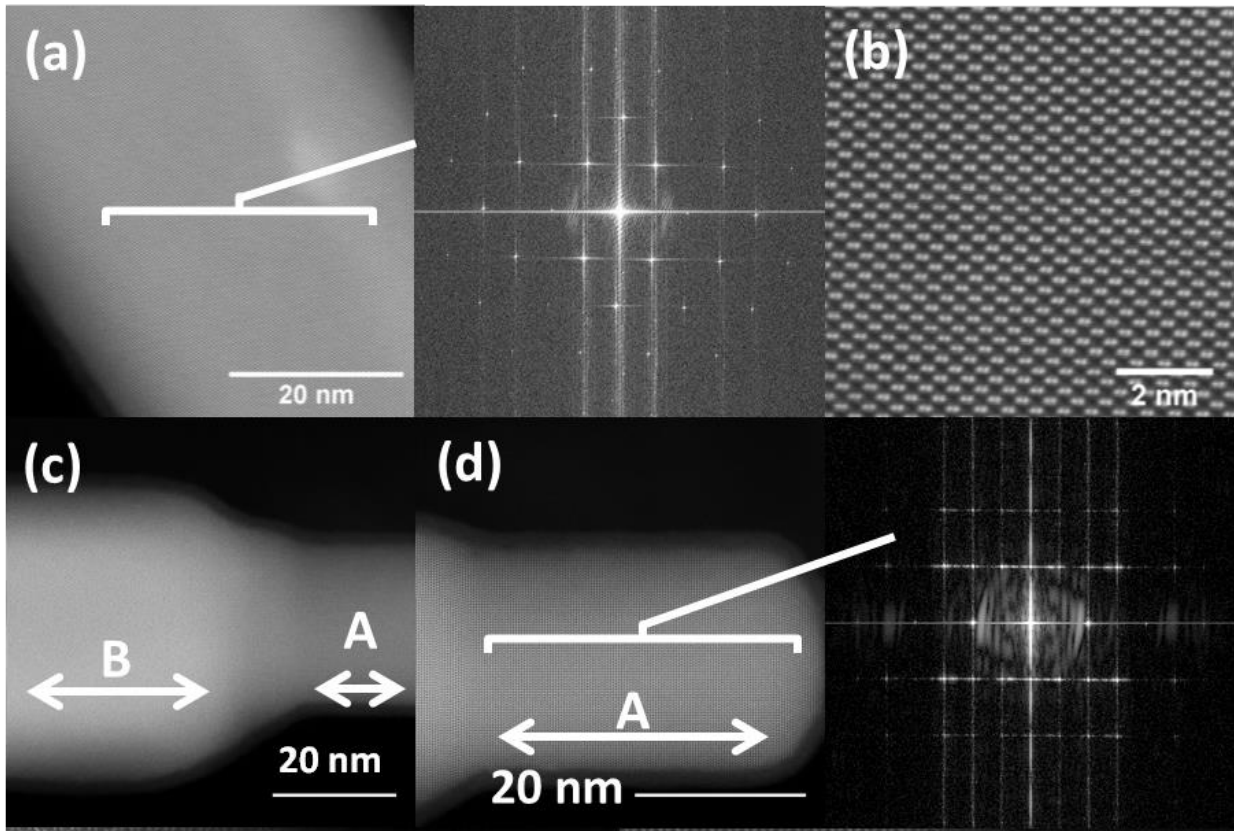


*Figure 4.5* HAADF and STEM images which (a) and (b) displays the zinc blende GaAs with GaAs dumbbells clearly visible as viewed from the  $[011]$  zone axis (c) Image showing necking down near the NW tip (d) FFT of WZ region in the NW tip viewed along the  $[2\bar{1}\bar{1}0]$  zone axis with WZ growth direction as  $\langle 0001 \rangle$ .

Figure 4.5 and 4.6 shows the HAADF STEM images emphasizing the transition from ZB to WZ phase. At the very tip of the NWs, for both the samples, the WZ structure transitions terminates in a ZB structure, as shown in Figures 4.7(a) and 4.7(e). The STEM image was acquired along the  $01\bar{1}0 \parallel 211$  (WZ $\parallel$ ZB) zone axis, where STEM images of the WZ $\parallel$ ZB structures are barely indistinguishable. Since the images for this STEM zone axis viewing are not included, we do not need to discuss. Only the STEM images acquired along the  $[2\bar{1}\bar{1}0] \parallel [011]$

(WZ||ZB) zone axes are included and shown, where the WZ-ZB interface is easily distinguished. The reduced diameter region associated with a necking phenomenon occurring near the tip of the core NW sample grown with Be at 900°C exhibits predominantly a WZ structure. The necking of the NW observed only in the doped NW cores can be attributed to termination of the Be flux while the As flux remains “on”. In the absence of Be, supersaturation is increased and with the availability of As flux, the wire continues to grow with smaller diameter, which strongly favors the WZ structure[59].

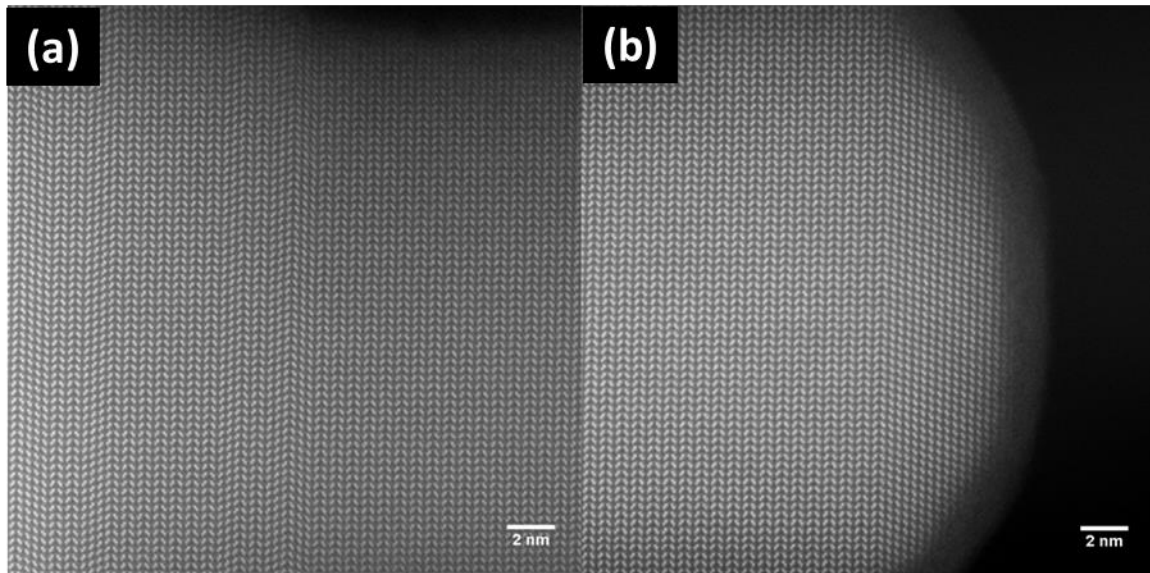


*Figure 4.6.* (a) Shows a transition from ZB to WZ with random twinning present (b) The tip end of the GaAs structure is shown transitioning back to ZB.

STEM micrographs (Figure 4.7) of core NWs grown at different Be cell temperatures of 800 °C and 900 °C exhibit a combination of both WZ and ZB crystal structures.

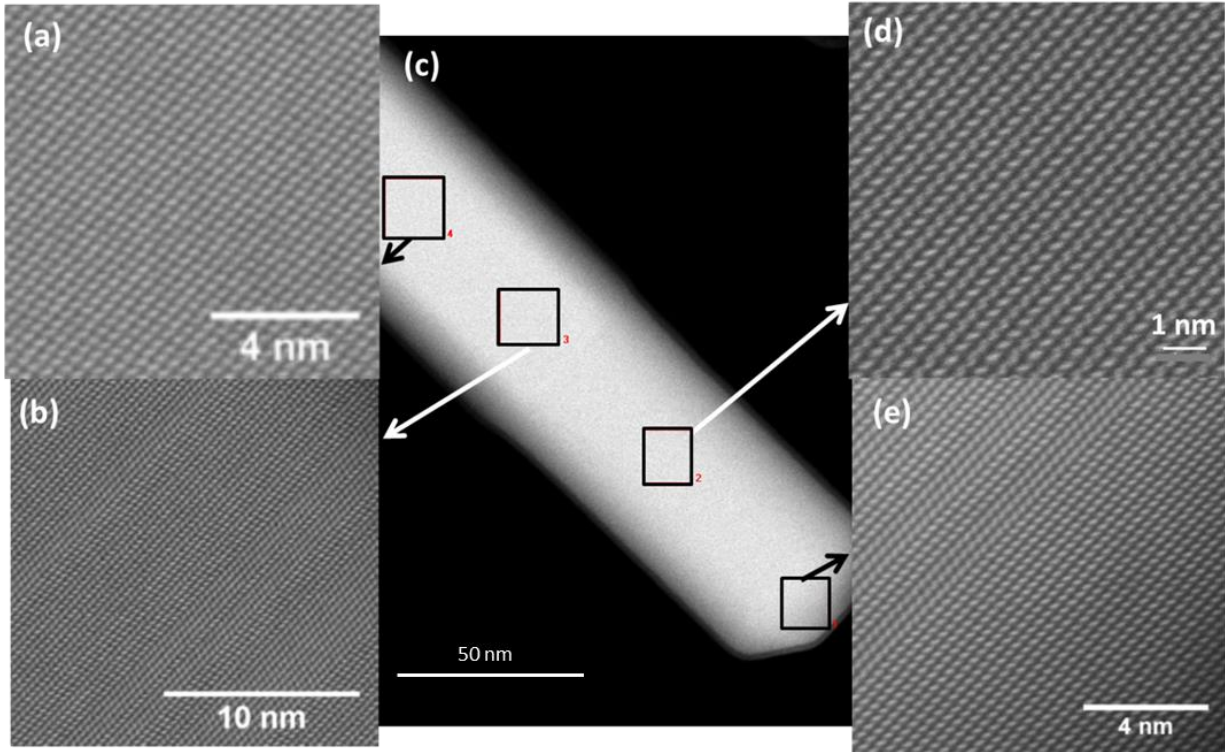


*Figure 4.7.* (a) HAADF STEM image of core NW, viewed along the  $[011]$  ZB zone axis indicating a predominantly ZB region. (b) viewed along the  $[2\bar{1}\bar{1}0] \parallel [011]$  (WZ||ZB) zone axes indicating a transition region from twinning ZB to polytype WZ congruent with NW diameter reduction (c) HAADF STEM image with selected areas annotated for region identification and correlation of subsequent images viewed from different axes, (d) viewed along the  $[2\bar{1}\bar{1}0]$  WZ zone axis indicating predominantly polytype wurtzite crystal structure (e) viewed along  $[2\bar{1}\bar{1}0] \parallel [011]$  (WZ||ZB) zone axes at the NW tip terminating in a ZB structure.

**4.3.3 Optical study of the Be doped NWs.** In this section, photoluminescence spectra was performed on all the samples including the core and shell structure and with Be at different cell temperature. Raman analysis was also performed to determine the vibrational properties and microstructural quality of the NWs.

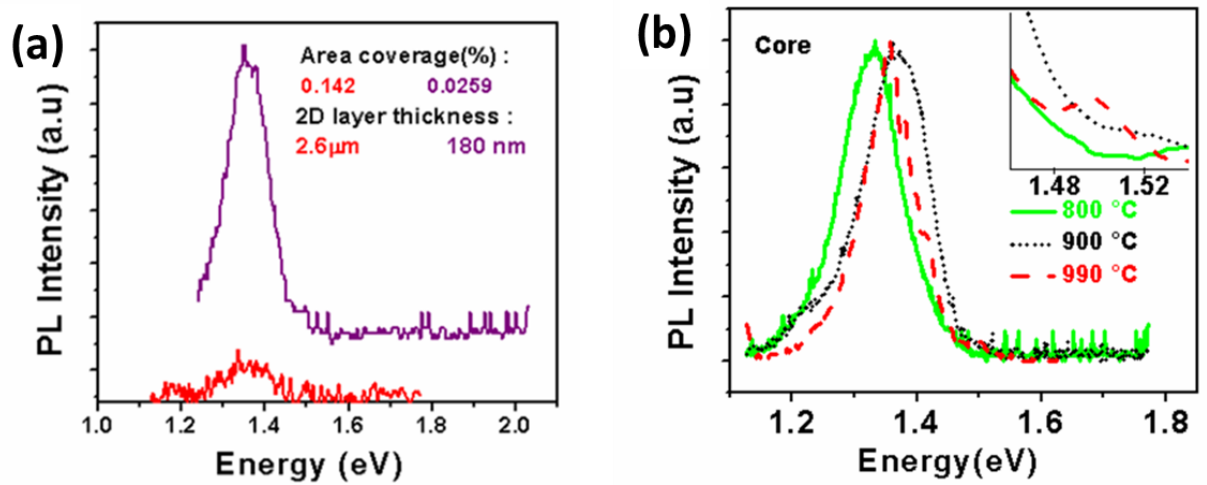


Figure 4.8. (a) PL spectra of samples with variation in density and 2D layer thickness for NWs grown at Be cell temperature of 900 °C. (b) PL spectra of NWs at different Be cell temperature.

**4.3.3.1 Photoluminescence study.** Figure 4.8(a) shows the PL spectra of NW samples before and after ultrasonication. It was found that the PL peak originated predominantly from the NWs as the peak intensity reduced drastically when the NWs were removed after ultrasonication. Figure 4.8(b) represents PL spectra of core NWs grown at different Be cell temperatures. A dominant and broad peak was observed in the range of 1.35-1.39 eV. This PL peak is associated with deep impurities and defects commonly attributed to the presence of two complexes,  $\text{As}_{\text{Ga}} - \text{Si}_{\text{Ga}}$  and  $\text{Si}_{\text{As}} - \text{V}_{\text{As}}$ , caused by diffusion of Si atoms from the Si substrate [100]. The PL peak shifted to higher energy with an increase in Be cell temperature from 800 °C to 900 °C and no significant shift was observed with a further increase in Be cell temperature. Hence, extensive characterization was carried out on the NWs grown with a Be cell temp of 900 °C and for the highest Be cell temperature of 990 °C, which exhibited a more narrow PL signal. A small peak was also observed at ~1.5 eV in all the samples except the one grown at 800 °C Be cell temperature; this peak becomes more well defined for NWs grown at a Be cell temperature of

990 °C. The PL shape of the NWs grown at 800 °C exhibited a long tail on the high energy side of the emission peak in contrast to that on all other samples, which showed a tail on the low energy side.

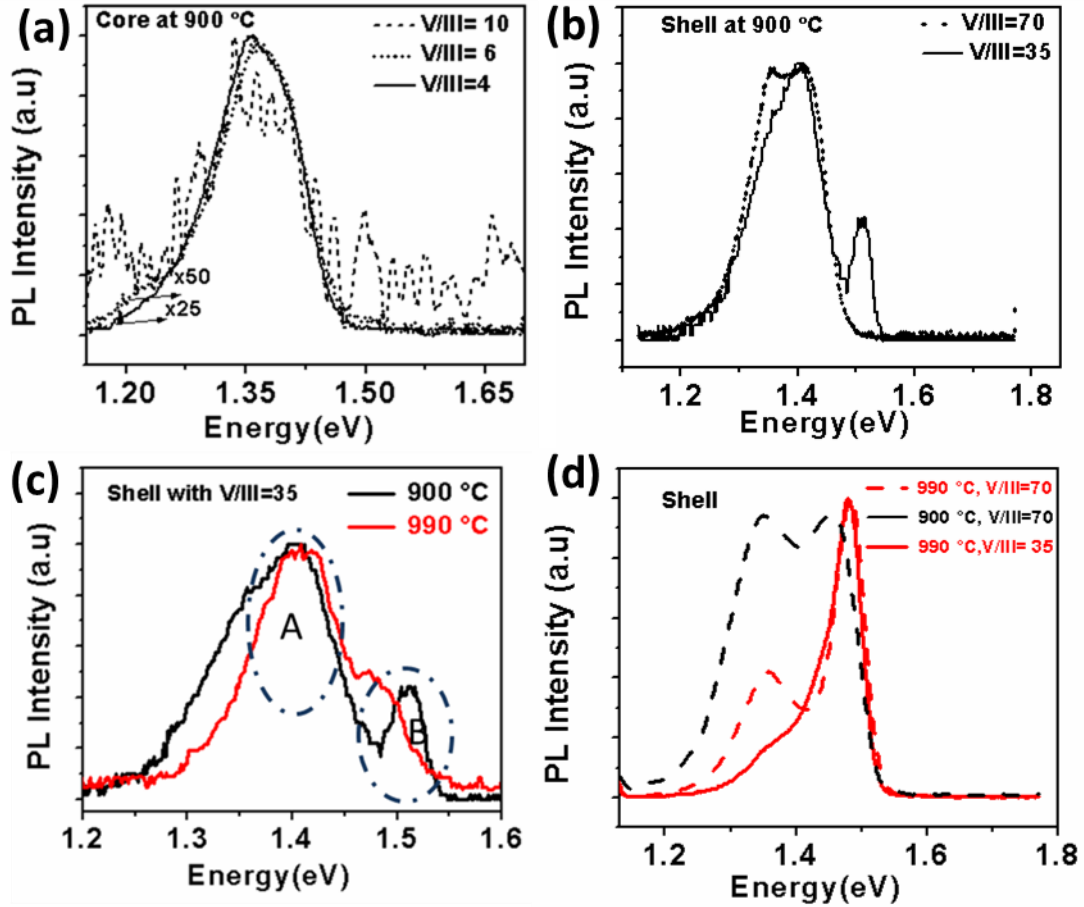


Figure 4.9. PL spectra of NWs grown at different V/III ratios of (a) core and (b) core/shell configurations. (c) PL spectra of core/shell (6/35) NWs for different Be cell temperatures and (d) comparison of core/shell structure for NWs grown at Be cell temperatures of 900°C and 990°C and at V/III ratios of 70 and 35.

Figure 4.9(a) shows the normalized PL spectral dependence of the NWs on V/III ratio. A higher V/III ratio of 10 results in a reduction in PL signal; hence, a ratio of 6 was found to be optimum with NWs having good density and PL signal. In the case of core/shell NW structures,

a blue shift in PL peak energy is observed with decreasing V/III ratio and no PL peak was discernible for a shell V/III ratio of 20 (not shown). Thus with the V/III ratio for the core at 6 as the optimized flux ratio, further tuning of the growth parameters were carried out at two Be cell temperatures of 900 °C and 990 °C as shown in Figure 4.9(c) and the V/III ratio of the shell as shown in Figure 4.9(d) . The growth duration for these samples were longer for both the core and shell, resulting in NWs of larger diameter of 388 nm and length of ~ 10 µm, to enhance the PL intensity. The PL spectra exhibit two broad peaks in the range of 1.35 to 1.39 eV and 1.48 to 1.51 eV assigned here as A and B, respectively, with the latter being dominant.

Be doped core nanowires with a varying V/III ratio from 10, 6 and 4 showed a consistent behavior in the reduction of the peak at the same Be cell temperature, i.e., 900°C. Keeping the As flux constant for a B.E.P at  $2.4 \times 10^{-6}$  Torr, the Ga flux was varied. The diameter was observed to reduce as the V/III ratio was increased. As the Ga flux is reduced, more As adatoms go to the liquid droplet increasing its supersaturation. But due to the less availability of Ga, the droplet size generally reduces which in turn reduces the diameter of the NWs. From the PL plot there is a higher intensity in case of the NWs with V/III ratio of 6 which could be due to alignment of the NWs.

Raman spectra of some selected samples are shown in Figure 4.10(a) and 4.10(b) which reveal three prominent peaks at  $267.7 \text{ cm}^{-1}$ ,  $290.7 \text{ cm}^{-1}$  and  $521.3 \text{ cm}^{-1}$ , corresponding to GaAs (TO), GaAs (LO) and Si (LO) peaks, respectively. Figure 4.10 (c) - 4.10 (e) display the variation of the full width half maxima of GaAs (LO) peak, GaAs LO peak intensity and TO/LO intensity ratio as a function of temperature. It may be observed that these three Raman peaks are strong functions of Be cell temperature and seem to be weakly dependent on the NW configuration. With increasing cell temperature the GaAs (LO) FWHM increases while the LO intensity

decreases with a corresponding increase in the TO/LO ratio. Amongst the 990 °C grown NW samples, the highest FWHM of the LO peak was exhibited by the shell configuration. The nanowire sample with Be cell temperature of 990 °C and V/III ratio of 6, exhibits an additional peak at  $391\text{ cm}^{-1}$  (Figure 4.10(a)) which is close to the  $384\text{ cm}^{-1}$  observed at 77K by Hilse et al.[38] on their Be-doped NWs grown by MBE and was assigned to  $\text{Be}_i\text{-Be}_{\text{Ga}}$  defect centers.

Applying the Raman selection rules to GaAs NWs, only the LO mode can be observed in a  $\langle 100 \rangle$  surface. Though the TO phonon is forbidden for this surface, the selection rules are relaxed due to the impurities that help in its activation[101]. With higher Be cell temperature of 990°C and lowering intensities of LO phonons indicates more Be incorporation in the NWs.

There is a strong dependence on the Be cell temperature on the structural and optical properties of the NWs. For the lowest Be cell temperature of 800°C, the NWs features are quite distinct as compared to those at higher Be temperatures. The GaAs XRD peaks obtained are very broad. The PL results show a blue shift for the higher energy peak which is also sharper as compared to other peaks (that is the tail at the lower energy path). In the Raman spectra too, there is an observation of highest GaAs LO peak accompanied with lowest TO/LO peak intensity ratio. Taking NWs with higher Be cell temperature of 990°C, the properties were contrasting. High x-ray Bragg intensity with a broader GaAs (111) XRD reflection is observed. There is a small peak near the band edge ( $\sim 1.49\text{ eV}$ ) in addition to a narrow defect peak A. A high GaAs TO/LO ratio is observed with a high FWHM ratio of these peaks. A peak at  $391\text{ cm}^{-1}$  is observed which can be taken as the interstitial Be peak which has been found in the bulk[38]. When the concentration of the Be is higher than  $1 \times 10^{19}/\text{cm}^3$ , there is a peak beyond 1.49 eV which is near the band edge known to be occurring in the Be doped bulk layer. The evolution of the higher energy peak B may thus be considered as a signature of Be incorporation, which is consistent

with reports in literature[100]. Thus, PL and Raman characteristics are indicative of enhanced Be incorporation in these NWs with increasing Be cell temperature. On the contrary at low Be cell temperatures, a low concentration of Be is reported [36] to pin the Fermi level at the surface due to dominance of surface defects. This in turn leads to a doping profile induced electric field quenching of low energy photons[102], which is consistent with the distinct PL behavior of this sample.

As shown in Figure 4.9 (b) and (c), the peak B (1.48 eV to 1.51 eV) has been found to be more pronounced. The ratio of the peak intensity of B to A was observed to increase with decrease in V/III ratio, increase in Be cell temperature and longer growth duration. A V/III ratio of 35 was found to be the optimum below which the PL signal vanishes (fig. 4.9(c)). The Raman peak intensity ratio 12 of TO/LO increases with an accompanying reduction in the individual peak intensity and broadening of the peaks for the shell configured NWs in comparison to the core. The Si peak at  $521\text{ cm}^{-1}$  is also reduced. Also, amongst the shell configuration all the above discussed Raman features are more accentuated with an increase in the cell temperature and for the V/III ratio of 35.

The effect of various growth parameters becomes clearly evident when the shell is grown thicker for a longer time (Figure 4.9(e)). For a lower Be cell temperature of  $900\text{ }^{\circ}\text{C}$ , the peak A and peak B intensity are comparable with the peak B at 1.45 eV for V/III ratio of the shell at 70.

The variation of different Raman parameters deduced from the Raman spectra (Figure 4.10 (a) - 4.10 (e)) namely, broadening of the Raman GaAs LO FWHM accompanied with the increase in corresponding TO/LO peak ratio, decrease in LO peak intensity and a Raman Si peak with increase in cell temperature and with a change in core to shell configuration are consistent with the enhanced Be incorporation.

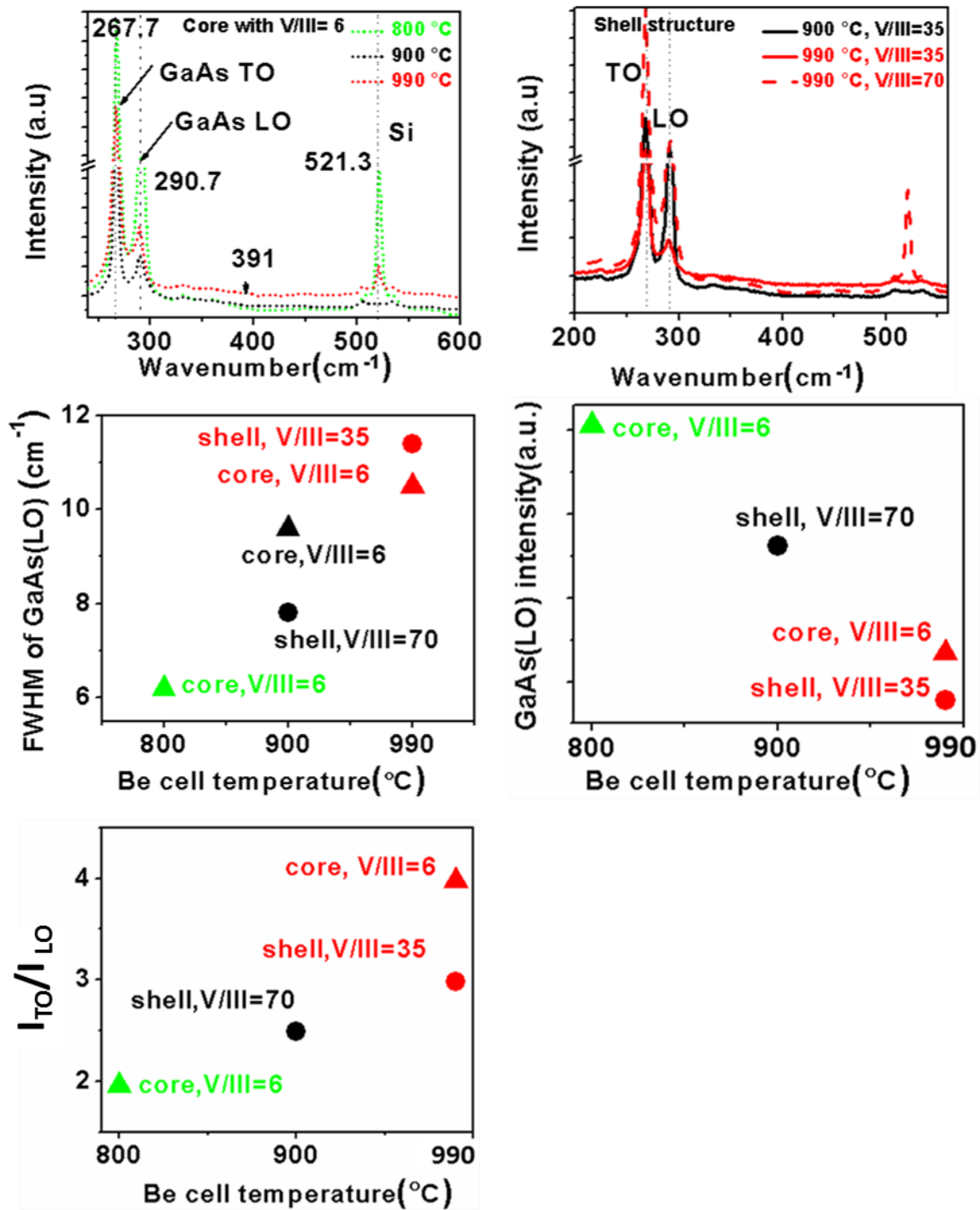
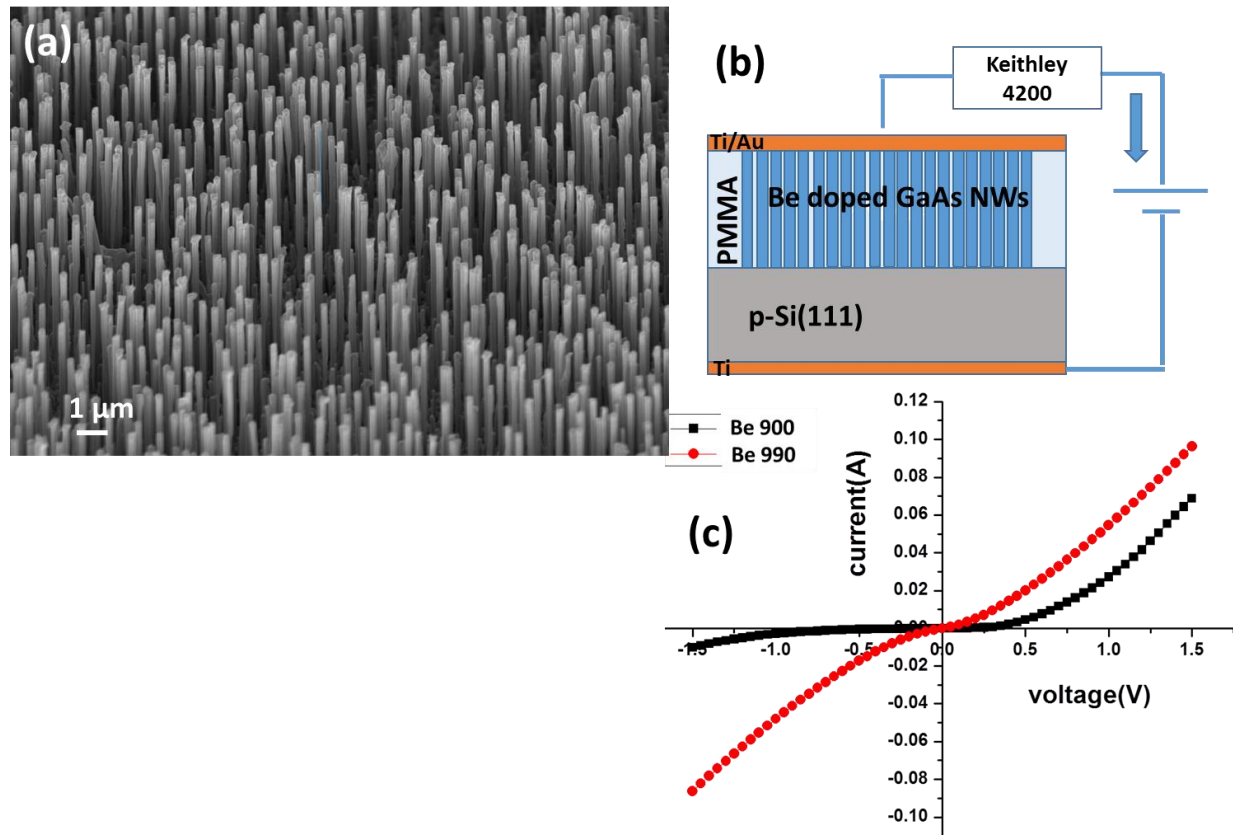


Figure 4.10. Raman plots of the (a) NW core and (b) with the core/shell configuration grown at Be cell temperature of 990 °C. Variation of (c) FWHM (LO) modes of GaAs and its (d) their intensities (LO) and (e)  $I_{TO}/I_{LO}$  for the GaAs peaks as a function of Be cell temperature.

All these observations suggest that Be preferentially incorporates through side facets as opposed to soluble Be within the Ga melt, which is in excellent agreement with the conclusions by Casadei et al. [36] on their Be-doped shell configured single NW based on electrical conductivity measurements. Further, the extended growth period resulting from the temperature ramping and shell growth also likely contribute to the continued diffusion of Be within the volume of the core [94]. It has been reported that Be atoms diffuse predominantly via a kick-out diffusion mechanism [103] in which a lower As/Ga ratio promotes diffusion [104, 105]. Further variation in the As/Ga ratio from 70 to 35 was found to increase the radial growth rate by three times. These observations provide insight on the As/Ga ratio dependence of the shell configuration on our PL and Raman data. Although carrier concentrations were not measured on the NWs, I-V characteristics were performed to illustrate the dopant incorporation.

**4.3.4 Growth of Be doped on etched substrates.** Be doped NWs were also grown on Si (111) substrates which were etched and subsequently oxidized in air at room temperature, prior to the growth. The V/III BEP flux ratio for GaAs core and shell were 6 and 35, respectively. The substrate preparation was found to be crucial in order to enhance the NW density and is discussed in detail in Chapter 7. Figure 4.11(a) below shows a typical SEM images of Be doped GaAs NWs grown on a chemically etched and dry oxidized p-type Si (111) substrate. All the NWs were vertical to the substrate with a diameter of  $165 \pm 20 \text{ nm}$  and height of  $3 \mu\text{m}$ . I-V characteristics was examined for two core shell samples which were grown with Be cell temperatures of  $900^\circ\text{C}$  (Be 900) and  $990^\circ\text{C}$  (Be 990). The samples for I-V measurements were prepared as follows. A Poly methyl methacrylate (PMMA) layer was used to fill the gaps between the NWs. PMMA thickness was measured to be  $\sim 4500 \text{ \AA}$  using an ellipsometer. Thereafter the NW was planarized by sonicating with DI water for 2 hours in a sonication water

bath. The NWs were then rapid thermal annealed under ambient atmosphere at 400°C for 40sec duration to expose the NWs for contact. Ti ( 50 nm)/Au( 200 nm) and Ti (200nm) were used for the top contact on the NW and back contact on the p-type Si, respectively[106]. Figure 4.11(b) shows the schematic of the 2 probe I-V measurement setup. The electrical measurements were performed in air at room temperature using a Keithley 4200 characterization system using a 2 probe method.



*Figure 4.11.* (a) shows the SEM image of Be doped NWs, (b) shows the schematic of I-V measurement for both the samples, (c) I-V curve for the ensemble of NWs at Be cell temperature of 900°C and 990°C.

Figure 4.11 (c) shows the I-V curves of an ensemble of Be doped GaAs NWs. For better comparison the electric current was measured at  $\pm 1.5$  V in both the samples. It was observed that the NWs with Be cell temperature at 990°C showed a much symmetric I-V curve with more linearity and higher current for a given voltage as compared to the ones grown at Be cell temperature of 900°C. The latter can be attributed to the high interfacial barrier caused by the pinning of the Fermi level in the NW at the surface states. The asymmetric behavior of the I-V characteristic is indicative of the different contact resistances present at the Si- NW and NW – metal contact, the latter being larger than the former. At higher Be cell temperature the higher doping on the semiconductor may likely causes unpinning of the Fermi level and forms an interface layer between the NW and the metal contact[107] lowering the barrier. This in turn enables enhanced tunneling of the charge carriers leading to more linear and symmetric I-V behavior, consistent with the observation of Dheeraj et al. [37] . These are clear evidences of higher Be incorporation.

**4.3.4.1 Photoluminescence measurement.** Figure 4.12 (a) below show the 4K PL measurement of both the samples. The main peak was at 1.5 eV. The peak at 1.5 eV was a clear indication of the Be doping in the NWs[108]. The FWHM were 33meV and 80 meV for Be 900 and Be 990, respectively. The broader FWHM can be considered as a signature of enhanced Be incorporation due to more disorder in the NW. The absence of any other peak is indicative of the good quality of the NWs.

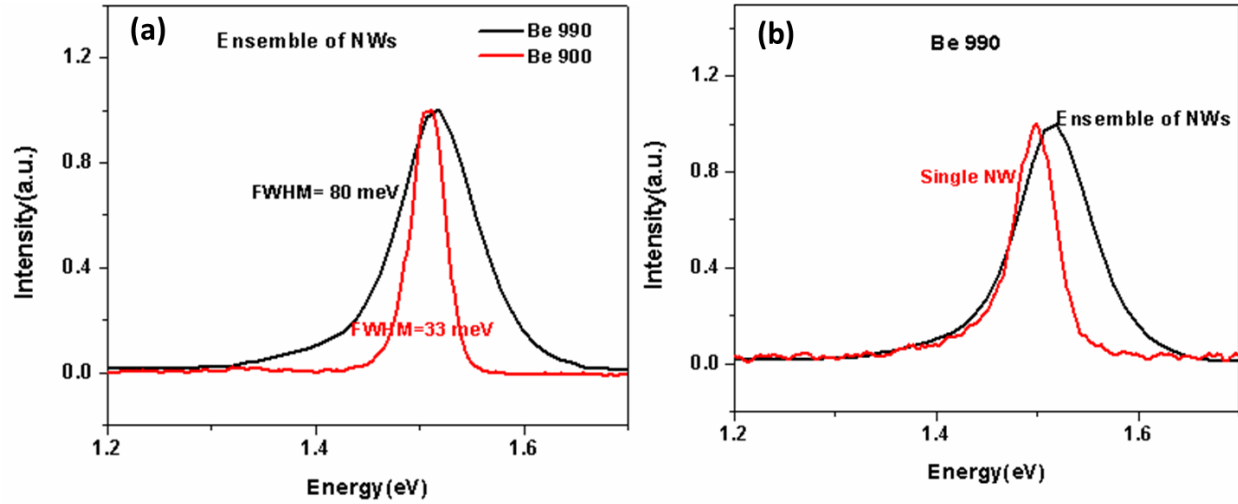


Figure 4.12. (a) 4K photoluminescence of samples grown with Be cell temperature of 900°C and 990°C (b) comparing single NW with the ensemble of NWs of sample grown with Be cell temperature of 990°C.

Figure 4.12(b) above shows the 4K  $\mu$ -PL measurement comparing single NW with the ensemble of NWs of Be 990. Single NWs were prepared by sonicating the ensemble of NWs on Si substrate in propanol for 30 minutes. Later the NWs are collected and transferred through a micropipette onto a Cu grid. It is allowed to dry in the grid which is followed by  $\mu$ -PL measurements. The peaks occur at 1.5 eV for Be 990 with FWHM of 53 meV. Comparison of single with the ensemble of wires showed a blue shift of 10 meV for the PL peak which broadened in case of ensemble of NWs. This could be due to variation of Be incorporation from single to ensemble ones. These results are in excellent agreement with our earlier results in section 4.3.3 and also the NW are homogenous and superior in quality as evidenced by the lack of the impurity related PL.

#### 4.4 Conclusion

In order for GaAs-based nanowires to be widely adopted in novel nanoelectronic and nanophotonic devices, one must understand the growth parameters that influence dopant

incorporation. As a consequence, we have performed a detailed and comprehensive investigation on the effect of V/III flux ratio, NW configuration and cell temperature on Be incorporation in MBE grown GaAs NWs. It has been demonstrated that Be incorporation is strongly influenced by NW configuration, Be cell temperature and V/III ratio of the shell. We find that a shell configuration with Be cell temperature of 990 °C with a V/III ratio of 35 for the shell are optimum for high Be incorporation. Using appropriate preparation of the substrate, high density and good quality doped NWs have been achieved as attested by PL data. Single NW PL replicates very well the PL ensemble, The I-V measurements were consistent with higher Be incorporation for Be cell temperature of 990°C.

## CHAPTER 5

### GaAs/GaAsSb Axial NWs on Non-etched Epiready Si Substrate<sup>1</sup>

#### 5.1 Introduction

The GaAsSb NW by itself [15] had been grown on GaAs(111)B substrate, exhibiting rotational twins around its (111)B growth axis, with an equal amount of twinned and untwined orientations. Plissard et al. [30], had demonstrated the growth of GaAs/GaAsSb without Au as a catalyst instead using the Ga to induce the growth. The Sb composition used in the GaAsSb core was up to 30 at. %. Unlike other III-V's, GaAsSb requires more accurate control in the composition due to the presence of two competing group V species with different sticking coefficients.

In this chapter, the self-catalyzed Ga assisted growth of GaAs NWs with GaAsSb inserts on Si (111) substrates has been studied. Structural and optical properties as a function of the number of segments in the nanowires are presented using a variety of characterization techniques. Extensive photoluminescence study on the NWs was performed which included 4K temperature dependence analysis.

#### 5.2 MBE Growth

The NWs studied were grown by MBE exploiting the vapor-liquid-solid mechanism initially reported by Wagner and Ellis [47] in 1964 where Ga was used as catalyst on a Si (111) substrate.

**5.2.1 Ga assisted GaAs/GaAsSb NWs on Si (111).** As previously reported, Au is the most commonly used catalyst. Successful MBE growths of Au assisted NW growths has been demonstrated [15]. But due to the deep trap formation along with its high diffusivity of the Au

---

<sup>1</sup> Parts of this chapter were adapted from book chapter: Iyer, S., et al., *A Study of Ga-Assisted Growth of GaAs/GaAsSb Axial Nanowires by Molecular Beam Epitaxy*. Nanoscience and Nanoengineering: Advances and Applications, CRC Press, 2014: p. 31.

into the semiconductor, it leads to contamination of the NWs. Due to these reasons alternative catalysts were proposed. In this study Ga is used as a self-catalyst.

1x1 cm square pieces of Si (111) epitaxial substrates were used for the growth. The substrate was rotated at 30 rpm and the growth temperature was varied from 580°C to 620°C. These growths were initiated by impinging Ga vapor to condense into isolated droplets on the Si substrates for 6-8 sec before allowing the As flux. The As to Ga ratio was kept constant at 6 for all the samples at an As BEP of  $2.4 \times 10^{-6}$  Torr. The NWs features were characterized using the in situ RHEED diffraction pattern. Below (Figure.5.1) are the typical RHEED images obtained during the growth which shows the evolution of the RHEED patterns during the NW growth. Due to instrumental shortcoming, further analyses on RHEED were not performed.

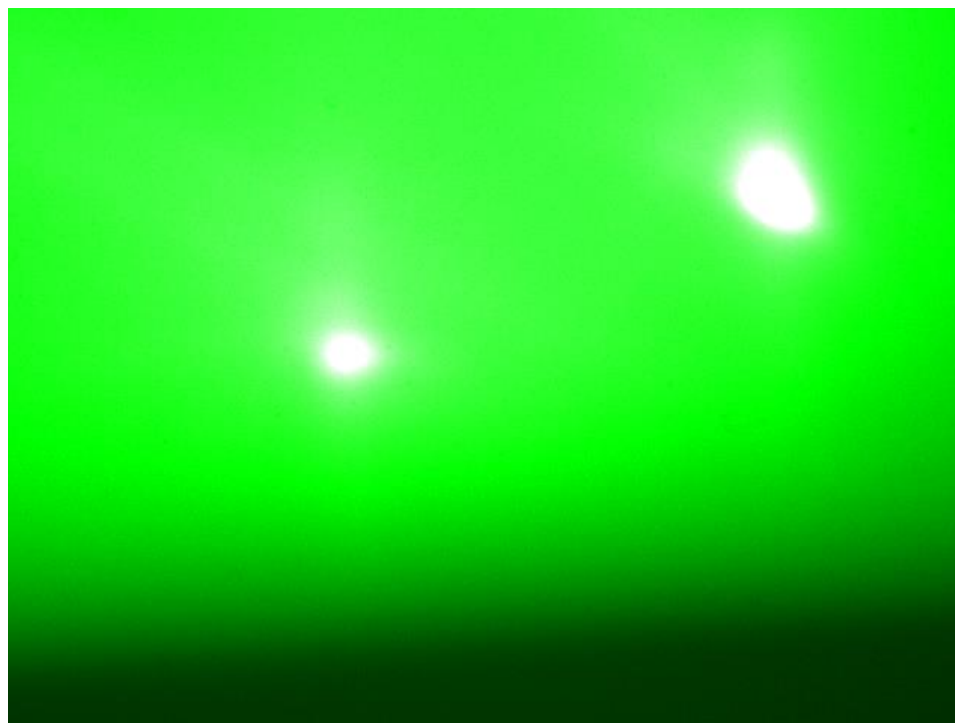


*Figure 5.1.* RHEED patterns of a Si substrate in the initial GaAs NWs growth showing the 3D islands formation.

As soon as the growth starts, the Ga droplets deposits on the substrate forming the 3D islands. As the growth proceeds, there is a shift in the RHEED pattern to horizontal isolated oval shapes confirming the 3D islands which are generally NWs [87]. A detailed analysis of these patterns could give information on the defects or presence of twin planes, whether it is WZ or ZB and also the reciprocal lattice spacing of materials.

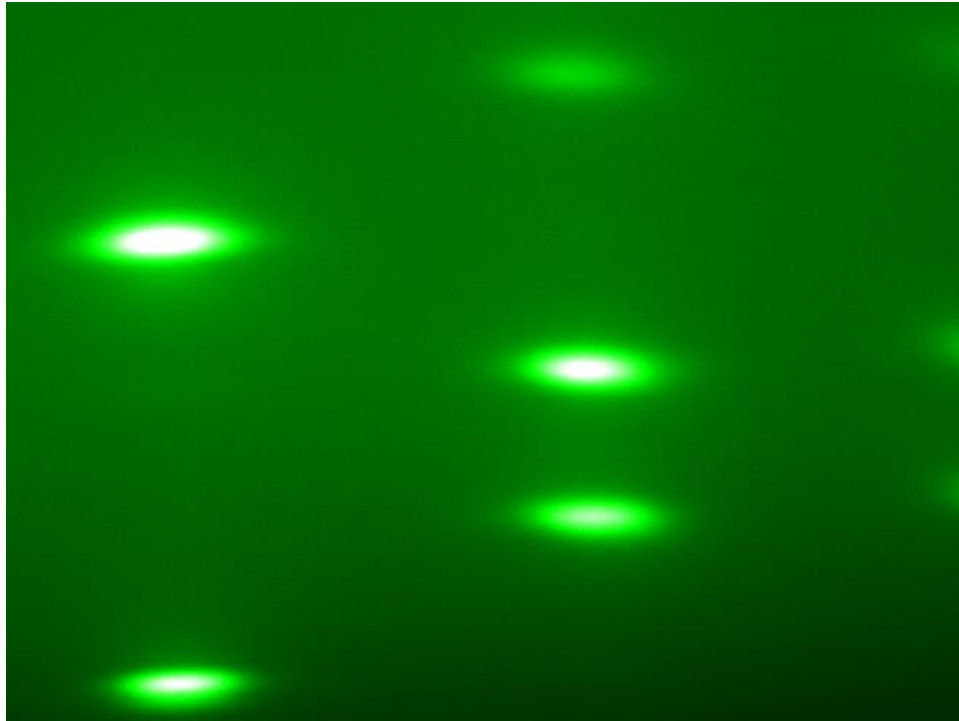


*Figure 5.2.* Typical RHEED image during a GaAs/GaAsSb NW growth on an epitaxial Si (111).

### **5.3 Scanning Electron Microscopy Analysis.**

Figure 5.3 below shows the schematic of NWs with two different configurations proposed. Figure 5.3(a) shows a single segmented GaAs/GaAsSb NW N1 and (b) shows a double segmented one N2. Based on the growth temperature, the nomenclature gets modified with an added growth temperature value. Along with the configurations, it also depicts the opening and closing time of the Ga, As and Sb shutters.

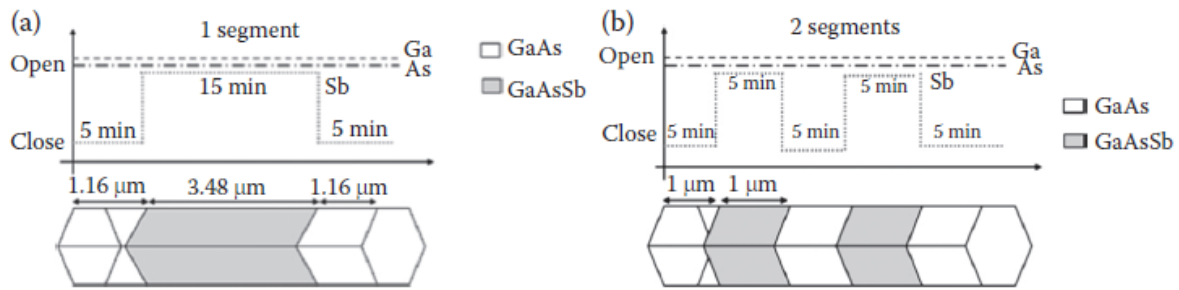


Figure 5.3. (a) schematic of the one segment NWs (b) two segmented NWs grown along with their expected dimensions. We also see the opening and closing time of Sb valve.

Below Figure 5.4(a) displays the SEM image of a single segmented GaAsSb in a GaAs NW, namely N1 620, with well uniform surface and a flat top where the Ga droplet was removed with an excess As flux. A typical alignment of the NWs with almost 80%, were vertical to the substrate as shown in the Figure 5.4(b). The length of these NWs was controlled by the Ga and As flux. They had a diameter of 150-180 nm and  $\sim 4$ -5.5  $\mu\text{m}$  length. The densities of these wires were less, ranging approximately from  $4 \times 10^6$  to  $3 \times 10^7 \text{ cm}^{-2}$ .

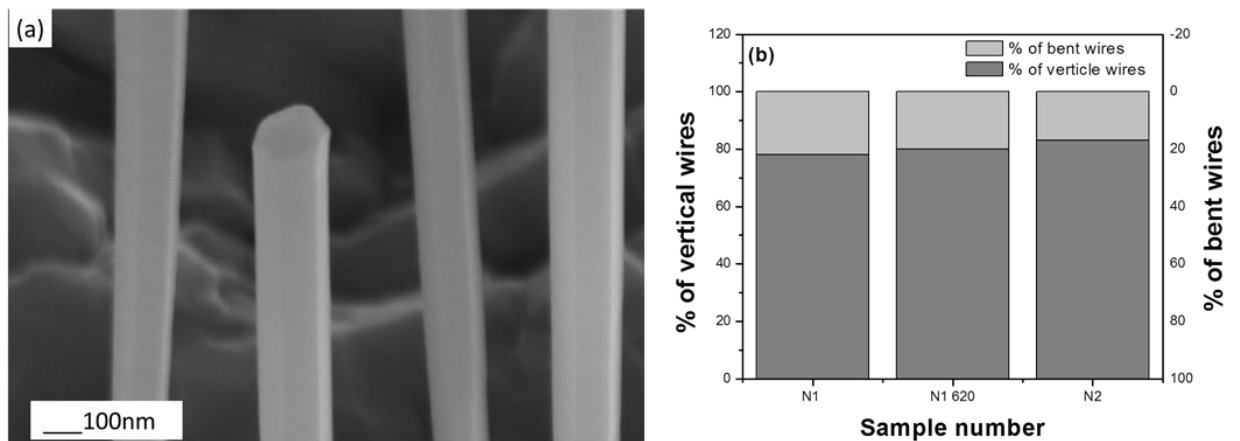


Figure 5.4. Hexagonal-shaped GaAs NWs grown on Si substrate and (b) comparison of the percentage of vertical and bent wires in different samples taken over an area of  $200 \mu\text{m}^2$ .

The Ga droplet plays an important role in the structure of the NW. Not only does it play a major role in determining its diameter, but also affects the length of the NWs by acting as a catalyst. At the initial stage the Ga shutter was opened for 8 sec. This allowed enough Ga to react with the Si substrate and form nano-droplets at the substrate's surface. The size of these droplets determines the diameter of the nanowires. Based on the growth rate and the growth temperature, the NWs grow axially or radially. By the removal of this Ga droplet, the axial growth can be terminated. Simultaneous closing of the As and Ga shutters results in a Ga droplet on the top of the NW as shown in Figure 5.5(a). Leaving the As "on" after termination of the growth resulted in a tapered top as shown in Figure 5.5(b). Thus, the tip of the NW can be suitably controlled by the As flux caused by varying Ga consumption consistent with the VLS growth mechanism.

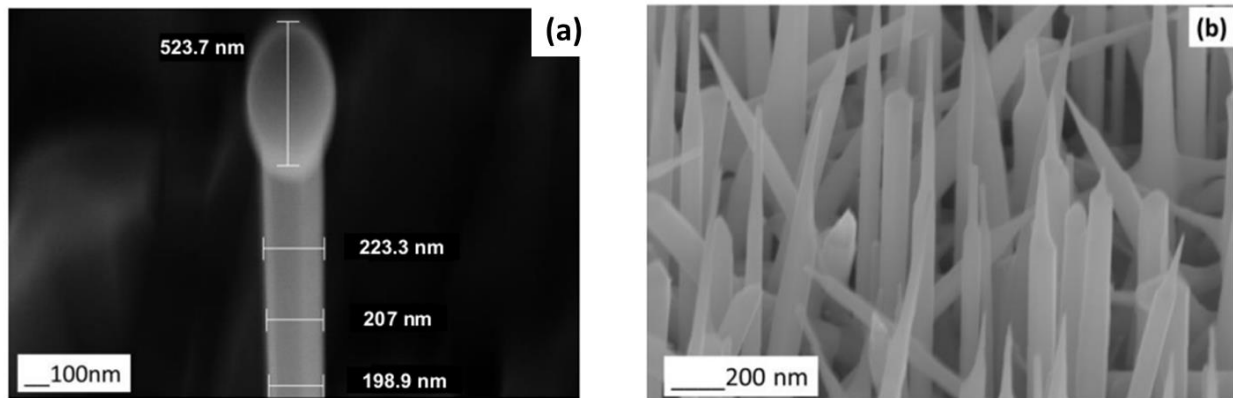
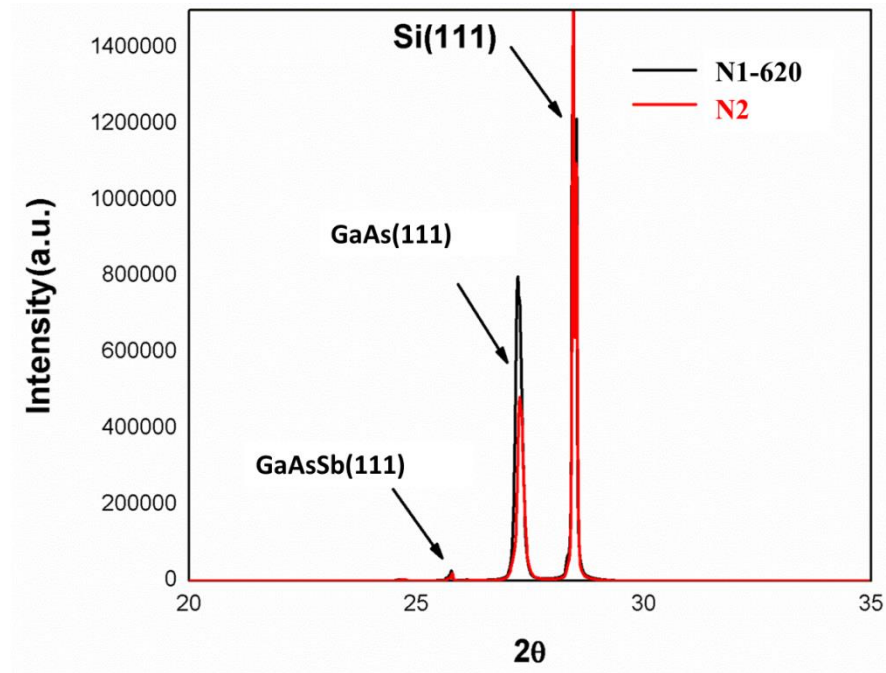


Figure 5.5. (a) Single segmented NW with Ga droplet on the top. (b) NW with tapered top

#### 5.4 XRD Analysis.

Since these NWs are grown on an epitaxial Si (111) substrate and the vertical alignment of the NWs is necessary for a good device, it is very important to determine its orientation with respect to the substrates. The  $2\theta$  scan of the XRD spectra was done in order to find the orientation and to determine the crystalline nature of the NWs. These scans were performed on GaAs NWs containing single GaAsSb insert (as shown in the Figure 5.6). The main dominant

peaks obtained were  $26.83^\circ$ ,  $27.31^\circ$  and  $28.44^\circ$  as shown in Figure 5.6 below. These correspond to GaAsSb (111), GaAs (111) and Si (111) substrates respectively. The scan showed the orientation of the NWs along (111) direction.



*Figure 5.6.* XRD scan of sample N1 620 and N2 are GaAs/GaAsSb NWs grown at  $600^\circ\text{C}$  and  $620^\circ\text{C}$ . Peaks at  $26.83^\circ$  represents to GaAsSb (111).

### 5.5 TEM Analysis.

Transmission electron microscopy (TEM) was performed on samples containing both N1 and N2 type of NWs. Figure 5.7 below shows the TEM image and SAED patterns of NWs N1 620 which contain a single GaAsSb segment as depicted in Figure 5.3. This NW contained a pure ZB phase verified by SAED patterns and also contained randomly spaced stacking faults as multiple twins. They are located at the upper-third to top quarter of the NW in the form of lamellar parallel to the (111) twin composition plane. This twin region correspond to the cessation of Sb incorporation in the NW. SAED pattern confirms the ZB NW to be (111) oriented and the twin planes to be (111) directed.

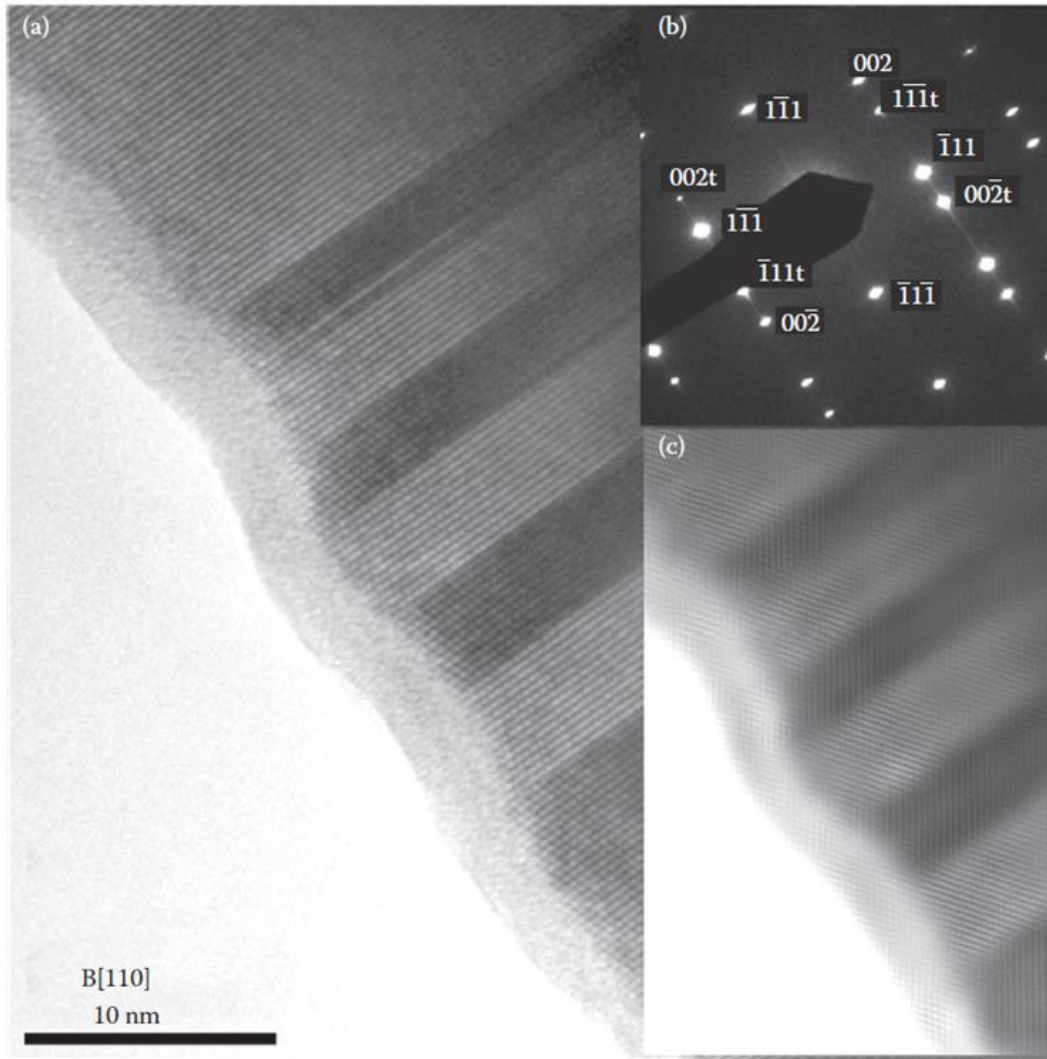


*Figure 5.7.* Shows (a) the TEM image of a NW with twin planes and (b) the corresponding SAED pattern of the twin (111) plane. Inverse Fast Fourier filter of HRTEM image (c) applied to the (002) reflections of both ZB twin phases illustrates the mirroring of the (002) and (002t) planes across the twin boundary.

For these GaAs/GaAsSb NWs, the formations of twin boundaries have separated the crystal domains by rotating in a symmetric manner. GaAs ZB crystal structure is in the  $F\bar{4}3m$  space group. And the  $[111]$  symmetric zone axis belonging to the  $F\bar{4}3m$  plane is parallel to the

NW growth axis. Subsequently the ZB phase mirrors one another across the twin boundaries with the ZB zone axes  $[1\bar{1}1]$  and  $[\bar{1}1\bar{1}]$  changing direction across the axes. For ZB GaAs, the symmetry operation for a rotation about the  $[111]$  axis is a triad. Thus, the twinning operation may be a  $60^\circ$ , a  $180^\circ$ , or a  $240^\circ$  rotation about the twin axis. However, it is conventional to describe the twinning operation as a rotation of  $180^\circ$ .

For N1 620 NWs, which exhibit Ga droplets at the tip, there was no evidence of a WZ phase at any point along the NW. However, for the N1 and N2 NWs in which the tip were devoid of Ga droplets, a region of WZ phase would occur just below the tip.

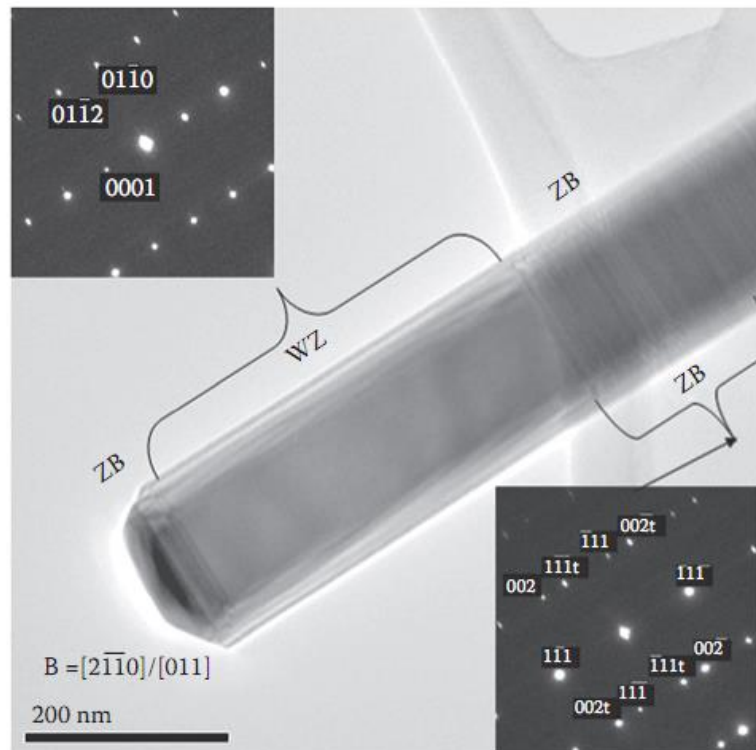


*Figure 5.8.* N2 NW without a Ga droplet at the tip and with a 400 nm region with a WZ structure just below the tip. The very tip end and the remaining NW below the WZ region are pure ZB with multiple twinning.

Sb plays a major role in the structure formation of the NW and generally results in a ZB structure [10]. Sb being a heavier element (at. no. 51) has longer covalent bonds compared to Ga and As. It behaves as a surfactant and has strong influence on surface related properties. It can modify the surface free energy and have negligible solubility in the bulk. It accumulates on the surface and affects the growth kinetics[60]. It has much lower vapor pressure [ $2 \times 10^{-4}$  Torr at  $450^\circ\text{C}$ ][109]. It tends to remain on the surface of the binary systems such as GaAs, InSb and produce growth irregularities. With the introduction of Sb during the growth, it resulted in ZB GaAsSb inserts on already existing ZB GaAs stem structure [95]. To get a lower energy, the ZB nucleus at the TPI (triple phase interface) tend to rotate  $180^\circ$  which results in formation of twin surfaces and result in the planar defects. Although these defects are formed, the NW exhibits the ZB structure due to the GaAsSb insert.

**5.5.1 Composition analysis by XEDS.** Figure 5.9 below shows the XEDS line scan and also the STEM imaging over the entire NW range. The XEDS line scan below confirms the incorporation of Sb in the NW. In addition, Sb mole fraction in the GaAsSb inserts was found to vary from 1 to 4 at. %. The region 2 shows Sb content of 4 at. % . Though not expected, some traces of Sb are found in region 3. It was found that the growth rate of the GaAsSb was  $\sim 20\text{-}25\%$  larger with respect to anticipated one as shown in the Figure 5.3. An XEDS line scan shows the relative elemental X-ray count distribution along the NW axis. The collective X-ray count increases with NW diameter in the direction of the NW base.

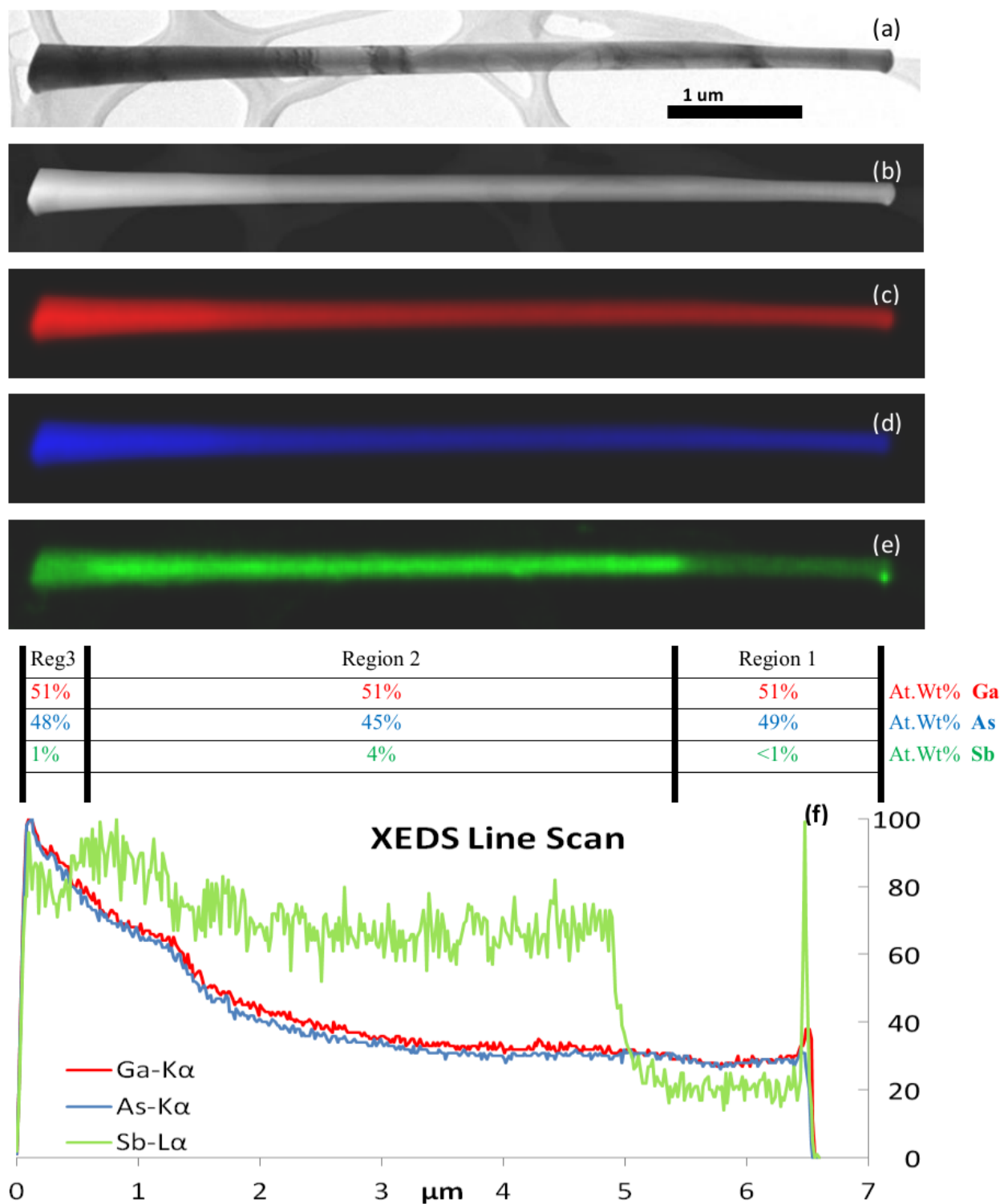


Figure 5.9. (a) A NW with a single GaAsSb band (Region 2 (e)) imaged with TEM, (b) HAADF-STEM and (c) through (e) XEDS-STEM mapping of Ga, As and Sb, respectively. (f)

## 5.6 Photoluminescence

Photoluminescence is a powerful tool to investigate the optical properties of the NWs, which are greatly influenced by the surface and morphological effects due to the inherent large surface-to-volume ratio. For instance, the WZ–ZB interface in GaAs is reported to yield PL peak energies lower than the corresponding polytypes due to the two phases at the interface forming a type II band alignment[110]. Similarly, the presence of defect levels often leads to luminescence at energies below that of the band gap at low temperatures. Thus, a clear interpretation of luminescence spectra of these NWs requires more detailed investigations. The temperature dependence of photoluminescence determines the nature of defects and non-radiative recombination centers and hence is indicative of the lifetime of the carriers.

In this work, we have carried out a detailed study of the temperature dependence of the PL spectra for the three NWs. Figure 5.10 (a) displays the low temperature PL of all the three NWs. The N2 sample exhibits the highest PL peak intensity with the spectra having a slightly asymmetric line shape with a relatively sharp high-energy cutoff.

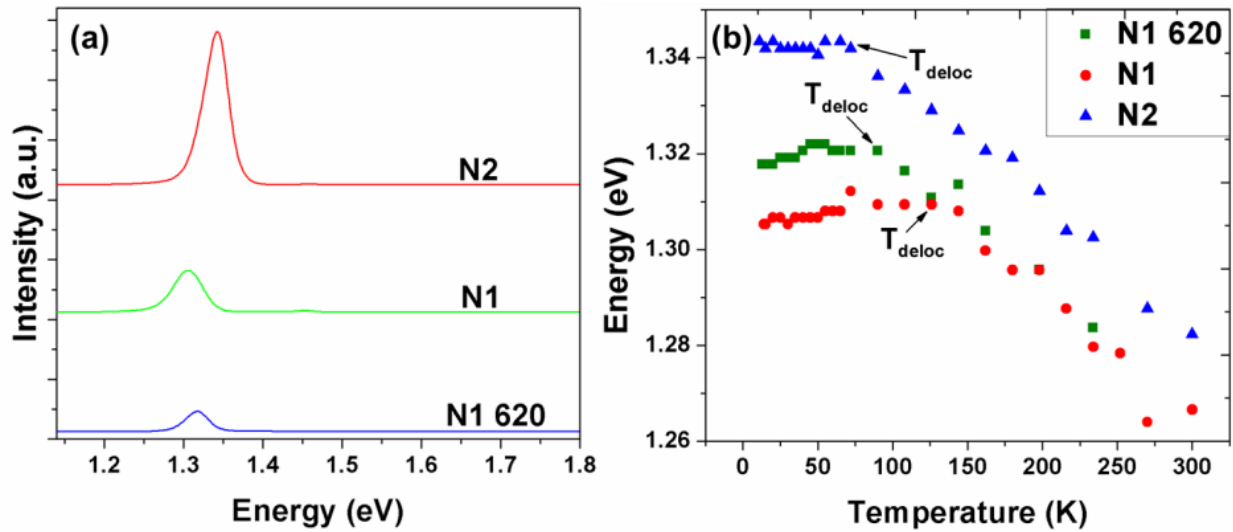


Figure 5.10. (a) 11 K PL spectra of the NWs and (b) temperature dependence of PL peak energy.

In Figure 5.10 (b), the temperature dependence of the PL peak energy is displayed for all the samples. In the low-temperature regime, single-segment wires exhibit a slight red shift with decreasing temperature compared to the double-segmented NW. The temperature dependence of the PL peak position was fitted using the Varshni equation[111].

$$E_g(T) = E_g(0) - \frac{\alpha T^2}{\beta + T} \quad (\text{Equation 5.1})$$

where T is the absolute temperature,  $E_g(0)$  is the band gap at 0 K and  $\alpha$  and  $\beta$  are the fitting parameters. The values of these parameters for all the three samples are listed in Table 1. The values of  $\alpha$  and  $\beta$  of the NWs are comparable to those of GaAs NWs reported in the literature. An excellent fit is obtained with the Varshni formula for sample N2 over the entire temperature range, while for the single-segmented samples, there is considerable difference between the experimental values and those obtained using Varshni's formula for temperatures below about 110 K. That is, in these latter samples, the temperature-independent portion that is normally observed at the lowest temperatures extends to considerably higher temperatures.

Table 5.1

*Summary of the PL parameter and pertinent PL data*

Sample	Segments	Growth Temperature (°C)	$\alpha$ (eV/k)	$\beta$ (k)	$E_g$ (eV)	Energy at				
						11 K	$E_a$ (meV)	$E_b$ (meV)	$E_{local}^{max}$ (meV)	$T_{deloc}$ (K)
N1-620	1	620	$3.87 \times 10^{-4}$	251	1.328	1.31	51.4	4.5	9.8	90
N1	1	600	$3.75 \times 10^{-4}$	247	1.326	1.31	47.6	6.8	20	127
N2	2	600	$3.7 \times 10^{-4}$	230	1.345	1.34	84.7	10.8	0	72

Where,  $\alpha$  &  $\beta$  = fitting parameters;  $E_g$ = Bandgap energy ;  $E_b$  &  $E_a$  = Activation energy, below and above 100K, ;  $E_{local}^{max}$  = Maximum localization energy;  $T_{deloc}$  = Delocalization temperature.

Table 5.1 lists the values of  $E_{loc}^{max}$  and  $T_{deloc}$ , where  $E_{loc}^{max}$  is defined as the maximum localization energy measured as the largest energetic difference between the experimental PL

peak energy and the value of the energy predicted by the Varshni relation.  $T_{\text{deloc}}$  is the temperature at which delocalization of the carriers is complete.

These quantities are shown in Figure 5.11. The values achieved are comparable in the two single-segmented NWs, but they are considerably lower for the double segmented NW. To understand the nature of the recombination mechanisms, the temperature dependence of the total integrated PL intensity ( $I_{\text{PL}}$ ) was also measured in these samples, as shown in Figure 5.12. The integrated intensity rapidly decreases with increasing temperature, in particular, for temperatures above 80 K. A best fit to the temperature dependence of the  $I_{\text{PL}}$  was obtained using the following phenomenological expression [112]:

$$I_{\text{PL}}(T) = \frac{I_0}{1 + A \exp(-E_a/KT)} \quad \text{Equation (5.2)}$$

The values of  $I_0$ ,  $E_a$  and  $E_b$  that resulted in the best fit to the experimental data in all three samples are also listed in Table 5.1. The values of  $E_a$  and  $E_b$  in the N1 and N1 620 are comparable, but are ~45% smaller than those for the double-segmented sample N2. This implies that there are deeper energy levels in N2 as compared to N1 and N1 620.

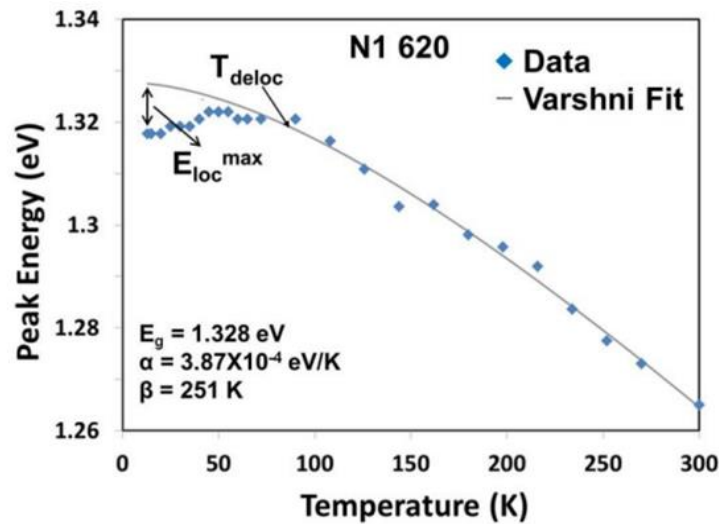


Figure 5.11. Varshni fit for the data of sample N1 620.

The difference between the experimental values and Varshni-predicted PL peak energy, as well as the invariance of the PL peak energy with temperature from 11 K up to 80–100 K and the corresponding very-low-temperature variation of the full width half maxima (FWHM) (see Figure 5.13) in this temperature range, can be considered as a strong evidence for exciton localization. The variation in the PL peak energy as a function of temperature in these NWs can be quantitatively explained as follows: At low temperatures, the excitons are localized either at the defects induced in the NWs by surface irregularities or impurities or at the band-tail states in the density of states (DOS). The latter is more likely as the FWHM significantly varies with temperature. This has been discussed in the later section.

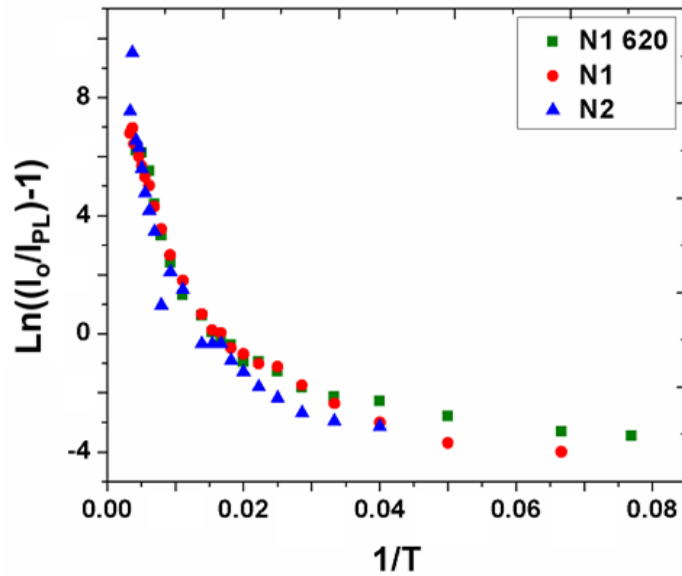
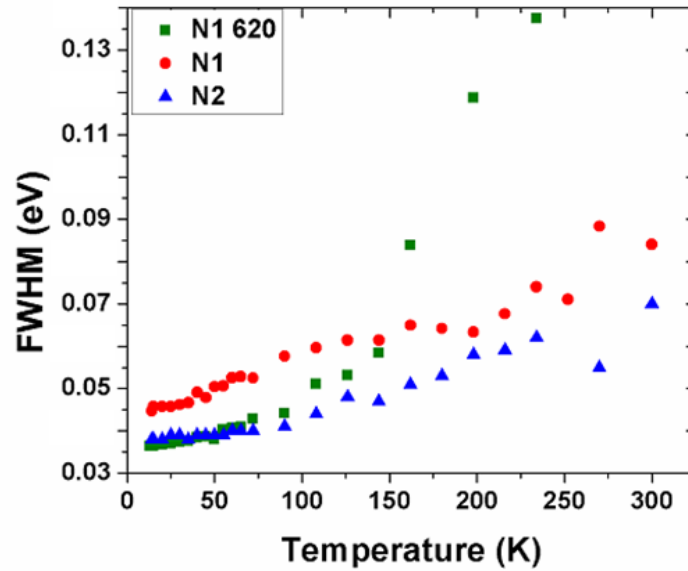


Figure 5.12. Temperature dependence of integrated intensity.

As the temperature is increased above the exciton localization energy identified as  $T_{\text{deloc}}$ , the excitons become delocalized due to dissociation into electron–hole pairs. Above this, the emission energy decreases as a function of temperature due to the band gap shrinkage following the Varshni-like relation. The differences in the PL peak energies observed at low temperature (10 K) and at room temperature in all these samples seem to be similar, ~55–60 meV and, thus,

independent of the GaAsSb segment length. These values are somewhat smaller than 76 meV reported by Chiu et al.[113] in GaAsSb quantum wells (QWs) and 81 meV from the bulk values. Thus, our data suggest that downsizing radially reduces the temperature-induced band gap variation. The delocalization temperature is the lowest for the double-segmented NW with the smallest localization energy and the effect of axial confinement results in opening of the band gap, blue shifting the PL peak energy in the entire temperature range.



*Figure 5.13.* Variation of the full width half maximum (FWHM) with temperature for sample N1, N1 620 and N2.

The value of the FWHM of an excitonic transition in these NWs is representative of the quality of the alloy segments, as well as the extent of the interface roughness[15]. The FWHM of the N2 is the lowest in the entire temperature region, which is an indication of better optical quality of these NWs. The observed variation of the FWHM with temperature in these NW structures can be qualitatively explained as follows: At low temperatures, FWHM reflects the energy distribution of the exciton states in the localizing potentials. As the temperature is raised, the excitons begin to become delocalized. For temperatures above  $T_{\text{deloc}}$ , almost all the excitons

have become delocalized and the exciton optical phonon interaction becomes dominant with the value of the FWHM increasing with temperature[114]. As shown in Figure 5.13, the variation in FWHM with temperature is less and  $T_{\text{deloc}}$  is smaller in sample N2 due to the smaller range of values of the localization energies. In sample N1, the FWHM exhibits a small inverted S-curve, that is, a mild dip in the FWHM curve as the temperature approaches  $T_{\text{deloc}}$ , which is a signature of strong exciton localization normally observed in dilute nitride system [115]. The  $T_{\text{deloc}}$  is considerably larger for this sample. The large value of  $T_{\text{deloc}}$  is consistent with the large  $E_{\text{loc}}^{\text{max}}$  also observed in this sample.

We have analyzed the variation of  $I_{\text{PL}}$  as a function of temperature using equation 5.2 and the values for various fitting parameters for all the three samples as listed in the Table 1. We find that the values of  $E_a$  and  $E_b$  are comparable for the two single-segment wires, but are considerably larger for the N2 sample. For the sample N1 620, the  $E_b$  is 4.5 meV, which is in excellent agreement with exciton binding energy in GaAs. The low activation energy ( $E_b$ ) and the high activation energy  $E_a$  correspond to non-radiative channels that are responsible for determining the quenching of PL intensity at temperatures below 100 K and higher than 100 K, respectively. The low values of 4–10 meV for  $E_b$  indicate that the weak excitons are bound to shallow defects. Higher  $E_a$  at 77 meV has been observed in GaAs NWs grown by Au-assisted catalyst and has generally been assigned to a deep center associated with Au-induced defects[55], which cannot be the case in our NWs since our NWs are Ga catalyzed. Such a deep center has been observed in CdS NWs[116] . The observation of such a deep exciton suggests the presence of the defect complexes in these NWs.

The room temperature PL is realized for the samples grown at 600°C and also, the low-temperature PL peak intensity was considerably higher; particularly, the N2 exhibited the highest

PL peak intensity almost threefold higher than the next largest PL intensity observed in N1. Sample N1 620 had the lowest PL intensity. The lowest FWHM and smallest variation in the FWHM observed for the double-segmented wire is consistent with the better quality of this NW. Conversely, N1 620 showed significant variation in FWHM with temperature and is characterized by low PL peak intensity.

The foregoing discussion of the behaviors of the PL peak energy, excitonic line-width and integrated PL intensity as a function of temperature in our samples suggests that among the three NWs investigated, the double-segmented GaAsSb NW is the better quality NW with reduced defect density of localized states and of non-radiative recombination centers. The temperature dependence of the PL can be well described by a Varshni-like relation for temperatures above 100–150 K. The low-temperature behavior appears to be dominated by excitons bound to shallow defects and two non-radiative channels were found, one weakly bound exciton related and the other related to a deep center, which appears to be influenced by the NW structure.

## 5.7 Raman Spectroscopy

Raman spectra were taken at different locations and representative Raman spectra are shown in Figure 5.13 and summarized in Table 5. 2 for the NWs N1 and N2 and a reference GaAsSb thin film grown on a (001) GaAs substrate. For the reference sample, one should note that the GaAs-like longitudinal optical (LO) and transverse optical (TO) modes occur at 279 and 255  $\text{cm}^{-1}$ , respectively and the intensity of the LO mode is greater than that of the TO mode. This is not unexpected since the TO mode is forbidden for the (100) surface. Its presence is most likely associated with relaxation of the selection rules due to the presence of defects. Very weak GaSb-like TO and LO modes are also observed at 227 and 240  $\text{cm}^{-1}$  in this reference sample.

Table 5.2

*Raman mode data for N1, N2 and the reference GaAsSb epilayer grown on GaAs*

Sample	GaAs TO (cm <sup>-1</sup> )	GaAs LO (cm <sup>-1</sup> )	GaSb TO (cm <sup>-1</sup> )	GaSb LO (cm <sup>-1</sup> )	GaAs TO/ LO	GaSb TO/ LO
N1	266	289	222	235	2.2	0.8
N2	266	289	223	237	1.6	0.73
Reference	255	279	227	240	0.73	0.94

where, TO= Transverse mode, LO=Longitudinal mode

In the NW samples, the spectra exhibit GaAs-like TO and LO phonon modes at 266 and at 289 cm<sup>-1</sup>, respectively, which are in good agreement with the corresponding bulk GaAs values. Compared to the reference epitaxial film, however, the GaAs-like TO and LO modes in the NWs are shifted upward by 10–11 cm<sup>-1</sup>, which are opposite to the downshift in energy reported [117] in GaAs NWs. The FWHM of the GaAs-like TO and LO modes in NWs N1 and N2 are 8/8 cm<sup>-1</sup> and 8/11.1 cm<sup>-1</sup>, respectively.

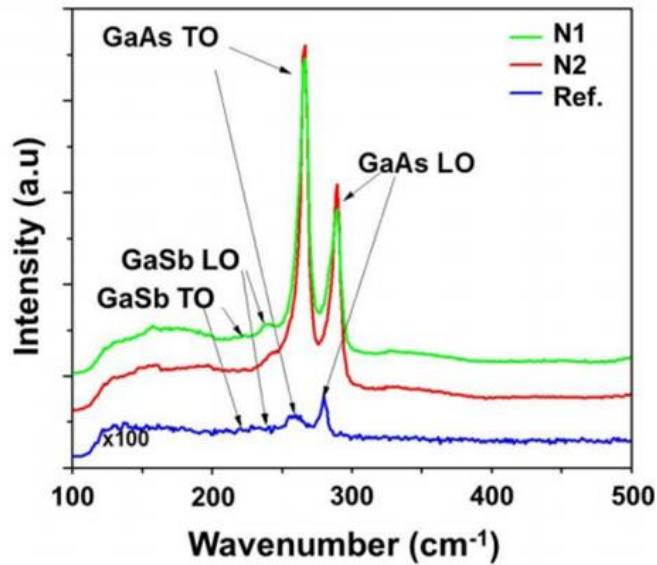


*Figure 5.14.* Raman spectra depicting the GaAs and GaSb like modes of NWs N1 and N2 compared to the epitaxial GaAsSb epitaxial film reference.

These values and the peak positions indicate good optical quality of the NWs. In addition, the GaSb-like TO and LO phonon modes were also observed at 222 and 237  $\text{cm}^{-1}$ , respectively, in reasonable agreement with the corresponding bulk values for GaSb. Note that the GaSb-like modes are downshifted in energy 3–5  $\text{cm}^{-1}$  compared to the reference sample. The GaSb peak intensity scales to the anticipated thickness of the GaAsSb layers in the NWs. The high-intensity ratio of TO to LO phonon modes of GaAs has been commonly observed in GaAs NWs, being the highest for N1 and is attributed [101] to the LO mode being forbidden from certain surface facets as opposed to no such restrictions imposed on the TO phonon modes. A relatively low TO/LO GaAs phonon peak ratio as well as a lower FWHM of these two in NW N2 is also indicative of better quality layers consistent with the PL data discussed earlier.

## 5.8 Conclusions

Segments of GaAsSb NWs on GaAs stem have been successfully grown by MBE, using a Ga-catalyzed VLS technique. The two-segmented GaAsSb NWs were found to be of excellent optical and structural quality as attested by low FWHM and their temperature variation in the corresponding PL spectra, as well as low TO/LO ratio was observed for both GaAs and GaSb LO peaks. TEM of these NWs revealed both GaAs and GaAsSb to be of ZB phase for the wire terminating without any Ga droplet. The stacking faults and twins were found to be present in all the NWs.

## CHAPTER 6

### Optimization of GaAs NWs on a Non-etched Si Substrate

#### 6.1 Introduction

For increasing the overall emission efficiency of nanowire devices, it is important to use the entire surface available on the device. In order to get maximum output, there is ongoing research to get 100 % thin vertical NWs. Using techniques namely, e-beam lithography [118] and patterning of the substrates [119], various groups have achieved ~ 100 % vertical NWs. But these methods involve high cost and were out of the scope for this current research. Although self-catalyzed GaAs NWs with GaAsSb inserts were grown successfully, further optimization of the growth conditions needs to be addressed to achieve a high yield in the density of the NWs with high % of vertical NWs.

All the GaAs/GaAsSb NWs examined in this section were grown on non-etched Si (111) substrate as in the previous chapter and the focus is on determination of interplay of growth conditions, namely, V/III ratio, initial Ga opening duration ( “Ga opening” refers to the duration of opening of the Ga shutter of the SUMO cell), fluxes of adatoms and growth temperature on the NW density and verticality of the NWs. Effects of different species of As namely, As<sub>2</sub> and As<sub>4</sub> were also the subject of investigation.

#### 6.2 Experimental Details

Two growth temperatures of 600°C and 620°C were chosen for investigation based on the literature review [120] for a V/III ratio varying from 6 to 20 and for three Ga shutter opening times of 0,4 and 15 sec prior to the growth. Along with this, the As species was also changed from As<sub>2</sub> to As<sub>4</sub>. These variations are listed out in Table 6.1 along with their density and the overall % of bent NWs. All these samples were grown on epitaxially intrinsic Si (111) wafers. For

the initial growths, these substrates were rotated with a rpm of 30. For later growths it was optimized at 7 rpm.

Table 6.1

*Shows the list of samples grown during the optimization process*

Sample number	Growth Temperature	V/III	Ga shutter opening	Anneal time	Anneal temp	rpm	As type	Density ( $\times 10^8 / \text{cm}^2$ )	Bent\Vertical ( $10 \times 10 \mu\text{m}^2$ )	% Bent over all
<b>GaAs NWs with initial growth condition</b>										
092112C	620	6	8	5	620	30	2	0.04	20\81	19
102412A	620	6	8	5	620	30	2	0.5	17\83	17
<b>GaAs NWs with optimized growth condition</b>										
011014C	600	6	4	10	600	30	2	0.034	4\28	12.5
011514A	600	10	0	10	600	30	2	3.59	0\152	0
012114A	600	10.9	0	5	600	30	2	4.55	0\193	0
020714A	620	15	4	5	620	30	4	1.04	37\88	29
030514B	620	17	15	5	620	7	4	1.5	41\122	25
031214B	620	15	15	20	620	7	4	2.06	75\143	34
032414C	620	20	15	20	620	7	4	3.16	91\244	27

### 6.3 Optimization Process

Figures 6.1(a) and (b) show the 45° tilted side view of the GaAs NWs on Si substrate with As<sub>4</sub> as the flux constituent for two V/III ratios of 6 and 15. The NWs grown at 620°C are generally a combination of both vertical and bent. The vertical NWs are uniform in diameter and cylindrical in shape whereas the bent NWs are conical with tapering towards the top of the NWs. It was observed that at constant "Ga opening", if there is an increase in V/III ratio, density increases till it reaches 0% bent wires. As per Figure 6.2, when the V/III ratio increases from 6 to 15, the density increases from  $2.06 \times 10^6 \text{ cm}^{-2}$  to  $9 \times 10^7 \text{ cm}^{-2}$ .

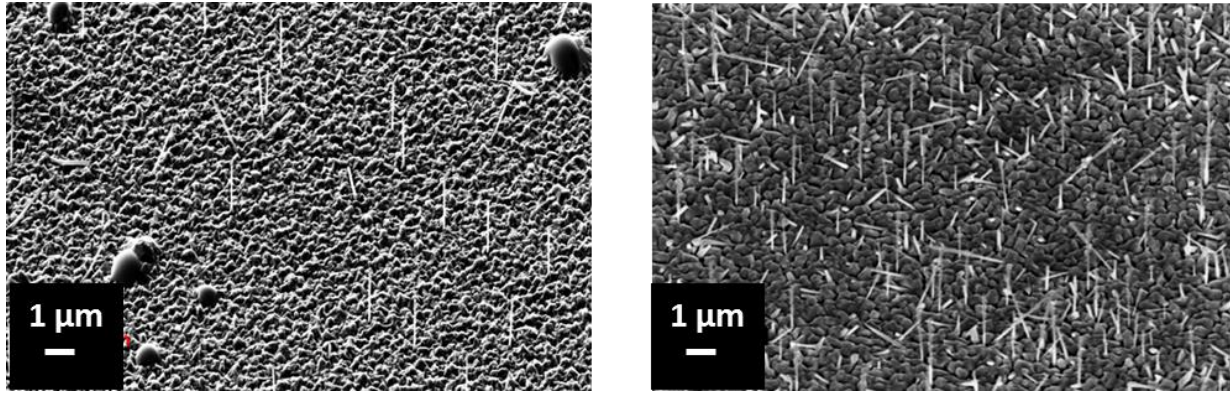


Figure 6.1. Cross section SEM images of GaAs NWs on Si (111) substrate with a change in V/III ratio with (a) 6 (b) 15.

After a number of iterations performed which is summarized in the Table 6.1, there were certain growth conditions obtained that produced NWs which were more vertical and with a density  $> 10^8 \text{ cm}^{-2}$ . Different factors that were varied in this process were: growth temperature, V/III ratio of the growth species, Ga shutter opening, annealing time of the substrate, the substrate rotation per minute (rpm), and the As species in particular.

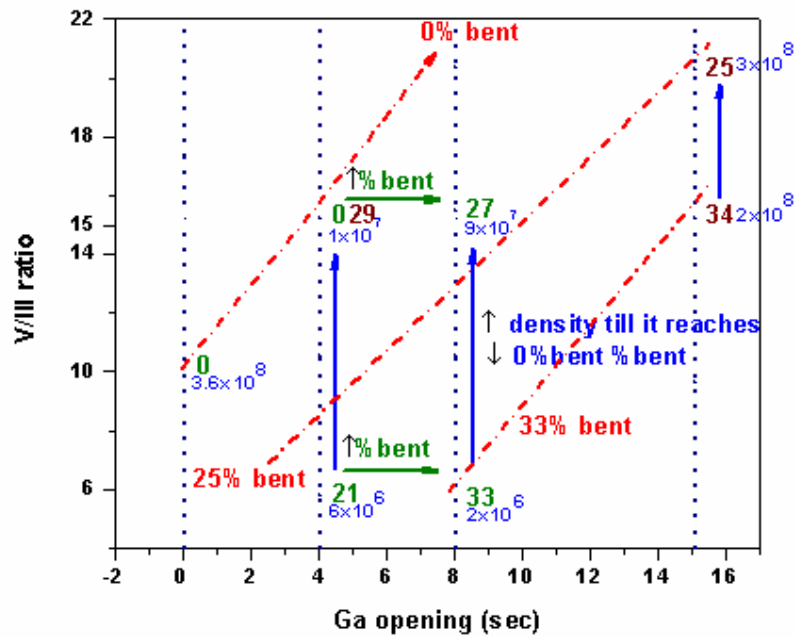


Figure 6.2. Variation in the Ga opening vs V/III ratio (Green and brown color corresponds to

As<sub>2</sub> and As<sub>4</sub> respectively). This plot also depicts a variation of NW density (values in blue) with change in the % of bent NWs.

Comparing the samples from Table 6.1, the samples grown at 600°C with As<sub>2</sub> as group V element, generally exhibited a highest percentage of vertical NWs as compared to the ones grown at 620°C with As<sub>4</sub>. It was also noticed that at constant V/III ratio, if there is an increase in "Ga opening", the % bent wires increases (Figure 6.2). This is also correlated with the density of the NWs. For a constant Ga opening duration and growth temperature (in this case at 620°C), the NW density increases with increase in V/III ratio. A high V/III ratio means large supply of As adatoms leading to high supersaturation resulting in growth of large number of NWs. Apart from higher density, the vertical nature of the wires is also necessary for a device with higher efficiency. The red dotted lines in Figure 6.2 shows the extrapolation for the occurrence of 0% bent NWs with variation in Ga opening and V/III ratio. For a given V/III ratio there is a threshold Ga opening which corresponds to all vertical NWs and above which the % of bent wires starts increasing. At higher Ga opening, the occurrence of all vertical NWs is restricted by the pores in the native oxide layer on Si (111) substrate. NWs will grow in [111] direction only when the NW bottom is epitaxially in contact with Si (111) substrate. When the initial Ga droplet size is smaller than the pore size, Ga will be in directly contact with Si (111) through pores leading to NW growth in [111] direction. Conversely, when the Ga droplet is bigger than the pore size, Ga may not be in direct contact due to native oxide which leads to NW growth in multi directions. At a particular Ga opening, the percent of vertical NWs increases with increasing V/III ratio. It is also observed that, the density of the NWs increased with increasing V/III ratio until it reaches a minimum percent of bent wires at that particular Ga opening. Switching from As<sub>2</sub> to As<sub>4</sub> results in better uniformity in addition to slight increase in the axial growth rate (5.3

nm/sec to 6.2 nm/sec). Based on these experimental data, the conditions for almost 0% bent NWs were predicted as shown in the Figure 6.2 above. With a Ga opening of 15 sec and V/III ratio of 16, the result was optimum with highly vertical NWs and a density of  $2 \times 10^8 \text{ cm}^{-2}$ .

**6.3.1 Effect of annealing.** The samples were annealed at 3 different durations of 5, 10 and 20 minutes at 620°C just before Ga opening on the substrate. Keeping the same growth conditions, it was found that when the annealing time is increased, there is an increase in the densities of the NWs (as shown in Figure 6.3). So, for an annealing time of 20 minutes, a Ga opening of 15 sec and a V/III ratio of 20, the density was  $5.9 \times 10^8 \text{ cm}^{-2}$ . Although a higher density of NWs was achieved for longer annealing duration, the density is highly dependent upon the Ga droplets and the nano pores formed.

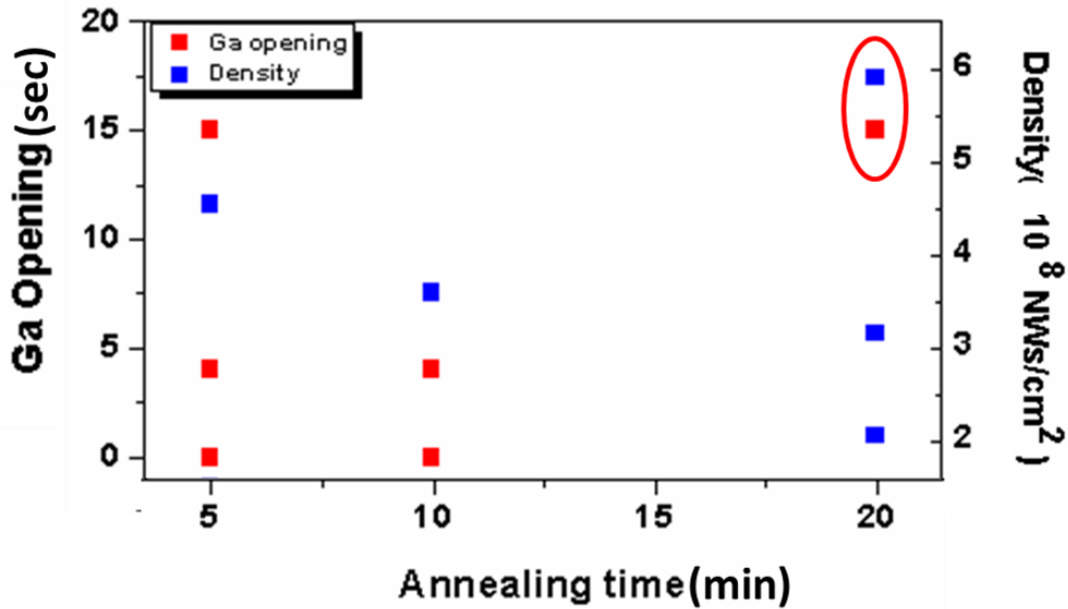


Figure 6.3. Plot of samples with different annealing time vs Ga opening and densities.

With increased annealing time, the amount of Ga opening along with V/III ratio should be increased. Annealing allows the formation of nano pores from the thin naturally occurring  $\text{SiO}_2$  layer. When this surface is exposed to the Ga droplet, based on the surface energy of the

substrate, the droplet forms nuclei at certain angle which generally guides the direction of these NWs. As there is more Ga accommodated, higher the density of the nucleus resulting in more number of NWs. Figure 6.4 below shows a comparison of the change in the % bent NWs with density, Ga opening and annealing time and is a graphical representation of Table 6.1.

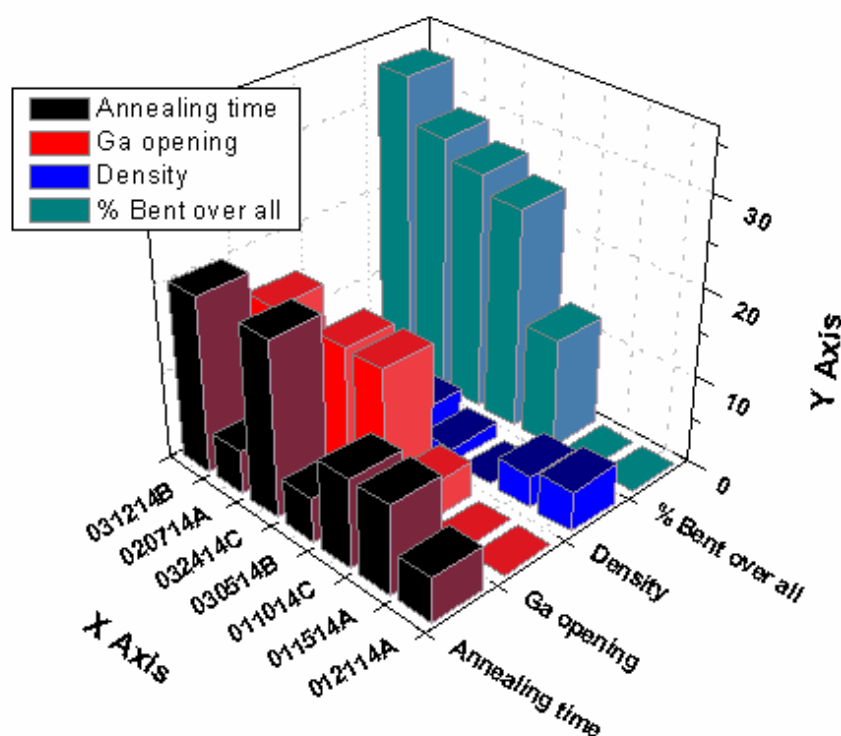


Figure 6.4. Graph depicting the increase in the % of bent NWs with the change in the annealing time, Ga opening and density of the NWs.

**6.3.2 Comparison between  $As_2$  and  $As_4$ .** Comparing samples, 020414A and 020714A, we can see that there is increase in the density from  $As_2$  to  $As_4$ . There is increase in NWs length for sample from  $As_2$  to  $As_4$  (1.5 to 2.9  $\mu m$ ) indicating the growth rate is higher for  $As_4$ .  $As_4$  leads to growth rate twice as fast than when  $As_2$  is used indicating that the diffusion length of Ga is smaller for  $As_2$  than  $As_4$  which is consistent with the literature [121, 122]. The % of bent NWs found in  $As_4$  was found to be more as compared to  $As_2$  as can be seen from the graph. The plausible reason could be  $As_4$  has lower chemical potential in gaseous phase. This will in turn

promote the increase in the radius of the Ga droplet. Larger the radius, tendency of the nuclei to incline to one direction increases, which in turn produce more of bent NWs for  $\text{As}_4$  species.

Considering the shape of the NWs, the NWs are more cylindrical and uniform in shape for  $\text{As}_4$ , whereas it is found to be conical in shape for  $\text{As}_2$ . The cylindrical NWs in case of  $\text{As}_4$  could again be attributed to the longer diffusion length of Ga that results in a uniform diameter NW.

#### **6.4 Conclusion**

In conclusion, optimized conditions for achieving high density and highly vertical GaAs NWs are demonstrated. It was observed that for at constant "Ga opening", with an increase in V/III ratio, density increases to maximum vertical wires. This could be due to the non-epitaxial contact of NWs with Si (111). At constant V/III ratio, when there is an increase in "Ga opening", the % bent wires increases. Since the epitaxial contact between NWs and Si (111) is prevented by the native oxide layer on Si (111), we attempted to prepare the substrate by making the native oxide layer sufficiently thin so that Ga can come in contact with Si (111) through the pores leading to vertical NWs. So, with an optimum nanopore size, the Ga opening should be fixed. In such a condition the V/III ratio should be increased steadily till the optimum result is achieved.

## CHAPTER 7

### Optimization Process on Etched Si Substrates

#### 7.1 Introduction

Over the past few years, extensive work has been done on the self-catalyzed growth of NWs [30] [21, 42]. This type of growth has been associated with the existence of plane or patterned  $\text{SiO}_2$  surface whose thickness plays an important role in the NW growth. When a pure Si surface is exposed to the ambient atmosphere, a thin layer of  $\text{SiO}_2$  forms on its surface based on the type of dopant [123]. There is considerable strain developed when an oxygen atom tries to accommodate between the Si-Si bonds changing the bond length of Si-Si from 2.3 Å to Si-O-Si group of 3.0 Å [123]. Incorporation of oxygen on the silicon substrate involves displacement of silicon atoms from their sites. Oxidation process is further enhanced if the surface is rough where the oxygen has more chances of forming siloxane (Si-O-Si). Based on the substrate orientation too, the surface roughness varies. For example, after a wet chemical treatment the Si (111) has more surface roughness as compared to Si(100) due to higher density of interface energy states in Si(100) [124].

In this chapter, 1x1 cm square Si (111) substrates were etched using piranha solution + diluted HF and were allowed for an ambient air oxidation. NWs samples were grown on samples of different thickness. Atomic force microscopy was performed for measurement of the roughness of the  $\text{SiO}_2$  layer formed during the oxidation process. Scanning electron microscopy measurement with a cross section view of the sample showed the density and morphological characteristics of the NWs.

## 7.2 Experimental Details

The etching process was performed on both intrinsic and p type Si (111) substrate. Initially it was done on intrinsic Si (111) substrates which were chemically etched by treating with the piranha solution for 10 minutes and then dipped in diluted HF solution. The native oxide thickness was reduced by dipping it in HF for 2 s, 10s, 20s, and 40 s. This was followed by oxidation in ambient atmosphere at room temperature. The oxidation process was varied from 2 hours to 2 days to produce desired SiO<sub>2</sub> thickness. Once the substrates were ready, they were baked at 200°C for 8 hours in the introduction chamber of the MBE system and the NWs were grown for 1 hour. As<sub>4</sub> was used as group V species during these growths. The V/III ratio used was 20, with an initial Ga opening of 15s at a growth temperature of 620°C. The substrate was in a stationery position where it was annealed for 5 minutes. The growth temperature for Ga-assisted growth was chosen as 620°C. The As/Ga flux ratio was kept constant for all the samples at an As<sub>4</sub> beam equivalent pressure (BEP) of  $2.5 \times 10^{-6}$  Torr. The samples were grown at 620°C with a V/III ratio of 20. The structural and optical characteristics were performed using scanning electron microscopy (SEM) images from a Zeiss EVO 10 and the photoluminescence using the PL setup as explained in Chapter 3.

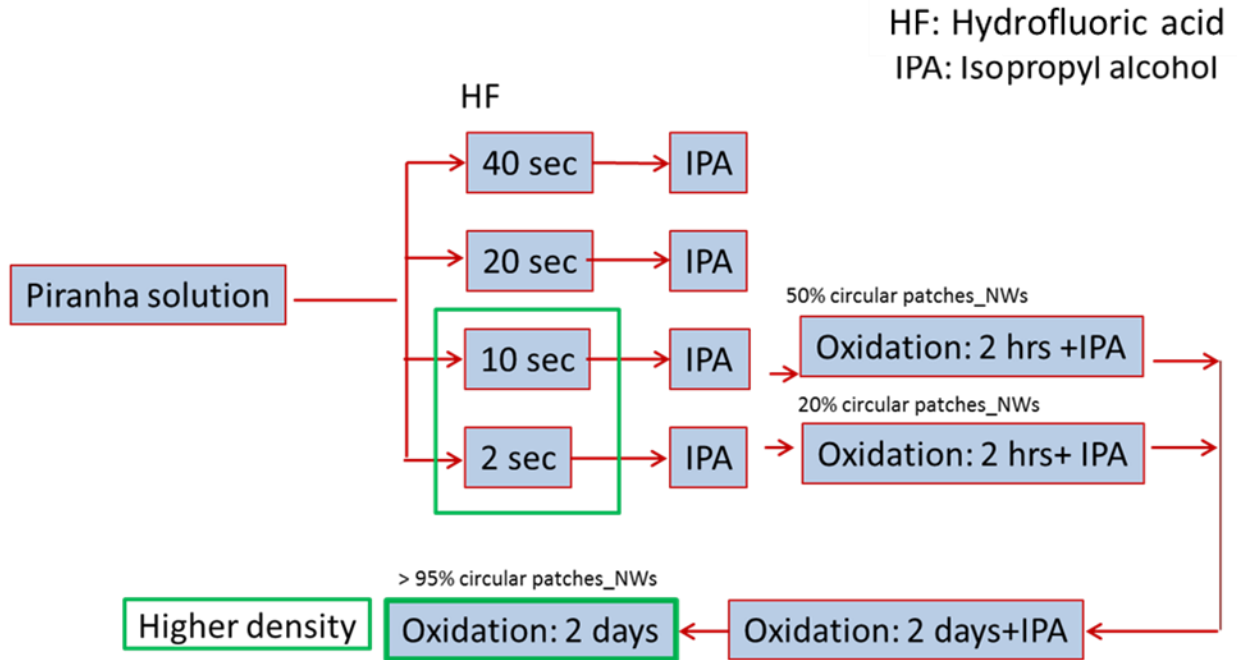


*Figure 7.1.* Schematic diagram of the etching process performed on the intrinsic Si (111) substrate.

For the p-type Si (111) substrates were treated with the piranha solution and then dipped in HF (for a duration varying from 2s to 30s). This was followed by the oxidation in ambient atmosphere. The oxidation process was varied from 2 days to 3.5 hours to produce desired SiO<sub>2</sub> thickness as shown in the Figure 7.2 below. Once the substrates were ready, they were baked in the introduction chamber of the MBE system and the NWs were grown for 1 hour. The V/III ratio used was 20, with an initial Ga opening of 15s at a growth temperature of 620°C. The substrate was in stationery position where it was annealed for 5 minutes. The NWs obtained were characterized with the same instruments as mentioned above.

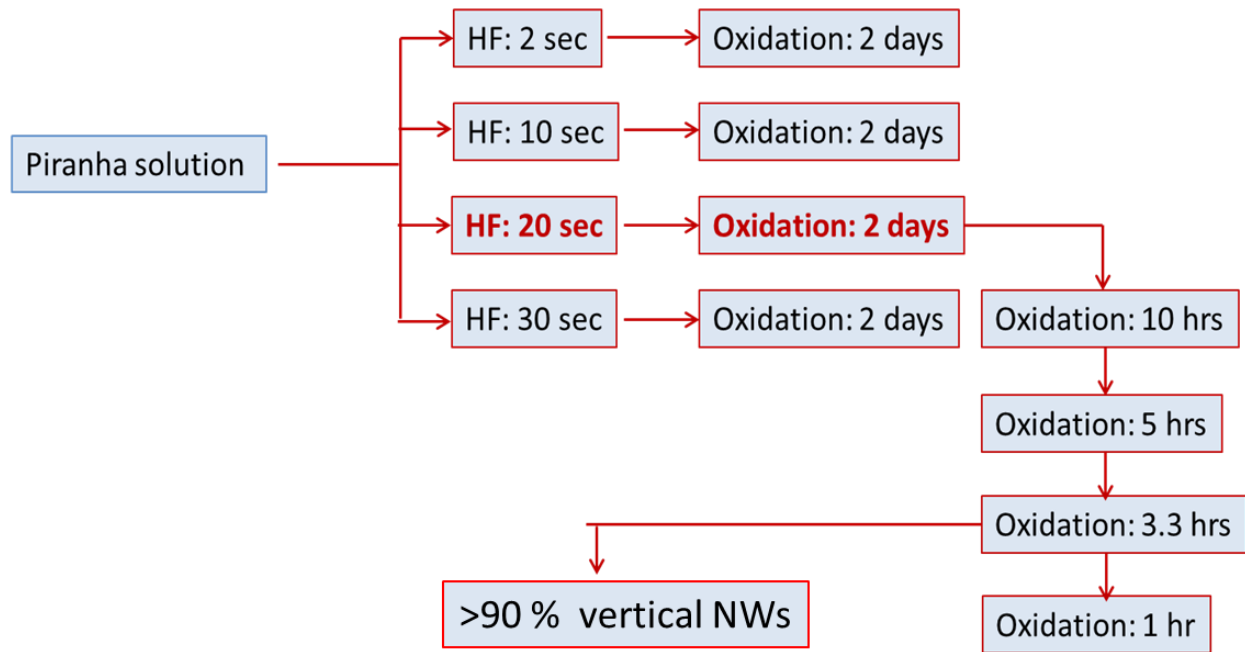
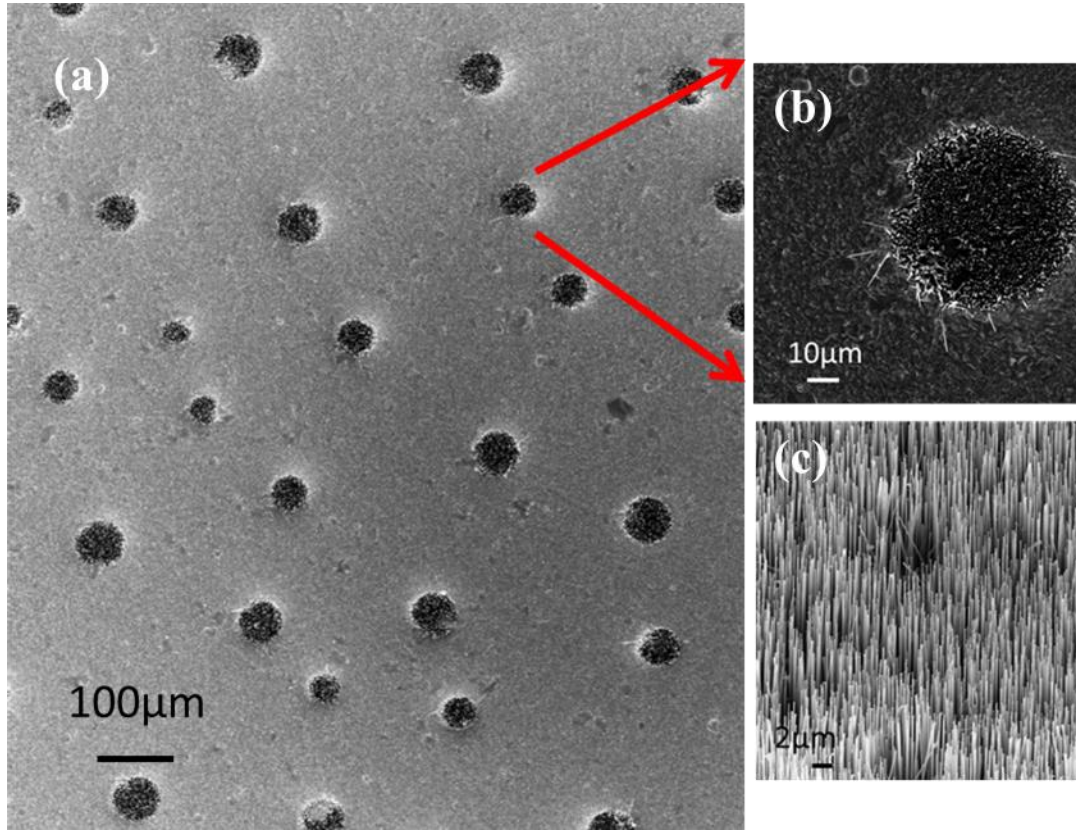


Figure 7.2. Schematic diagram of the etching process performed on the p- type Si (111) substrate.

### 7.3 Optimization Process on Etched Si (111) Substrates

Figure 7.3 shows the top view of the NWs with intrinsic type Si substrates prepared with 2 hours of oxidation after etching. It shows a clear variation in the orientation of the NWs with the change in the oxide thickness. For 10s HF dip followed by 2 hours of oxidation, there were circular patches of NWs, showing the right amount of SiO<sub>2</sub> layer that was formed after etching as circular patches. These patches had more than 90 % vertical NWs and a density  $\sim 2 \times 10^8 \text{ cm}^{-2}$ . Figure 7.3 (b) and (c) shows one of those circular patches with closer view. Under 2 days of oxidation, the NWs were formed throughout the sample instead of the circular patches. This could be due to formation of the required oxide layer. Comparing both the intrinsic and p type substrate, there was difference in the oxidation time for the formation of SiO<sub>2</sub> layer. The

densities of the NWs obtained were same on both which could be due to the formation of right amount of  $\text{SiO}_2$  layer. For future analysis, p type Si substrate was preferred due to its applicability in device making.



*Figure 7.3.* (a) SEM image of circular patched GaAs/GaAsSb/GaAs NWs with  $> 90\%$  vertical orientation.

The AFM results as shown in Figure 7.4 coincide with the expected rough surfaces which were predominantly the  $\text{SiO}_2$  patches on the Si substrate. The NWs obtained were broader at the bottom and had an inclination of  $83.8^\circ$  from the base. Its diameter was on average 127 nm with a length of  $\sim 2.5\mu\text{m}$ . Hexagonal facets were clearly noticed for the NWs grown on these substrates.

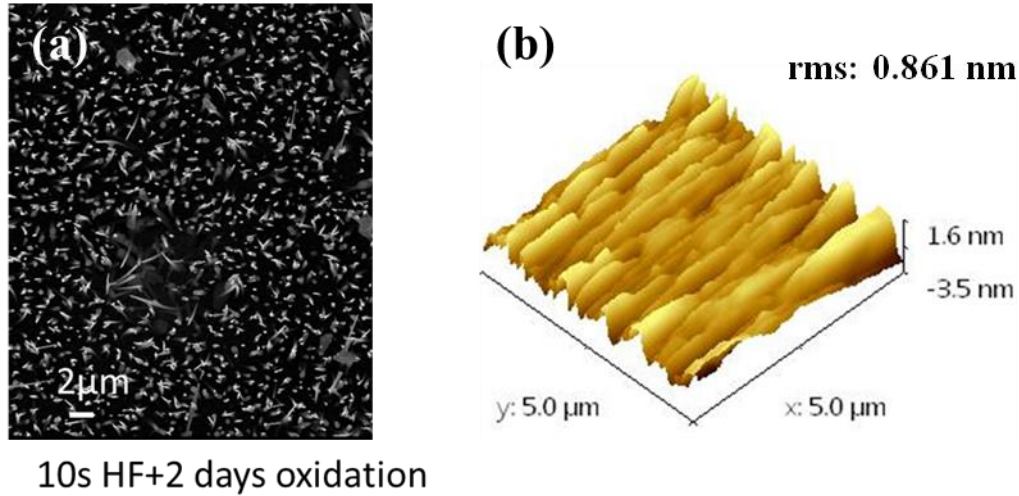


*Figure 7.4.* AFM image on the optimized substrate showing the formation of  $\text{SiO}_2$  and the corresponding top view SEM of the nanowires.

Raider et al. [125] reported that the native oxide thickness on Si (111) is  $\sim 16 \pm 2 \text{ \AA}$ . By keeping the piranha solution etch time constant, we have varied the HF (1%) etch time to alter the native oxide thickness. The etch rate of 1% HF after piranha treatment measured by ellipsometer on a thick oxide layer is  $0.44 \text{ \AA/s}$ . The resultant native oxide thickness after piranha + 20 s HF (1%) chemical treatment on Si (111) is  $\sim 7.1 \pm 2 \text{ \AA}$ . Now we have allowed a fresh native oxide to grow through oxidation at room temperature. Raider et al. [125] reported that the growth rate of native oxide at room temperature on Si (111) is  $2\text{-}3 \text{ \AA/hr}$  for the first one hour and slows down to  $0.03 \text{ \AA/hr}$  thereafter. Growths were performed on substrates with different oxidation timings ranging from 1 hr – 48 hrs. Figure 7.5 below shows the atomic force microscopy (AFM) results of the substrates. Substrate samples with an oxidation timing of 3.3hr, 24 hr and 48 hr were analyzed. The roughnesses of the substrates for these conditions were 2.57 nm, 3.13nm and 0.22 nm, respectively.

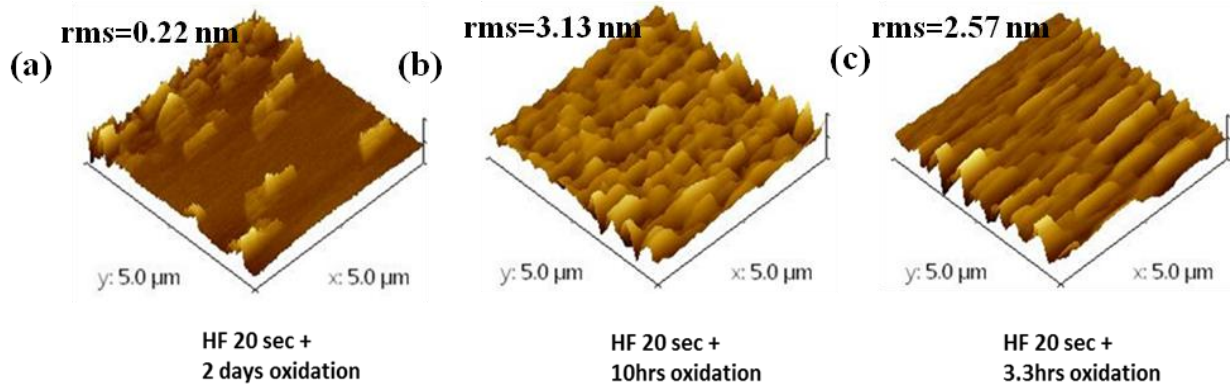


Figure 7.5. AFM image of Si (111) substrate with different oxidation timings.

Figure 7.6 depicts the decrease in the percentage of bent wires with decrease in the oxidation time and also shows increase in the density of NWs from  $2 \times 10^8/\text{cm}^2$  to  $8 \times 10^8/\text{cm}^2$ . The optimum condition for  $\sim 90\%$  vertical NWs was found to be 3.5 hrs oxidation i.e.  $\sim 9.1 \pm 2 \text{ \AA}$  oxide layer is optimum for highly dense and vertical NWs as shown in Figure 7.6(c). The roughness of oxide layer leads to formation of nano-faceted Ga/Si interface which results in NW growth in several alternative directions. Miccoli et al.[126] reported that each nano facet is parallel to  $\{n11\}$  planes of Si for Au/Si interface.

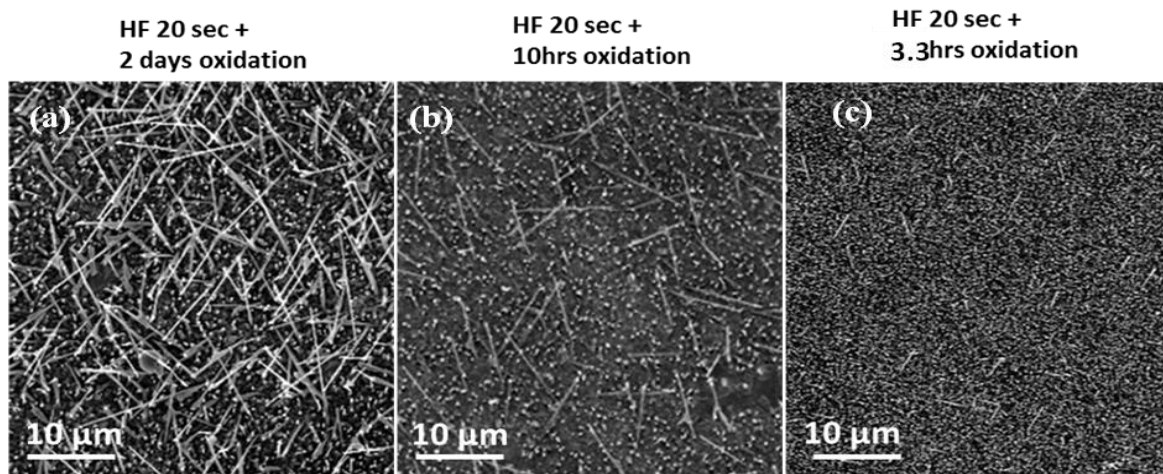
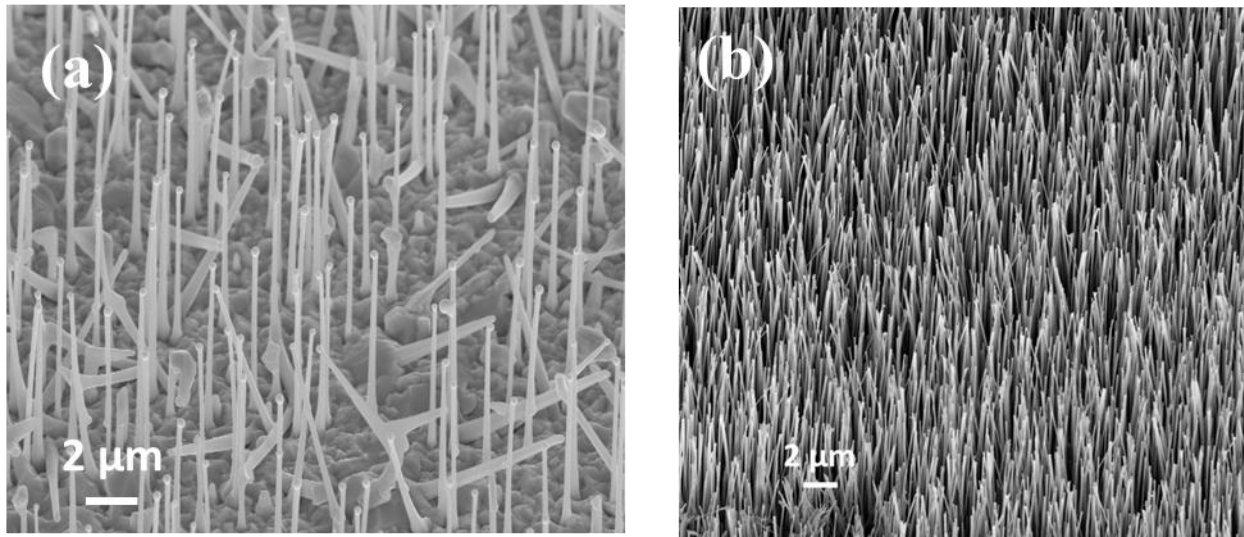


Figure 7.6. SEM images show the top view of the NWs grown on Si (111) with different oxidation timings from (a) 48 hrs (b) 10 hrs and (c) 3.3 hrs.

#### 7.4 Comparison of the GaAs/GaAsSb/GaAs NWs on both Etched and Non-etched substrates

The initial growth conditions used to grow the NWs were on epi-ready non etched Si (111) substrate. These samples are identified as NE1. The substrates were blown with dry nitrogen gas and were annealed in the introduction chamber at 200°C for 8 hours. Then the growth was performed which has been described in the previous chapters. In case of etched substrates, the 1x1 cm square Si substrates were chemically treated with piranha solution for 10 minutes followed by dip in diluted HF. The substrates are allowed for dry oxidization and based on the number of exposure hours there is  $9.1 \pm 2$  Å oxide layer. Due to the oxide layer formed there is a variation of the density of the NWs and also on the verticality of the NWs. Naming this sample as E1, we compare their properties subsequently.



*Figure 7.7.* SEM images of GaAs/GaAsSb/GaAs NWs on (a) non-etched substrate and (b) etched Si substrates.

Figure 7.7 shows the variation in the orientation and density of the NWs on non-etched and etched substrate. The NWs grown on non-etched substrate has a total length of 5.1  $\mu\text{m}$  in which the GaAs stem was  $\sim 1.3 \mu\text{m}$  with the GaAsSb insert of 3.5  $\mu\text{m}$  and typical diameter of the NWs was 150-180 nm. Almost 70% of the NWs were found to be vertical with a density of  $3 \times 10^7/\text{cm}^2$ . The NWs grown on etched substrate were slightly arced and has hexagonal facets and the diameter of the NWs was 123-130 nm with a higher density of  $> 10^8/\text{cm}^2$ . The change in the diameter of the NWs might be due to the changes in the growth parameters which were optimized for high density of NWs.

Other than the  $\text{SiO}_2$  layer, there are other factors affecting the structure of the NWs. NWs exhibit salient differences in the shape and growth rate, depending on the nature of the As flux used. Use of  $\text{As}_2$  flux resulted in NWs with larger diameter  $\sim 200$  nm at the bottom of the NW compared to 120 nm for those grown under  $\text{As}_4$ . Secondly, NWs were broader at the base and gradually tapered to the top while the use of  $\text{As}_4$  source resulted in NWs of uniform diameter. This type of morphological change indicates a sufficiently large lateral growth on the sidewalls. Now based on the ratio of the adatom diffusion length to that of the NW length, there is possibility of nucleation along the NW sidewall [127]. Finally, axial growth rate was found to be lower (2.83 nm/s) with  $\text{As}_2$  when compared to the growth rate of 3 nm/s with  $\text{As}_4$  flux. These differences are indicative of the effect of As species on the diffusion length of Ga, which is reported [127] to be reduced by half under  $\text{As}_2$  species than  $\text{As}_4$ . Hence, the use of  $\text{As}_2$  species results in lower axial growth rate and tapered NWs due to the inability of the Ga to diffuse to the top with increase in the length of the NWs and also leading to higher radial growth rate.

In order to estimate the lifetime of carriers, it is important to understand the nature of the defects and the possibilities of non-radiative recombination centers. Figure 7.8 below depicts 4K

photoluminescence (PL) spectra of the NWs. The temperature dependence PL peak fit was performed using the Varshni relation. In our recent report on GaAsSb NWs, extensive work was done on temperature dependence of the PL of these NWs[95]. In case of excitons, as the temperature increases, they get sufficient thermal energy and overcome the nearby energy states with localization energy. These excitons generally recombine with low energy which we term as  $E_a$ . In our case, this phenomenon happens from 4K till 65K, where the  $E_a$  varies from 4.51 to 4.85 meV. This emission could be due to the occurrence of the surface defects along the NW structure or at the band tail states in the density of states. The latter is more likely due to the following reasons. Firstly, due to significant variation in FWHM of the PL signal from 38 meV at 4K to 116 meV at room temperature, secondly the surface defects are expected to be comparatively fewer in (111) oriented NWs and thirdly the surface defects are reported to be pinned about 0.25 eV below the conduction band. The second activation energy,  $E_b$  (Figure 7.8(b)) seems to vary considerably between the NWs NE1 (non- etched substrate) and E1 (etched substrate) from 51.4 meV to 1.3 meV respectively. NE1 NWs seems to produce a much deeper level and E1 NWs on the other hand displays an extremely shallow level. Hence, the lower PL intensity obtained in E1 is speculated to be caused by the presence of this shallow level. As the temperature increases, the excitons gain more energy and become further delocalized and follow the Varshni relation.

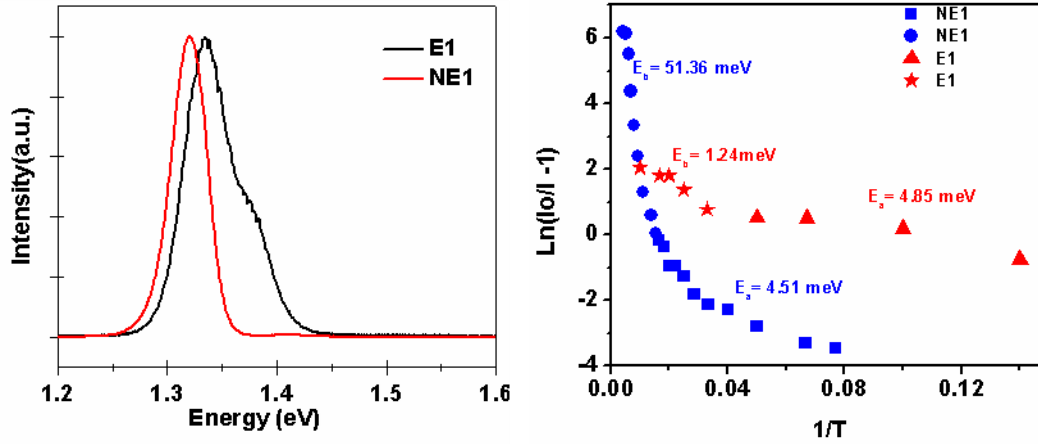


Figure 7.8.(a) Low temperature photoluminescence spectra of the single segmented GaAsSb NWs. Here NE1 (non-etched) indicates the NWs with single segment and E1 (etched), the NWs with single segment with high densities. (b) Plot for calculating the activation energies for both single segmented NWs.

Figure 7.9 shows the Raman spectra of sample NE1 (non- etched substrate) and E1 (etched substrate) depicting the GaAs and GaSb like TO and LO modes. Both the spectra exhibit the GaAs like TO and LO modes at  $266$  and  $289$   $\text{cm}^{-1}$ , respectively. In case of E1, there is shift towards the lower wavenumber from  $290$   $\text{cm}^{-1}$  to  $283.4$   $\text{cm}^{-1}$  for the GaAs like LO mode. This could be due to the small size of the E1 nanowires that define the Raman correlation length or due to any coaxial strain developed in the nanowires [90]. This can be correlated with strain developed in the arcing of the nanowires as found in the SEM micrographs.

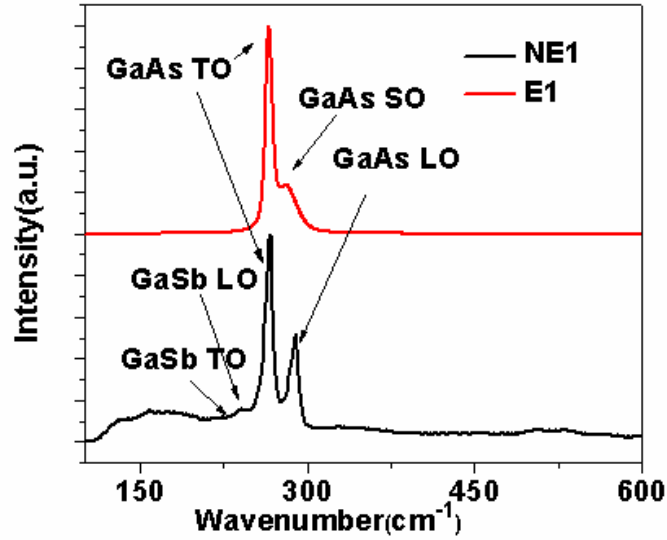


Figure 7.9. Raman spectra depicting the LO and TO modes of GaAs and GaSb.

The FWHM of the GaAs like TO and LO mode for NE1 is  $8/8\text{cm}^{-1}$ . The low FWHM shows the good quality of the NWs. Also the lower TO/LO intensity ratio of NE1 as compared to E1, indicates better quality of NWs. For the E1, the FWHM for the GaAs like TO and the shifted LO mode are  $8.7$  and  $20.7\text{ cm}^{-1}$ , respectively. The broadening of the FWHM of the LO mode clearly shows the strain present in the E1 sample which is consistent with the SEM results and the occurrence of the twin planes as confirmed by TEM analysis. It has been shown that there are possibilities of SO mode which would be arising from the hexagonal cross section of the GaAsSb NW. But in our case, due to the higher diameter and occurrence of the peak at  $283.4\text{ cm}^{-1}$ , this possibility can be neglected. Based on the analysis, the E1 NWs, having a 4.5 at. % Sb composition in its insert accommodates strain and defects, though there is considerable improvement in its density and alignment of the NWs. Another reason for the low quality of the E1 NWs could be the stationary position of the substrates during the growth. Further investigation is needed for reduction of this strain and better incorporation of Sb into the NWs.

## 7.5 Conclusion

In conclusion, Ga assisted GaAs NWs with GaAsSb segments were grown on both etched and non-etched epitaxial Si substrate. The NWs grown on etched substrates with the optimum oxide layer were higher in density and vertically aligned as compared to the NWs on the non-etched substrate. This clearly indicates the critical role of optimum oxide layer thickness for achieving vertical and high density NWs. NWs under  $As_2$  lead to higher radial growth rate whereas in case of  $As_4$ , axial growth rate was favored with respect to radial. Temperature dependence photoluminescence showed the presence of shallow defects for the NWs grown on the etched substrate. Based on Raman analysis, quality of the NWs was of slightly inferior quality as evidenced by a broader FWHM and higher TO/LO ratio. For the sample with higher density arcing of the NWs is attributed to the increased strain resulting from increased Sb incorporation. Further study needs to be done for improving the quality of GaAsSb nanowires with higher density.

## CHAPTER 8

### Compositional variation of Sb in Ga Assisted Axial GaAs/GaAsSb/GaAs

#### Heterostructure Nanowires on Chemically Etched Si Substrate

### 8.1 Introduction

GaAs/GaAsSb NWs have been promising structures for the near IR region for its application in the devices like photodetectors on a nanoscale. But for applications closer to the optical window of 1.3  $\mu\text{m}$ , the Sb composition needs to be varied in these NWs. But varying the Sb composition through standard epitaxial techniques is typically very challenging. There are several factors such as large miscibility gap for ternary alloys, the low vapor pressure for elemental Sb and the tendencies for the materials to include material defects. To date, there have been several reports on the axial heterostructure growth of both Au assisted and Au free GaAs/GaAsSb NWs by MBE [15, 30, 128]. Extensive photoluminescence study has also been performed for a better understanding on its structure [129]. There have been several reports that GaAsSb as an insert in GaAs NW producing emission peaks at 1.26 eV and 1.25 eV [29]. In fact, further Sb incorporation in such a structure has the potential of driving the wavelength towards the telecommunication spectrum. Moreover, vertical growth of such structures would improve the device efficiency.

In this work, Sb composition was varied from 1 to 4.5 at. % in the axially grown GaAsSb insert. Ga assisted GaAs/GaAsSb axial heterostructures grown by molecular beam epitaxy on etched Si (111) substrates have been studied. Four sets of single inserted GaAs/GaAsSb NWs samples with different at. % compositions of Sb varying from 0 to 4.5 were used to perform a systematic study on the effect of Sb incorporation in the axial structure and correlate to its optical properties.

## 8.2 Experimental Details

All the NWs were grown on chemically etched p-type Si (111) substrates by the conventional EPI 930 MBE system. The substrates were initially etched with piranha solution and HF followed by oxidation in ambient atmosphere. The entire NW growth was accomplished in three parts, i.e., GaAs stem, GaAsSb insert and GaAs cap. Initially, the GaAs stem was grown for 112seconds, followed by the GaAsSb as an insert for 15 minute with GaAs cap for 112seconds at the end. After loading the substrate into the growth chamber, the NW growth was initiated by first opening the Ga shutter for 15s followed by the opening of As<sub>4</sub> flux ( $4.8 \times 10^{-6}$  Torr BEP) for the growth of GaAs as the NW stem. The GaAsSb insert growth was then performed by allowing Sb flux which varied for achieving the different compositions. A GaAs cap layer was grown by terminating the Sb flux. The heterostructured NWs of GaAs (0 at. % Sb), GaAs/GaAsSb/GaAs (1 at. % Sb), GaAs/GaAsSb/GaAs (2.6 at. % Sb), GaAs/GaAsSb/GaAs (4.5 at. % Sb) referred as S1, S2, S3 and S4, respectively, were grown. The samples were characterized by various instruments which are mentioned in details in chapter 3.

## 8.3 Results

**8.3.1 Morphological analysis.** Figure 8.1 shows the SEM images of the NWs with different composition of Sb varying from 0 to 4.5 at.% in the GaAsSb insert in GaAs/GaAsSb/GaAs core NW. Assessing the diameter to be between 70 nm to 200 nm, the NWs were measured for their uniformity and shape variation along the length of the NWs. The amount of Sb in the insert is gradually increased with Sb at. % from sample S1 to S4 as 0, 1, 2.6 and 4.5 respectively. As the Sb concentration increases distinct morphological changes have been observed along with faceted growth. Inverted conical shaped NWs were found. Sb act as a

surfactant which can enhance the lateral growth and decrease the axial growth[130]. This results in increase in the lateral growth which is consistent with our experimental results.

**Composition variation of Sb in the GaAsSb insert in GaAs/GaAsSb/GaAs core NWs.**

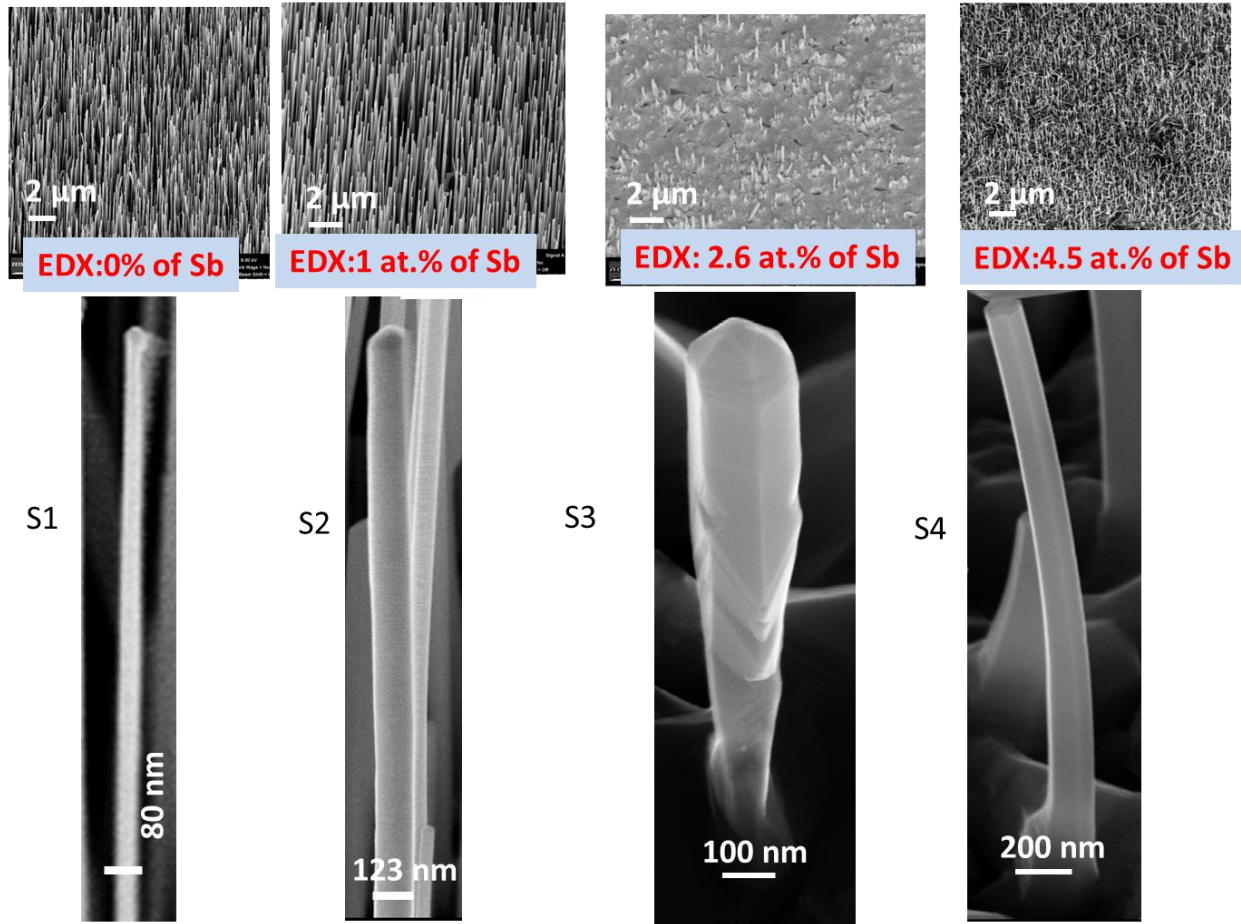


*Figure 8.1.* SEM images of the NWs with different composition of Sb varying from 0 to 4.5 at. % in the GaAsSb insert in GaAs/GaAsSb/GaAs core NW.

There is an increase of the diameter of the NWs from 80 nm (S1); 123 nm (S2); 126 nm (S3) to 230 nm (S4). Due to the difference in the growth time there was change in the height of the NWs from 0.84  $\mu\text{m}$  to 7.15  $\mu\text{m}$ . The density of the wires was  $\sim 3 \times 10^8 \text{ cm}^{-2}$ . Sample S1, S2 and S3 had  $> 95\%$  vertical wires while S4 had curve at an angle of  $83.8^\circ$  from the base. S1 and S2 were very cylindrically uniform. Hexagonal facets can be clearly seen for S4, whereas the shapes of the S3 NWs were conically inverted in shape. The shape changes would be due to the

difference in the Sb incorporation [10, 131]. In sample S3, the lower section of the NW is thinner which gradually enlarges radially with the growth of the NWs. The thinner section refers to the pure GaAs stem. The overgrowth is due to certain facets that evolve along the sidewalls. This indicates the Sb induced lateral growth enhancement. This constriction at the interface between the top GaAsSb segment and bottom GaAs segment is in good agreement with the TEM observation, discussed later.

**8.3.2 Sb composition by EDX.** In order to study the Sb composition, EDX scans were performed on the NWs. Figure 8.2 below shows the EDX spectra for NW (S2) showing the Ga, As and Sb. It was found to have 1at. % of Sb in the NWs.

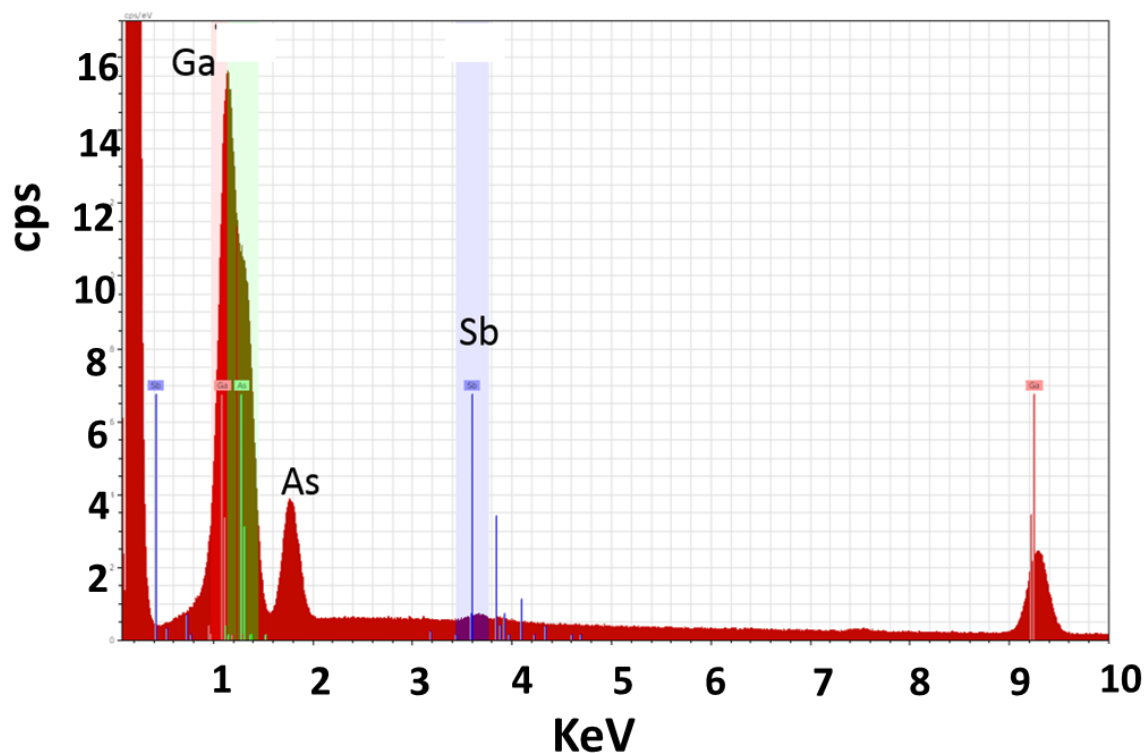


*Figure 8.2.*Shows the EDX spectrum of a GaAs/GaAsSb NW with 1 at. % Sb.

Table 8.1

*The dimensions of the NWs and Sb at. % along the length of S2*

NW segment	Diameter(nm)	Length ( $\mu\text{m}$ )	Sb at. %
GaAs	~125	1.16	~0
GaAsSb	~125	2.41	~1
GaAs	~125	1.10	~0

Similar analysis was done on NWs with higher concentration of Sb. Figure 8.3 below shows EDX spectra for 4.5 at.% Sb and the Table 8.1 depicting the segment size along with the Sb content along the NW.

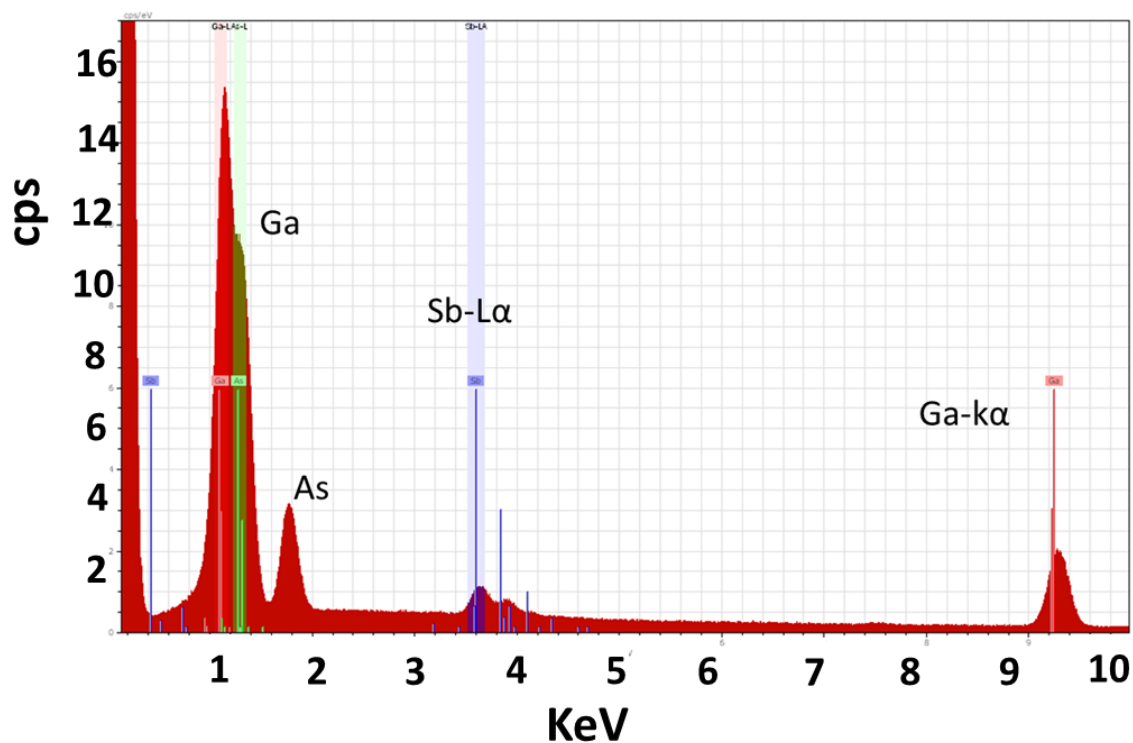


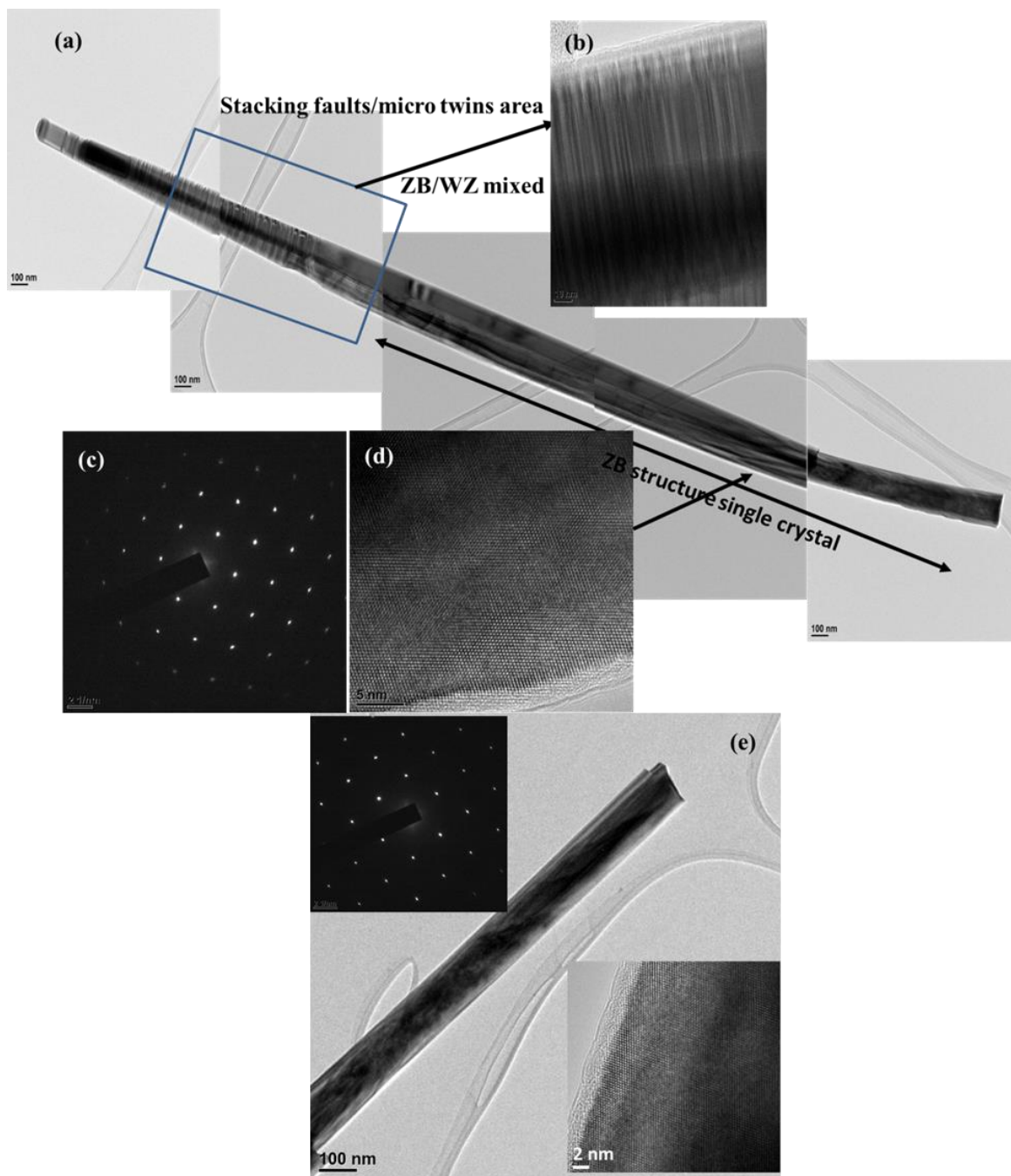
Figure 8.3. Shows the EDX spectrum of a GaAs/GaAsSb NW with 4.5 at. % Sb.

Table 8.2

*The dimensions of the NW and Sb at. % along the length of S4*

NW segment	Diameter (nm)	Length ( $\mu\text{m}$ )	Sb at. %
GaAs	$\sim 280$	$\sim 0.3$	$\sim 0$
GaAsSb	126	$\sim 1.5$	$\sim 4.5$
GaAs	126	$\sim 0.6$	$\sim 0$

**8.3.3 STEM Study.** Figure 8.4 (a) shows the dark field STEM image of a core GaAs/GaAs<sub>0.955</sub>Sb<sub>0.045</sub>/GaAs NW. NW exhibited a ZB structure single crystal (as shown in Figure 8.4 (d)) throughout the entire wire except towards the top where patches of stacking faults and twin defects were observed (Figure 8.4 (b)). These defects can be controlled by altering the growth parameters during the termination process. Another NW which probably was broken off at the tip showed no defects in the body as shown in Fig.8.4 (e).



*Figure 8.4.* (a) TEM image of the core NW (b) HR-TEM image displaying the stacking faults and twinning defects. (c) SAED pattern showing the ZB crystal structure. (d) ZB structure and (e) TEM image of NW2 with the ZB structure (inset) and the SAED pattern (inset).

**8.3.4 X- Ray Diffraction.** Figure 8.5 displays the  $2\theta$  scan of X-ray diffraction spectra for the core samples S1, S2 and S4. The prominent peaks were  $56.28^\circ$  for core GaAs (111) NWs,  $55.88^\circ$  for GaAsSb,  $90.16^\circ$  for GaAs (333) and  $94.93^\circ$  for Si (333) which were identified from the JCPDS standard database. Based on the obtained peaks, different orders of reflection of (111) planes was confirmed. The FWHM was calculated for all of the peaks and were analyzed. There is a shift in the  $2\theta$  from sample S1 to S4. Occurrence of only GaAs (nnn) and GaAsSb (nnn) XRD peaks confirm the vertical orientation of these NWs. Here 'n' represents the miller indices (hkl).

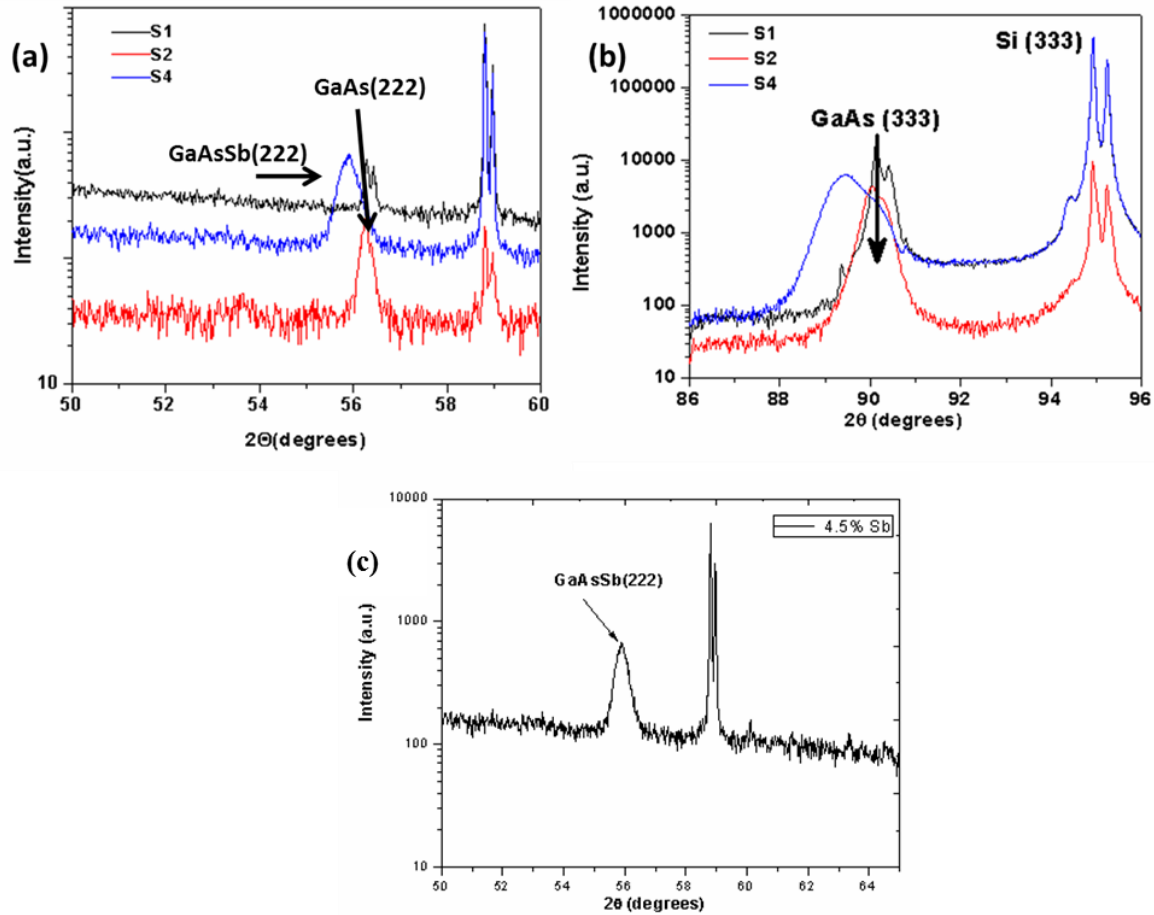


Figure 8.5. The XRD spectra of GaAs/GaAsSb/GaAs for different concentrations of Sb

depicting the occurrence of different planes of GaAs, GaSb and Si. (a) Shows the  $2\theta^\circ$  region from  $50^\circ$  to  $60^\circ$ , (b) from  $86^\circ$  to  $96^\circ$  and (c) the GaAsSb (222) peak for S4 sample.

**8.3.5 Photoluminescence.** Figure 8.6 shows the 4K photoluminescence spectra of the samples with Sb at. % varying from 0 to 4.5.

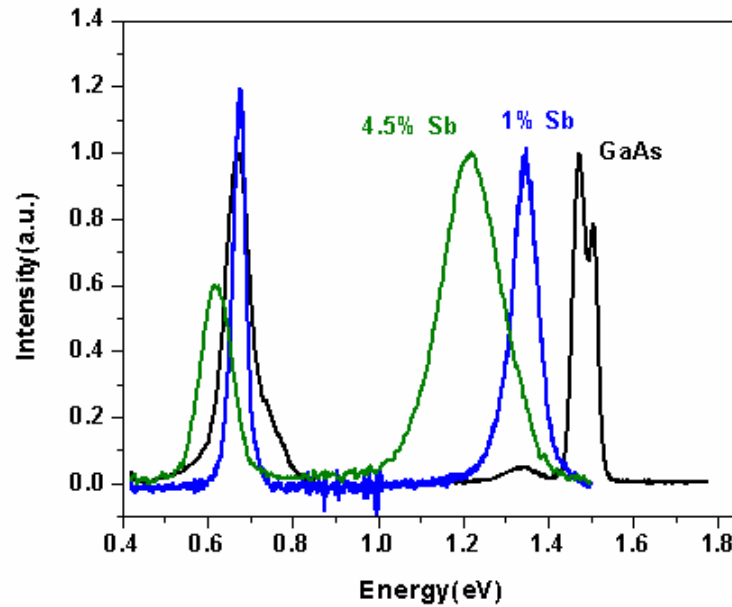


Figure 8.6. 4K PL spectra with Sb at. % varying from 0 to 4.5.

Figure 8.7 shows the temperature dependence of axial GaAs/GaAsSb NWs (S2 and S4). As expected, the intensity of the peak decreases with increasing temperature which is due to the thermal escape of electrons from GaAs well to GaAsSb barrier for the PL quenching [113]. This is well known temperature dependence of energy band gap and is related to increase of interatomic spacing with increasing temperature. It was observed that GaAs NWs also exhibited peaks at 1.47 eV and 1.33 eV which corresponded to the ZB band to band transition and As defect ( $V_{As}$ ) level [132]. The PL transitions observed in the samples are due to two energy levels. The first one is located 0.14 eV below the conduction band which is known as As vacancy level ( $V_{As}$ ) and the second one is attributed to a level L. This possible energy level L could be due to

an EL2 midgap donor level [133-135] or a surface defect level. The surface Fermi level, which is expected to be pinned at the surface defect level below the conduction band, is reported to vary when Sb composition changes,  $E_F=0.70-0.192x$ , where  $x$  is Sb composition. Although the identity is not clear of this energy level, it is placed in the middle of the type II transition.

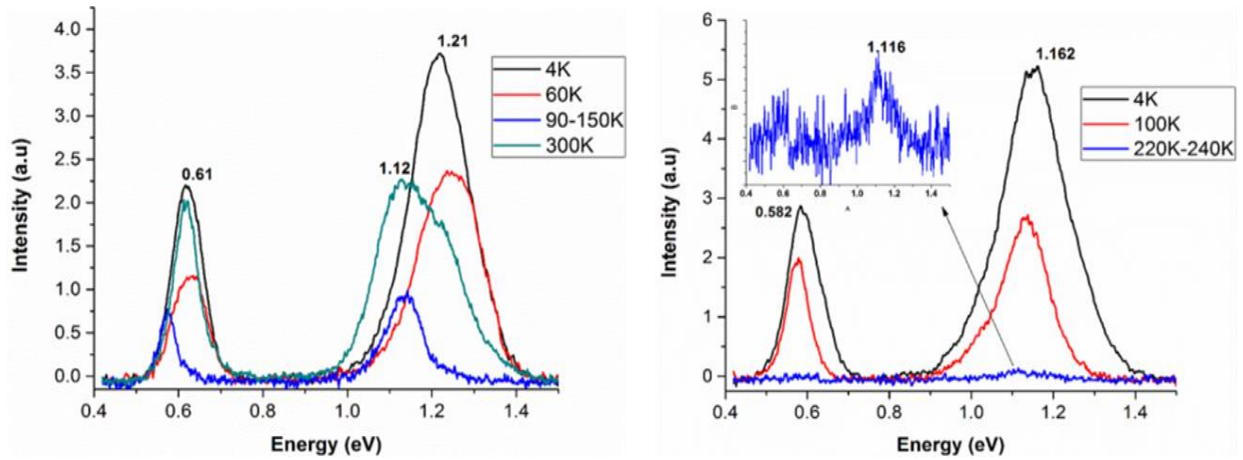


Figure 8.7. Temperature dependent PL spectra for both (a) S2 and (b) S4.

Figure 8.8 depicts the intensity dependent PL analysis of single segmented GaAsSb NWs with Sb at. % of 1(S2) and 4.5 (S4). The prominent PL peak observed were 0.67 eV and 1.35 eV for S2 where as it was 0.61 eV and 1.21 eV for S4. For S4, the Gaussian fit of the PL spectra resulted a peak at 1.21 eV from CB GaAs to the VB GaAsSb (Figure 8.8(b)) exhibiting a blue shift of  $\sim 50$  meV when the incident PL power was increased by 60 times. This type of large blue shift is signature of type II structures which is caused by confinement of carriers in a narrow bandwidth due to electric field induced band bending [113, 136, 137]. The electric field is created by the spatial separation of electron and hole pairs in these structures. Thus this transition is assigned to ZB GaAs conduction band (CB) to ZB GaAsSb (VB) as shown in Figure 8.8. Further convoluting the peak at 16P, two peaks were found namely 1.07 eV and 1.22 eV. These transition could be explained by considering the  $V_{As}$  defect level just below the conduction band of ZB GaAs[132]. The 1.07 eV peak could be a transition from the  $V_{As}$  defect level to VB of

GaAsSb and 1.22 eV peak is attributed to CB of GaAs to VB of GaAsSb. The lower energy peak would be from energy level L to GaAsSb VB.

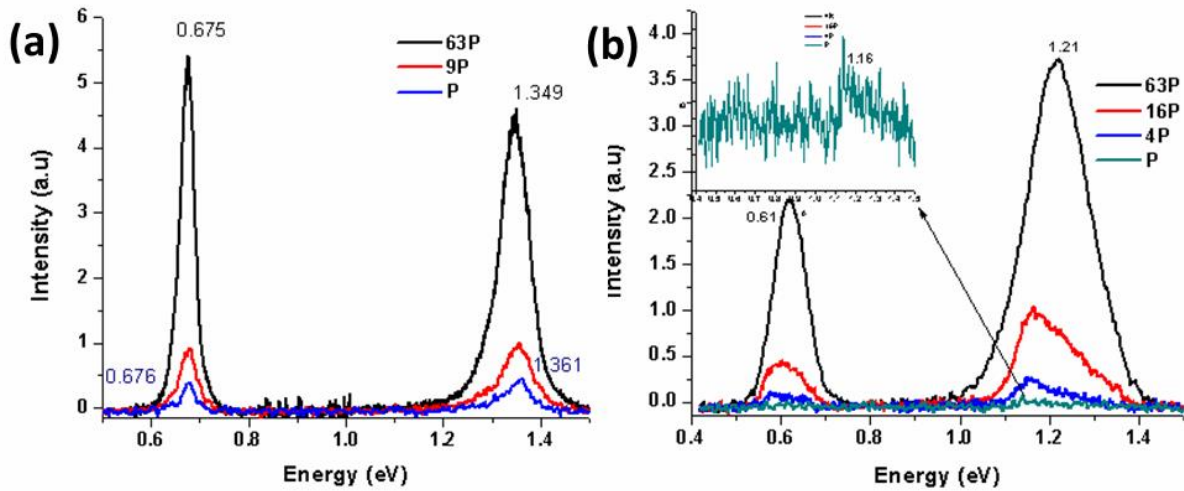
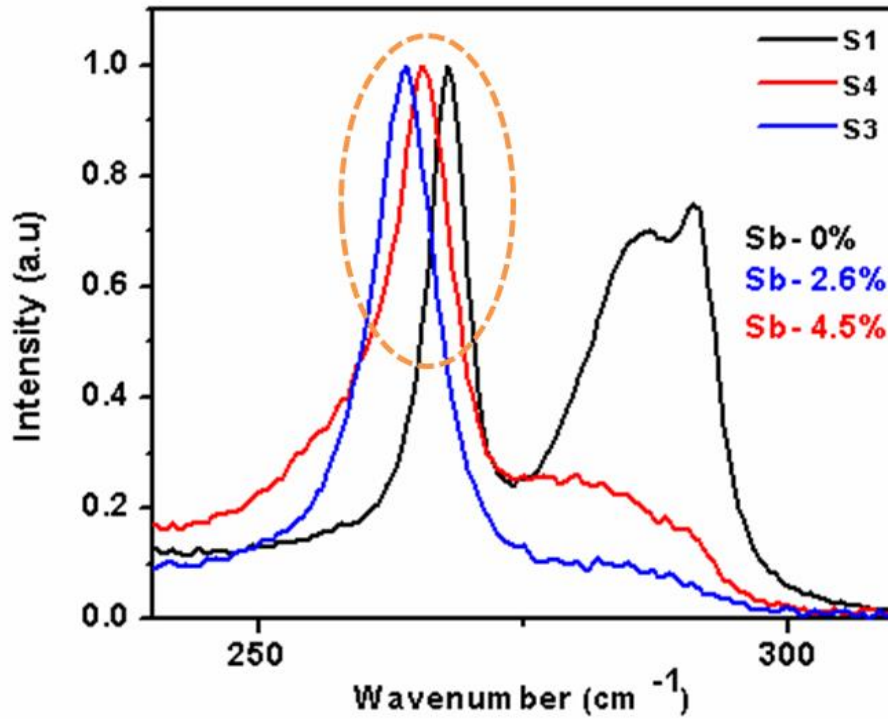


Figure 8.8. Intensity dependent photoluminescence spectra for core sample containing (a) S2 (b) S4.

As shown in Figure 8.9(a), the two transition occurring are assigned as from  $V_{As}$  defect level to the GaAsSb VB and from the surface defect level to the GaAsSb VB. For S2 i.e. GaAs/GaAs<sub>0.99</sub>Sb<sub>0.01</sub> we have an abnormal redshift of 11 meV with increasing intensity from 0.5 mW to 35 mW. This can be explained by the concept of radiation heating[113]. At low concentrations of Sb, a very small blue shift is overcome by a red shift caused by radiation heating leading to overall redshift of 11 meV as shown in Figure 8.9 (a). With increasing incident intensity, the band bending is more pronounced at the interface which leads to large blue shift. It was also observed that, the blue shift was increased with increasing Sb content, which might be due to the strong type II transition with increasing Sb content.



NWs grown so far show great promise for applications in the 1.3  $\mu\text{m}$  region and longer wavelength for optical communications.



*Figure 8.10* Raman spectra depicting the shift in the peak (encircled) with the variation in the at. % of Sb in the samples from S1 to S4.

#### 8.4 Conclusion

In conclusion, Sb was incorporated in GaAsSb insert in axially grown GaAs/GaAsSb NW with Sb at. % varying from 1 to 4.5. These NWs exhibited single crystal ZB structure defect free structure in the body of the GaAsSb insert and exhibits combination of planar defects like twins and stacking fault only near the tip. SEM results showed that as the Sb concentration increases, distinct morphological changes like inverted conical shaped NWs have been observed along with faceted growth. XRD exhibited only (nnn) peaks which confirm the vertical

orientation of these NWs. Prominent PL peaks at 1.21 eV in 4.5 at. % Sb showed a blue shift with the intensity variation confirming a type II transition.

## CHAPTER 9

### Summary and Scope of Future Work

#### 9.1 Summary

**9.1.1 GaAs/GaAsSb Segmented NWs.** A systematic study on the growth and characterization was carried out with two sets of axial NW structures: (a) single segment GaAsSb (N1) and (b) double segment GaAsSb (N2). High quality self-catalyzed GaAs/GaAsSb/GaAs nanowires were grown on Si (111) substrates. Extensive growth study was performed by varying different parameters namely, growth temperature and V/III ratio. These growths were calibrated by using Ga as a catalyst and varying the growth temperature in the window of 580°C-620°C with a constant V/III BEP ratio for Ga and As. GaAsSb segments of length varying from 1  $\mu\text{m}$  to 3.48  $\mu\text{m}$  were inserted in the GaAs NWs. High quality NWs were obtained at the growth temperature of 620°C. The core diameter of the NWs varied from 150-180 nm with height up to 7.15  $\mu\text{m}$ . These NWs exhibited pure ZB phases with randomly spaced stacking faults and multiple twins. The NW density was in the range of  $4 \times 10^6 \text{ cm}^{-2}$  to  $3 \times 10^7 \text{ cm}^{-2}$ . More than 80% of the NWs were vertically aligned in (111) direction normal to the orientation of the substrate.

Low temperature PL study provided a good understanding of the nature of the defects. Double segmented GaAsSb NWs provided higher PL intensity in comparison to single segmented NWs, with a relatively asymmetric line shape and high energy cut off. There was little variation in the FWHM with the PL temperature and  $T_{\text{deloc}}$  was also found to be less due to small range of localization energies. However, single segmented GaAsSb NWs FWHM spectra exhibited an inverted S-curve indicative of strong exciton localization. A relatively lower TO/LO

GaAs phonon Raman peak ratio as well as a lower FWHM of these two modes in double segmented GaAsSb NWs attest to the better quality of these NWs.

**9.1.2 High density and vertical NWs.** Optimization on the growth condition was carried out on GaAs NWs to achieve high density and vertical NWs. Influence of three main growth parameters investigated were: (a) V/III ratio, (b) As species and (c) duration of Ga shutter opening. With a growth temperature of 620°C and a constant duration of Ga shutter opening, when the V/III ratio was increased from 6 to 20, there was a steady increase in the density of the NWs with a maximum of  $3 \times 10^8 \text{ cm}^{-2}$ . The role of As<sub>4</sub> over As<sub>2</sub> was found to affect the growth rate of the NWs. As<sub>4</sub> lead to twice the growth rate indicating the diffusion length of Ga to be larger in comparison to As<sub>2</sub> flux. V/III ratio increases with corresponding increase in the duration of Ga opening. The extrapolated plots of V/III ratio vs duration of Ga opening led to the optimum growth temperature of 620°C with a V/III ratio of 20 resulting in NWs of density of  $5.9 \times 10^8 \text{ cm}^{-2}$  and with high verticality. As the V/III ratio increases, there should be a corresponding increase in the duration of Ga opening too. This combination would result in having a higher vertical and denser yield of NWs.

To increase the NW density further chemical etching and subsequent oxidization in air of the substrate prior to the growth was investigated. Si (111) substrates were chemically treated with piranha solution and later oxidized in an ambient atmosphere. This resulted in forming a favorable SiO<sub>2</sub> layer on the substrate with an rms roughness value of 2.57 nm confirmed by the AFM measurements. The thickness of the layer was SiO<sub>2</sub> approximately  $9.1 \pm 2 \text{ \AA}$ . Using this approach significant increase in NW density reaching up to  $8 \times 10^8 \text{ cm}^{-2}$  was obtained. However, a comparison of the non-etched and etched samples indicated the etched samples to be somewhat of superior quality in terms of strain and defects based on the Raman and TEM data.

Using these optimized growth conditions effect of the Sb variation was examined where Sb at. % varied from 0 to 4.5 in the inserts of the axially grown NWs. Presence of prominent XRD peaks of GaAs (111), GaAsSb(111) and Si(333) is clear evidence of vertical orientation of the NWs. The peak shifts towards lower Bragg angle with corresponding increase in the FWHM are consistent with the increased Sb incorporation in the NW. Strain accumulation in the NW caused curving of the NWs at higher Sb concentration of 4.5 at. %. These NWs exhibited single crystal ZB structure with some combination of planar defects. PL emission of 1.21 eV and 1.16 eV were obtained for GaAs/GaAs<sub>0.99</sub>Sb<sub>0.01</sub>/GaAs NWs and GaAs/GaAs<sub>0.955</sub>Sb<sub>0.045</sub>/GaAs NWs, respectively. A blue shift of ~50 meV of the 1.21 eV peak under intensity variation indicated a type II type of transition for Sb concentration of 4at. %.

**9.1.3 Doping.** For a good device, the p-type doping incorporation was studied in details on a core-shell GaAs NW configuration and elemental Be was examined for p-type dopant. A detailed investigation on the V/III ratio of the core, shell and Be cell temperature on the Be incorporation was performed. Beside core, the shell configuration played an important role in the Be incorporation in the NWs. The V/III ratio of 35 for the shell configuration with a Be cell temperature of 990°C was found to be optimum for higher Be incorporation. The prominent photoluminescence peak in the range of 1.48-1.51 eV confirmed the Be incorporation in the NWs. Room temperature Raman analysis and the I-V measurements of the NWs were also consistent with enhanced Be incorporation at the above stated shell growth condition.

## 9.2 Future Work

These are preliminary data and a fairly good optical and structural quality of the GaAsSb NWs grown so far show great promise for applications in the 1.3  $\mu\text{m}$  region and longer wavelength in fiber optics for quantum networking. To reach the 1.55  $\mu\text{m}$  optical window

requires significant increase in Sb and that may be challenging. More work needs to be done in this direction by increasing the number of GaAsSb inserts and further study on the effect of Sb concentration on material deterioration needs to be addressed.

As already growth parameters are optimized for GaAs/GaAsSb axial NWs for 4.5 at.% Sb concentration and a study of p-type doping study, a natural sequence is the device fabrication. Hence a parallel path is recommended for the demonstration of photodetector of high sensitivity.

## References

1. Tomioka, K., M. Yoshimura, and T. Fukui, *A III-V nanowire channel on silicon for high-performance vertical transistors*. Nature, 2012. **488**(7410): p. 189-192.
2. Dresselhaus, M., et al., *Nanowires*, in *Springer Handbook of Nanotechnology*, B. Bhushan, Editor. 2010, Springer Berlin Heidelberg. p. 119-167.
3. Zhang, A., et al., *Silicon nanowire detectors showing phototransistive gain*. Applied Physics Letters, 2008. **93**(12): p. 121110.
4. Shapiro, J.N., et al., *InGaAs heterostructure formation in catalyst-free GaAs nanopillars by selective-area metal-organic vapor phase epitaxy*. Applied Physics Letters, 2010. **97**(24): p. 243102.
5. Scofield, A.C., et al., *Bottom-up Photonic Crystal Lasers*. Nano Letters, 2011. **11**(12): p. 5387-5390.
6. Khudiyev, T., E. Huseyinoglu, and M. Bayindir, *Non-resonant Mie scattering: Emergent optical properties of core-shell polymer nanowires*. Sci. Rep., 2014. **4**.
7. Van Kouwen, M., et al., *Single quantum dot nanowire photodetectors*. Applied Physics Letters, 2010. **97**(11): p. 113108.
8. Claudon, J., et al., *A highly efficient single-photon source based on a quantum dot in a photonic nanowire*. Nature Photonics, 2010. **4**(3): p. 174-177.
9. Todorovic, J., et al., *The effects of Sb concentration variation on the optical properties of GaAsSb/GaAs heterostructured nanowires*. Semiconductor Science and Technology, 2013. **28**(11): p. 115004.

10. Borg, B.M. and L.-E. Wernersson, *Synthesis and properties of antimonide nanowires*. Nanotechnology, 2013. **24**(20): p. 202001.
11. Hadfield, R.H., et al., *Quantum key distribution at 1550nm with twin superconducting single-photon detectors*. Applied physics letters, 2006. **89**(24): p. 241129.
12. Hadfield, R.H., *Single-photon detectors for optical quantum information applications*. Nature photonics, 2009. **3**(12): p. 696-705.
13. Rosfjord, K.M., et al., *Nanowire single-photon detector with an integrated optical cavity and anti-reflection coating*. Optics Express, 2006. **14**(2): p. 527-534.
14. Chuang, L.C., et al., *Critical diameter for III-V nanowires grown on lattice-mismatched substrates*. Applied Physics Letters, 2007. **90**(4): p. 043115.
15. Dheeraj, D., et al., *Zinc blende GaAsSb nanowires grown by molecular beam epitaxy*. Nanotechnology, 2008. **19**(27): p. 275605.
16. Dubrovskii, V.G., et al., *Diffusion-induced growth of GaAs nanowhiskers during molecular beam epitaxy: Theory and experiment*. Physical Review B, 2005. **71**(20): p. 205325.
17. Fontcuberta i Morral, A., et al., *Nucleation mechanism of gallium-assisted molecular beam epitaxy growth of gallium arsenide nanowires*. Applied Physics Letters, 2008. **92**(6): p.- 063112.
18. Colombo, C., et al., *Ga-assisted catalyst-free growth mechanism of GaAs nanowires by molecular beam epitaxy*. Physical Review B, 2008. **77**(15): p. 155326.
19. Paek, J., et al., *Catalyst free MBE-VLS growth of GaAs nanowires on (111) Si substrate*. physica status solidi (c), 2009. **6**(6): p. 1436-1440.

20. Jabeen, F., et al., *Self-catalyzed growth of GaAs nanowires on cleaved Si by molecular beam epitaxy*. Nanotechnology, 2008. **19**(27): p. 275711.
21. Mattila, M., et al., *Catalyst-free growth of In (As) P nanowires on silicon*. Applied physics letters, 2006. **89**(6): p. 063119.
22. Mandl, B., et al., *Au-free epitaxial growth of InAs nanowires*. Nano letters, 2006. **6**(8): p. 1817-1821.
23. Corkish, R., et al., *Applied Photovoltaics*. 2013: Taylor & Francis.
24. Jabeen, F., *III-V semiconducting nanowires by molecular beam epitaxy*. 2009.
25. Sang-Woo, S., et al., *High-speed large-area inverted InGaAs thin-film metal-semiconductor-metal photodetectors*. Selected Topics in Quantum Electronics, IEEE Journal of, 2004. **10**(4): p. 686-693.
26. Teissier, R., et al., *Temperature-dependent valence band offset and band-gap energies of pseudomorphic GaAsSb on GaAs*. Journal of Applied Physics, 2001. **89**(10): p. 5473-5477.
27. Nunna, K.C., *A Study of GaAsSb/GaAs Quantum Well Structures Grown by Molecular Beam Epitaxy*, 2003, North Carolina Agricultural and Technical State University.
28. Y R Chen, L.C.C., Y J Yang and H H Lin, *Twinning in GaAsSb grown on (1 1 1)B GaAs by molecular beam epitaxy*. J. Phys. D: Appl. Phys, 2013. **46**: p. 035306.
29. Dheeraj, D.L., et al., *Growth and Characterization of Wurtzite GaAs Nanowires with Defect-Free Zinc Blende GaAsSb Inserts*. Nano Letters, 2008. **8**(12): p. 4459-4463.
30. Plissard, S., et al., *Gold-free GaAs/GaAsSb heterostructure nanowires grown on silicon*. Applied Physics Letters, 2010. **96**(12): p. 121901-3.

31. Alarcón-Lladó, E., et al., *Raman spectroscopy of self-catalyzed GaAs<sub>1-x</sub>Sb<sub>x</sub> nanowires grown on silicon*. Nanotechnology, 2013. **24**(40): p. 405707.
32. Ghalamestani, S.G., et al., *Self-catalyzed MBE grown GaAs/GaAs<sub>x</sub>Sb<sub>1-x</sub> core-shell nanowires in ZB and WZ crystal structures*. Nanotechnology, 2013. **24**(40): p. 405601.
33. Huffaker, D., et al., *1.3 μm room-temperature GaAs-based quantum-dot laser*. Applied Physics Letters, 1998. **73**(18): p. 2564-2566.
34. Wei, S.-H., J. Li, and Y. Yan. *Design of shallow p-type dopants in ZnO*. in *Photovoltaic Specialists Conference, 2008. PVSC'08. 33rd IEEE*. 2008. IEEE.
35. Zhang, S.B., S.H. Wei, and A. Zunger, *Overcoming doping bottlenecks in semiconductors and wide-gap materials*. Physica B: Condensed Matter, 1999. **273–274**(0): p. 976-980.
36. Casadei, A., et al., *Doping incorporation paths in catalyst-free Be-doped GaAs nanowires*. Applied Physics Letters, 2013. **102**(1): p. 013117-013117-4.
37. Dheeraj, D.L., et al., *Comparison of Be-doped GaAs nanowires grown by Au- and Ga-assisted molecular beam epitaxy*. Journal of Crystal Growth, 2013: p. 532-536.
38. Hilse, M., et al., *Incorporation of the dopants Si and Be into GaAs nanowires*. Applied Physics Letters, 2010. **96**(19): p. 193104.
39. Dheeraj, D.L, et al., *Growth and structural characterization of GaAs/GaAsSb axial heterostructured nanowires*. Journal of Crystal Growth, 2009. **311**(7): p. 1847-1850.
40. Dick, K.A., et al., *Failure of the vapor-liquid-solid mechanism in Au-assisted MOVPE growth of InAs nanowires*. Nano Letters, 2005. **5**(4): p. 761-764.

41. Sun, X., et al., *GaAsSb: A novel material for near infrared photodetectors on GaAs substrates*. Selected Topics in Quantum Electronics, IEEE Journal of, 2002. **8**(4): p. 817-822.
42. S Plissard, G Larrieu, X Wallart and P Caroff, *High yield of self-catalyzed GaAs nanowire arrays grown on silicon via gallium droplet positioning*. Nanotechnology, 2011. **22**: p. 275602.
43. Harmand, J., et al., *Analysis of vapor-liquid-solid mechanism in Au-assisted GaAs nanowire growth*. Applied Physics Letters, 2005. **87**(20): p. 203101-203101-3.
44. Koguchi, M., et al., *Crystal structure change of GaAs and InAs whiskers from zinc-blende to wurtzite type*. Japanese journal of applied physics, 1992. **31**(7R): p. 2061.
45. Persson, A.I., et al., *Solid-phase diffusion mechanism for GaAs nanowire growth*. Nat Mater, 2004. **3**(10): p. 677-681.
46. Glas, F., *Critical dimensions for the plastic relaxation of strained axial heterostructures in free-standing nanowires*. Physical Review B, 2006. **74**(12): p. 121302.
47. Wagner, R.S. and W.C. Ellis, *Vapor-Liquid-Solid Mechanism Of Single Crystal Growth*. Applied Physics Letters, 1964. **4**(5): p. 89-90.
48. Lauhon, L., M.S. Gudiksen, and C.M. Lieber, *Semiconductor nanowire heterostructures*. Philosophical Transactions of the Royal Society of London. Series A: Mathematical, Physical and Engineering Sciences, 2004. **362**(1819): p. 1247-1260.
49. Wu, Z.H., et al., *Growth of Au-catalyzed ordered GaAs nanowire arrays by molecular-beam epitaxy*. Applied Physics Letters, 2002. **81**(27): p. 5177-5179.
50. Plante, M. and R. LaPierre, *Growth mechanisms of GaAs nanowires by gas source molecular beam epitaxy*. Journal of crystal growth, 2006. **286**(2): p. 394-399.

51. Ihn, S.-G., et al., *Growth of GaAs nanowires on Si substrates using a molecular beam epitaxy*. Nanotechnology, IEEE Transactions on, 2007. **6**(3): p. 384-389.
52. Samsonenko, Y.B., et al., *Specific features of formation of GaAs nanowire crystals during molecular beam epitaxy on different silicon surfaces*. Semiconductors, 2008. **42**(12).
53. Hoang, T.B., et al., *Observation of free exciton photoluminescence emission from single wurtzite GaAs nanowires*. Applied Physics Letters, 2009. **94**(13): p. 133105.
54. Pantelides, S.T., *Deep Centers in Semiconductors*. 1992: Taylor & Francis.
55. Breuer, S., et al., *Suitability of Au- and Self-Assisted GaAs Nanowires for Optoelectronic Applications*. Nano Letters, 2011. **11**(3): p. 1276-1279.
56. Krogstrup, P., et al., *Structural Phase Control in Self-Catalyzed Growth of GaAs Nanowires on Silicon (111)*. Nano Letters, 2010. **10**(11): p. 4475-4482.
57. Glas, F., J.-C. Harmand, and G. Patriarche, *Why Does Wurtzite Form in Nanowires of III-V Zinc Blende Semiconductors*. Physical Review Letters, 2007. **99**(14): p. 146101.
58. Joyce, H.J., et al., *Twin-free uniform epitaxial GaAs nanowires grown by a two-temperature process*. Nano letters, 2007. **7**(4): p. 921-926.
59. Joyce, H.J., et al., *Phase Perfection in Zinc Blende and Wurtzite III–V Nanowires Using Basic Growth Parameters*. Nano Letters, 2010. **10**(3): p. 908-915.
60. Howard, A.D., D.C. Chapman, and G.B. Stringfellow, *Effects of surfactants Sb and Bi on the incorporation of zinc and carbon in III/V materials grown by organometallic vapor-phase epitaxy*. Journal of Applied Physics, 2006. **100**(4): p. 044904.
61. <http://lab.frumania.com>.

62. Tomioka, K., et al., *GaAs/AlGaAs core multishell nanowire-based light-emitting diodes on Si*. Nano letters, 2010. **10**(5): p. 1639-1644.
63. Tambe, M.J., et al., *Realization of defect-free epitaxial core-shell GaAs/AlGaAs nanowire heterostructures*. Applied Physics Letters, 2008. **93**(15): p. 151917.
64. Mayer, B., et al., *Lasing from individual GaAs-AlGaAs core-shell nanowires up to room temperature*. Nature communications, 2013. **4**.
65. Ercolani, D., et al., *Growth of InAs/InAsSb heterostructured nanowires*. Nanotechnology, 2012. **23**(11): p. 115606.
66. Borg, B.M., et al., *Enhanced Sb incorporation in InAsSb nanowires grown by metalorganic vapor phase epitaxy*. Applied Physics Letters, 2011. **98**(11): p. 113104.
67. Du, W.-N., et al., *The self-seeded growth of InAsSb nanowires on silicon by metal-organic vapor phase epitaxy*. Journal of Crystal Growth, 2014. **396**: p. 33-37.
68. Jeppsson, M., et al., *GaAs/GaSb nanowire heterostructures grown by MOVPE*. Journal of Crystal Growth, 2008. **310**(18): p. 4115-4121.
69. Svensson, J., et al., *Diameter-dependent photocurrent in InAsSb nanowire infrared photodetectors*. Nano letters, 2013. **13**(4): p. 1380-1385.
70. Kim, D.J., *Novel Growth of InGaAs/GaAs Nanostructures by Molecular Beam Epitaxy*. Graduate Theses and Dissertations, 2009: p. 258.
71. Kim, S., et al., *Electron mobility enhancement of extremely thin body  $In_{0.7}Ga_{0.3}As$ -on-insulator metal-oxide-semiconductor field-effect transistors on Si substrates by metal-oxide-semiconductor interface buffer layers*. Applied Physics Express, 2012. **5**(1): p. 014201.

72. Heiss, M., et al., *Direct correlation of crystal structure and optical properties in wurtzite/zinc-blende GaAs nanowire heterostructures*. Physical Review B, 2011. **83**(4): p. 045303.
73. Teissier, R., et al., *Temperature-dependent valence band offset and band-gap energies of pseudomorphic GaAsSb on GaAs*. Journal of Applied Physics, 2001. **89**(10): p. 5473-5477.
74. Yano, M., et al., *Molecular-beam epitaxial growth and interface characteristics of GaAsSb on GaAs substrates*. Journal of Vacuum Science & Technology B, 1989. **7**(2): p. 199-203.
75. Kauko, H., et al., *Near-surface depletion of antimony during the growth of GaAsSb and GaAs/GaAsSb nanowires*. Journal of Applied Physics, 2014. **116**(14): p. 144303.
76. Todorovic, J., et al., *Correlated micro-photoluminescence and electron microscopy studies of the same individual heterostructured semiconductor nanowires*. Nanotechnology, 2011. **22**(32): p. 325707.
77. Salehzadeh, O., et al., *Rectifying characteristics of Te-doped GaAs nanowires*. Applied Physics Letters, 2011. **99**(18): p. 182102.
78. Czaban, J.A., D.A. Thompson, and R.R. LaPierre, *GaAs Core–Shell Nanowires for Photovoltaic Applications*. Nano Letters, 2009. **9**(1): p. 148-154.
79. Ilegems, M., *Beryllium doping and diffusion in molecular-beam epitaxy of GaAs and  $Al_xGa_{1-x}As$* . Journal of Applied Physics, 1977. **48**(3): p. 1278-1287.
80. Yu, S., T. Tan, and U. Gosele, *Diffusion mechanism of zinc and beryllium in gallium arsenide*. Journal of applied physics, 1991. **69**(6): p. 3547-3565.

81. Yee, R., et al., *Effects of Be doping on InP nanowire growth mechanisms*. Applied Physics Letters, 2012. **101**(26): p. 263106-263106-5.
82. Dubrovskii, V. and N. Sibirev, *General form of the dependences of nanowire growth rate on the nanowire radius*. Journal of crystal growth, 2007. **304**(2): p. 504-513.
83. Arthur, J.R., *Molecular beam epitaxy*. Surface science, 2002. **500**(1): p. 189-217.
84. Maksym, P. and J.L. Beeby, *A theory of RHEED*. Surface Science, 1981. **110**(2): p. 423-438.
85. Braun, W., *Applied RHEED: reflection high-energy electron diffraction during crystal growth*. 1999: Springer Science & Business Media.
86. Neave, J., B. Joyce, and P. Dobson, *Dynamic RHEED observations of the MBE growth of GaAs*. Applied Physics A, 1984. **34**(3): p. 179-184.
87. Cheze, C., *Investigation and comparison of GaN nanowire nucleation and growth by the catalyst-assisted and selfinduced approach*, 2010, Ph. D. Dissertation, Humboldt-Universität zu Berlin, Germany.
88. <http://www.zeiss.com/>.
89. Anastassakis, E., *Selection rules of Raman scattering by optical phonons in strained cubic crystals*. Journal of applied physics, 1997. **82**(4): p. 1582-1591.
90. Zardo, I., et al., *Raman spectroscopy of wurtzite and zinc-blende GaAs nanowires: Polarization dependence, selection rules, and strain effects*. Physical Review B, 2009. **80**(24): p. 245324.
91. Ewen Smith, G.D., *Modern Raman Spectroscopy: A Practical Approach*.
92. <http://www.azom.com/>.

93. D. B. Williams and C. B. Carter, *Transmission Electron Microscopy: A Textbook for Materials Science*. Springer.
94. Tejwani, M., et al., *Growth and diffusion of abrupt beryllium-doped profiles in gallium arsenide by organometallic vapor phase epitaxy*. Applied physics letters, 1988. **53**(24): p. 2411-2413.
95. Iyer, S., et al., *A Study of Ga-Assisted Growth of GaAs/GaAsSb Axial Nanowires by Molecular Beam Epitaxy*. Nanoscience and Nanoengineering: Advances and Applications, 2014: p. 31.
96. S.Bharatan, "*MBE growth of lattice-matched GaAsSbN/GaAs and InGaAsSbN/GaSb quantum wells for optoelectronic devices*" *Electrical and Computer Engineering, North Carolina A&T State University*. 2009.
97. Wang, H., et al., *Atomistics of vapour–liquid–solid nanowire growth*. Nat Commun, 2013. **4**.
98. Massies, J. and N. Grandjean, *Surfactant effect on the surface diffusion length in epitaxial growth*. Physical Review B, 1993. **48**(11): p. 8502.
99. Kandel, D. and E. Kaxiras, *The surfactant effect in semiconductor thin film growth*. arXiv preprint cond-mat/9901177, 1999.
100. Lysov, A., et al., *Optical properties of heavily doped GaAs nanowires and electroluminescent nanowire structures*. Nanotechnology, 2011. **22**(8): p. 085702.
101. N. Begum, A.S.B., M. Piccin, G. Bais, F. Jabeen, S. Rubini, F. Martelli, and A. Franciosi, *Adv. Mater. Res*, 2008. **31**(23).
102. Jeong, T., et al., *Electric-field-induced quenching effect of photoluminescence on p-GaN films*. 2005.

103. Springer, T. and R. Lechner, *Diffusion in Condensed Matter*. Vieweg, Wiesbaden, 1998: p. 59.
104. Komsa, H.-P., et al., *Beryllium doping of GaAs and GaAsN studied from first principles*. Physical Review B, 2009. **79**(11): p. 115208.
105. Mosca, R., et al., *Influence of the As/Ga flux ratio on diffusion of Be in MBE GaAs layers*. Materials Science and Engineering: B, 2001. **80**(1–3): p. 32-35.
106. Patkar, M.P., et al., *Very low resistance nonalloyed ohmic contacts using low-temperature molecular beam epitaxy of GaAs*. Applied Physics Letters, 1995. **66**(11): p. 1412-1414.
107. Howes, M.J. and D.V. Morgan, *Gallium arsenide: materials, devices, and circuits*. Chichester, England and New York, Wiley-Interscience, 1985, 592 p. No individual items are abstracted in this volume., 1985. **1**.
108. Schulte, D.W., *Growth and characterization of III-V compound semiconductor materials for use in novel MODFET structures and related devices*. 1995.
109. Rosenblatt, G.M., P.K. Lee, and M.B. Dowell, *Vaporization of Solids. Mechanism of Retarded Vaporization from a One-Component Single Crystal*. The Journal of Chemical Physics, 1966. **45**(9): p. 3454-3455.
110. Yeh, C.-Y., et al., *Zinc-blende–wurtzite polytypism in semiconductors*. Physical Review B, 1992. **46**(16): p. 10086.
111. Varshni, Y., *Temperature dependence of the energy gap in semiconductors*. Physica, 1967. **34**(1): p. 149-154.

112. Torchynska, T., et al., *Comparative investigation of photoluminescence of silicon wire structures and silicon oxide films*. Journal of Physics and Chemistry of Solids, 2002. **63**(4): p. 561-568.
113. Chiu, Y., et al., *Properties of photoluminescence in type-II GaAsSb/GaAs multiple quantum wells*. Journal of applied physics, 2002. **92**(10): p. 5810-5813.
114. Li, J., et al., *Annealing effects on the temperature dependence of photoluminescence characteristics of GaAsSbN single-quantum wells*. Journal of Applied Physics, 2005. **98**(1): p. 013703.
115. Patra, N.C., et al., *Molecular beam epitaxial growth and characterization of  $\text{InSb}_{1-x}\text{N}_x$  on GaAs for long wavelength infrared applications*. Journal of Applied Physics, 2012. **111**(8): p. 083104.
116. Duan, X., et al., *Single-nanowire electrically driven lasers*. Nature, 2003. **421**(6920): p. 241-245.
117. Begum, N., et al., *Structural characterization of GaAs and InAs nanowires by means of Raman spectroscopy*. Journal of Applied Physics, 2008. **104**(10): p. 104311-6.
118. Pease, R., *Electron beam lithography*. Contemporary Physics, 1981. **22**(3): p. 265-290.
119. Hochbaum, A.I., et al., *Controlled Growth of Si Nanowire Arrays for Device Integration*. Nano Letters, 2005. **5**(3): p. 457-460.
120. Bougerol, C., H. Mariette, and R. Songmuang, *Intrinsic limits governing MBE growth of Ga-assisted GaAs nanowires on Si (111)*. Journal of Crystal Growth, 2013. **364**: p. 118-122.

121. Hayakawa, T., et al., *Comparison of As species ( $As_4$  and  $As_2$ ) in molecular beam epitaxial growth of  $Al_xGa_{1-x}As$  ( $x=0.2-0.7$ ) on (100) GaAs*. Applied physics letters, 1991. **59**(19): p. 2415-2417.
122. Tersoff, J., M. Johnson, and B. Orr, *Adatom densities on GaAs: Evidence for near-equilibrium growth*. Physical review letters, 1997. **78**(2): p. 282.
123. Wolkenberg, A., *A Mechanism for the Effect of Doping on the Silicon Native Oxide Thickness*. physica status solidi (a), 1983. **79**(1): p. 313-322.
124. Angermann, H., et al., *Wet-chemical passivation of Si (111)-and Si (100)-substrates*. Materials Science and Engineering: B, 2000. **73**(1): p. 178-183.
125. Raider, S. and A. Berman, *On the nature of fixed oxide charge*. Journal of The Electrochemical Society, 1978. **125**(4): p. 629-633.
126. Miccoli, I., et al., *Synthesis of vertically-aligned GaAs nanowires on GaAs/(111) Si hetero-substrates by metalorganic vapour phase epitaxy*. Crystal Research and Technology, 2011. **46**(8): p. 795-800.
127. Sartel, C., et al., *Effect of arsenic species on the kinetics of GaAs nanowires growth by molecular beam epitaxy*. Journal of Crystal Growth, 2010. **312**(14): p. 2073-2077.
128. Munshi, A.M., et al., *Crystal phase engineering in self-catalyzed GaAs and GaAs/GaAsSb nanowires grown on Si (111)*. Journal of Crystal Growth, 2013. **372**: p. 163-169.
129. Ba Hoang, T., et al., *Engineering parallel and perpendicular polarized photoluminescence from a single semiconductor nanowire by crystal phase control*. Nano letters, 2010. **10**(8): p. 2927-2933.

130. Anyebe, E.A., et al., *Surfactant effect of antimony addition to the morphology of self-catalyzed  $\text{InAs}_{1-x}\text{Sb}_x$  nanowires*. Nano Research, 2014: p. 1-11.
131. Xu, T., et al., *Faceting, composition and crystal phase evolution in III–V antimonide nanowire heterostructures revealed by combining microscopy techniques*. Nanotechnology, 2012. **23**(9): p. 095702.
132. Prucnal, S., et al., *Temperature stable 1.3  $\mu\text{m}$  emission from GaAs*. Optics express, 2012. **20**(23): p. 26075-26081.
133. Tajima, M., T. Iino, and K. Ishida, *Above Band-Gap Excitation Process of the 0.6 eV Luminescence Band in GaAs*. Japanese journal of applied physics, 1987. **26**(6A): p. L1060.
134. Dabrowski, J. and M. Scheffler, *Isolated arsenic-antisite defect in GaAs and the properties of EL2*. Physical Review B, 1989. **40**(15): p. 10391.
135. Bourgoin, J. and T. Neffati, *The energy level of the EL2 defect in GaAs*. Solid-State Electronics, 1999. **43**(1): p. 153-158.
136. Morozov, S., et al., *Type II–type I conversion of GaAs/GaAsSb heterostructure energy spectrum under optical pumping*. Journal of Applied Physics, 2013. **113**(16): p. 163107.
137. Kasanaboina, P.K., et al. *Tailoring of GaAs/GaAsSb core-shell structured nanowires for IR photodetector applications*. in *SPIE OPTO*. 2015. International Society for Optics and Photonics.

## *Appendix A*

### **Publications and Conference presentations during the research work**

#### **1. List of Publications:**

1. Shanthi Iyer, Lew Reynolds, Thomas Rawdanowicz, Sai Krishna Ojha, Pavan Kumar Kasanaboina, and Adam Bowen, “A Study of Ga-Assisted Growth of GaAs/GaAsSb Axial Nanowires by Molecular Beam Epitaxy”, *Nanoscience and Nanoengineering: Advances and Applications*, CRC Press, 2014: p. 31-50, Print ISBN: 978-1-4822-3119-9, eBook ISBN: 978-1-4822-3120-5, DOI: 10.1201/b16957-5.

#### **2. List of Conferences:**

1. Sai Krishna Ojha, Pavan Kumar Kasanaboina, Lewis Reynolds, Thomas Rawdanowicz and Shanthi Iyer, “Study of Ga Assisted GaAs/GaAsSb Heterostructure Nanowires and Be doping in GaAs NWs for IR photodetector applications”, 30th North America Molecular Beam Epitaxy conference (NAMBE 2013), Oral presentation, Banff, Alberta, Canada, Oct 5-10, 2013.
2. Sai Krishna Ojha, Pavan Kumar Kasanaboina, Lewis Reynolds, Thomas Rawdanowicz and Shanthi Iyer, “Study of Double Segmented GaAsSb Inserts in Ga Assisted GaAs/GaAsSb Nanowires for IR Photodetector Applications”, MRS/ASM/AVS/AReMS Meeting 2013, Raleigh, NC, Oral presentation, Nov 15, 2013.
3. Sai Krishna Ojha, Pavan Kumar Kasanaboina, Lewis Reynolds, Thomas Rawdanowicz and Shanthi Iyer, “Effect of GaAsSb Inserts in Ga Assisted GaAs/GaAsSb Heterostructured Nanowires and Be Doping in GaAs NWs”, MRS Fall Meeting 2013, Boston, MA, Oral presentation, Dec 03, 2013.
4. Sai Krishna Ojha, Pavan Kumar Kasanaboina, Lewis Reynolds, Thomas Rawdanowicz and Shanthi Iyer, “Growth Optimization of GaAsSb Inserts in Ga Assisted GaAs/GaAsSb

Heterostructure Nanowires for IR Photodetector Applications”, 56th Electronic Materials Conference (EMC) and Exhibition, Oral presentation, Santa Barbara, CA, (June 24-27, 2014)

5. Sai Krishna Ojha, Pavan Kumar Kasanaboina, Lewis Reynolds, Tom Rawdanowicz and Shanthi Iyer, “A study of Be doping in Ga assisted GaAs nanowires by molecular beam epitaxy”, NAMBE 2014, poster presentation, Flagstaff, Arizona, Sep 7-12, 2014.

6. Pavan Kumar Kasanaboina , Sai Krishna Ojha , Shifat U. Sami , Lewis Reynolds ,Yang Liu , Shanthi Iyer, “Tailoring of GaAs/GaAsSb core-shell structured nanowires for IR photodetector applications”, Oral presentation, Proc. SPIE 9373, San Fransisco, CA, February 27, 2015.

**Manuscript in preparation:**

1. Sai Krishna Ojha, Pavan Kumar Kasanaboina, Lewis Reynolds, Tom Rawdanowicz, Ryan White and Shanthi Iyer, ”A Study of Be doped GaAs Nanowires grown by Ga Assisted Molecular Beam Epitaxy” .

2. “Band tuning of GaAs/GaAsSb axial nanowires for IR photovoltaic applications”  
(Manuscript, in preparation).